

Search for charginos and neutralinos decaying via a W and a Higgs boson into final states with two same-sign leptons with the ATLAS detector

(Suche nach Charginos und Neutralinos im Zerfall über ein W
und ein Higgs Boson in Endzustände mit zwei gleich-geladenen
Leptonen mit dem ATLAS Detektor)



LUDWIG-MAXIMILIANS UNIVERSITY MUNICH
FACULTY OF PHYSICS

MASTER THESIS

Daniela Maria Köck

Munich, 25th April 2018

Supervisor: Prof. Dr. Dorothee Schaile

Abstract

Supersymmetry as an extension to the Standard Model can solve the hierarchy problem if supersymmetric particles are present at the TeV scale. If R-parity is conserved, the lightest supersymmetric particle is stable and might be a viable dark matter candidate. The production of charginos and neutralinos might be the dominant production mode of supersymmetry at the LHC, if squarks and gluinos are beyond the reach of the LHC. In this thesis, a search for chargino and neutralino production with 36.1 fb^{-1} of $\sqrt{s} = 13 \text{ TeV}$ proton-proton collisions collected with the ATLAS detector is presented. The charginos and neutralinos can decay via W and Higgs bosons into several final states. A final state with exactly two leptons of the same charge, jets and missing transverse energy is analysed. The design of signal regions as well as of validation regions for the WZ diboson background is described. No significant excess over the standard model expectation was observed. Uncertainties considered in the analysis are summarised before interpreting the data in terms of a simplified chargino neutralino model. Chargino masses up to 225 GeV have been excluded for a massless lightest neutralino. Estimating the sensitivity of the analysis using future larger datasets, a maximum discovery significance of 2.92σ was obtained for $\int \mathcal{L} = 140 \text{ fb}^{-1}$.

Zusammenfassung

Falls supersymmetrische Teilchen nahe der TeV Skala realisiert sind, könnte Supersymmetrie als Erweiterung des Standard Modells das Hierarchieproblem lösen. Ist die sogenannte R-Parität in Supersymmetrie erhalten, wäre das leichteste supersymmetrische Teilchen ein möglicher Kandidat für einen Teil der Dunklen Materie. Die Produktion von Charginos und Neutralinos kann der dominante Produktionsmechanismus von Supersymmetrie am LHC sein, falls Squarks und Gluinos außerhalb der kinematischen Reichweite des LHC sind. In dieser Arbeit wird eine Suche nach Charginos und Neutralinos in 36.1 fb^{-1} Proton-Proton Kollisionen, aufgenommen vom ATLAS Detektor bei einer Schwerpunktsenergie von $\sqrt{s} = 13 \text{ TeV}$ am LHC, präsentiert. Das betrachtete Modell beschreibt die Produktion von Charginos und Neutralinos, welche dann in W und Higgs Bosonen sowie die leichtesten supersymmetrischen Teilchen zerfallen. Das kann zu einem Endzustand mit zwei gleich geladenen Leptonen, Jets und fehlender Transversalenergie führen. Innerhalb dieser Arbeit ist die Optimierung von signal-dominierten Parameterräumen beschrieben, gefolgt von der Definition von Validierungsregionen für einen der dominierenden Untergründe, der WZ Diboson Produktion. Es wurde kein signifikanter Überschuss von Daten im Vergleich zur Standard Modell Erwartung beobachtet. Daher werden die Daten innerhalb des vereinfachten Chargino Neutralino Modells interpretiert. Dabei wurden Chargino Massen bis 225 GeV für masselose leichteste Neutralinos mit 95% Sicherheit ausgeschlossen. Abschätzungen der Entdeckungssensitivität in zukünftigen Analysen erreichten eine maximale Signifikanz von 2.92σ für eine integrierte Luminosität von $\mathcal{L} = 140 \text{ fb}^{-1}$.

Contents

1	Introduction	1
2	Theory	3
2.1	The Standard Model of Particle Physics	3
2.1.1	Quantum field theories	3
2.1.2	Gauge symmetries	3
2.1.3	The Higgs mechanism	4
2.1.4	Particle content of the SM	5
2.1.5	Limitations of the SM	6
2.2	Supersymmetry	7
2.2.1	Introduction	7
2.2.2	Supersymmetry breaking	8
2.2.3	Particle spectrum of the MSSM	8
2.2.4	Model considered in this thesis	12
2.2.5	Current status	14
3	Experimental Setup	17
3.1	The Large Hadron Collider	17
3.2	The ATLAS Detector	17
3.2.1	The Inner Detector	19
3.2.2	Calorimeters	20
3.2.3	Muon Spectrometers	20
3.2.4	Trigger System	21
3.2.5	Reconstruction	21
4	Monte Carlo simulation and Data	23
4.1	Data	23
4.2	Monte Carlo simulations	24
4.3	Event cleaning	24
4.4	Trigger strategy	25
4.5	Object definitions	26
5	The WH two same-sign leptons analysis	31
5.1	Standard Model backgrounds	32
5.2	Analysis strategy	34
5.3	The problem of fakes	35

6	Optimisation of the signal regions	37
6.1	Discriminating variables	37
6.2	Optimisation procedure	41
6.3	Signal region definitions	50
6.3.1	Expected Significance	53
7	Background estimation	55
7.1	Fake lepton estimation	55
7.1.1	The generalised Matrix Method	55
7.1.2	Measurement of the real lepton efficiency	56
7.1.3	Measurement of the fake lepton efficiency	56
7.2	Charge Flip estimation	57
7.3	Diboson validation regions	58
8	Treatment of uncertainties	65
8.1	Experimental uncertainties	65
8.1.1	Object definition and weighting uncertainties	65
8.1.2	Fake lepton uncertainties	66
8.1.3	Charge flip uncertainties	67
8.2	Theoretical uncertainties	68
8.3	Summary of uncertainties before the fit	68
9	Results	75
9.1	Expected and observed yields	75
9.2	Statistical interpretation	75
9.2.1	Statistical concepts	78
9.2.2	HistFitter setup	80
9.2.3	Exclusion limits	80
10	Future prospects	85
11	Conclusion	89
A	Appendix	91
A.1	List of MC Samples	91
A.2	Studying the impact of m_T and m_{eff}	97
A.3	Data to MC comparisons for the proposed validation regions	98
	Bibliography	101

1 Introduction

After the Higgs boson discovery in 2012 [1, 2], the Higgs boson properties are probed to high precision. The measurement of the Higgs at the 125 GeV mass scale leads to further questions going beyond the Standard Model of Particle Physics.

Since the scalar Higgs boson mass value is sensitive to new heavy particles and new physics scales, and as new physical phenomena are expected to happen at the Planck scale, therefore entering the calculation of the Higgs boson mass, why is the Higgs boson mass at the electroweak scale? Since dependent on the mass of possible new heavy particles, the Higgs mass could be as high as the Planck scale [3].

Supersymmetry might be able to answer this question through an additional symmetry between bosons and fermions partially cancelling the possibly large radiative loop corrections to the Higgs boson mass. As supersymmetric particles would have the same properties as their Standard Model partners except for spin and mass, the Higgs boson is required to couple to supersym. particles directly. Observing direct couplings of the Higgs boson to supersymmetric particles would therefore be an important requirement for SUSY being able to solve the hierarchy problem. While searching for a direct production of supersymmetric particles, observing a decay via a Higgs boson would offer such a direct coupling evidence. The simplified model considered in this work describes such a decay. It looks for the production of the lightest chargino together with the second-lightest neutralino, both being mass degenerate with each other. The chargino is decaying further into a W boson and the lightest supersymmetric particle, while the second-lightest neutralino is decaying into a Higgs boson and the lightest neutralino. Dependent on the Higgs decay mode and the W boson decay, several final states can be produced by this model. In this analysis a final state with two leptons of the same charge, jets and missing transverse energy is considered. A pair of leptons with the same charge is a rare Standard Model final state, since most of the lepton pairs in the Standard Model are produced in the decays of oppositely charged particles. After introducing the main theoretical concepts (chapter 2) and the experimental setup (chapter 3), the considered data and the simulation used is presented in chapter 4. Before going into details about the chargino neutralino search, an overview of the designed analysis is given in chapter 5. In order to search for the simplified chargino neutralino production described, in this thesis a signal-enhanced parameter space is optimised (section 6), followed by the design of diboson background enhanced parameter spaces 7, after detailing the Standard Model backgrounds. In chapter 8, the considered uncertainties are described, followed by the statistical interpretation of the data in chapter 9. Finally, some future prospects for larger available datasets is given in chapter 10 followed by some conclusions in chapter 11.

2 Theory

2.1 The Standard Model of Particle Physics

The supersymmetric particles searched for within this work are decaying to known particles of the Standard Model of Particle Physics. Therefore this section introduces the concepts of the Standard Model. Starting with the observation of electrons by J.J Thomson in 1897, the Standard Model of Particle Physics was developed further to describe all particles and their interaction, e.g. include the 1964 by Gell-Mann and Zweig proposed constituent of the proton, the quarks [4]. In its form today, the Standard Model is able to predict particle interactions to high precision, with its most recent large success being the prediction of the Higgs boson [1], [2].

2.1.1 Quantum field theories

Quantum field theory is the generalisation of relativistic quantum mechanics to continuous fields. Similar to classical Lagrangian field theory, a system is completely described by its Lagrangian density. Using the principal of least action, by minimising the action given through the Lagrangian density in equation 2.1, the Euler-Lagrange equation in 2.2 determines the equations of motions to a given Lagrangian density, for every field ϕ in the Lagrangian [5].

$$S = \int \mathcal{L}(\phi, \partial_\mu \phi) d^4x \quad (2.1)$$

$$\partial_\mu \left(\frac{\partial \mathcal{L}}{\partial (\partial_\mu \phi)} \right) - \frac{\partial \mathcal{L}}{\partial \phi} = 0 \quad (2.2)$$

2.1.2 Gauge symmetries

Noethers theorem connects symmetries of the Lagrangian with conservation laws. The Standard Model of Particle Physics (SM) is based on the concept of local gauge invariance, this means that the Lagrangian density can be made invariant under transformations like (2.3), where the wave function $\psi(x)$ (dependent on the four-vector x) is

multiplied by an additional, space-time-dependent, 'local', phase $\alpha(x)$ [5].

$$\psi(x) \rightarrow e^{i\alpha(x)}\psi(x) \quad (2.3)$$

The symmetries in the Standard Model are based on the symmetry groups $SU(3)_C \times SU(2)_L \times U(1)_Y$, describing the strong and electroweak interactions. A theoretical explanation of the gauge groups and their Lagrangians can be found in [4], [6] and [7].

2.1.3 The Higgs mechanism

The Higgs mechanism describes the generation of particle masses in the $SU(3)_C \times SU(2)_L \times U(1)_Y$ symmetry, in which ad-hoc particle mass terms in the Lagrangian would break the gauge invariance. The basic principle introduces a complex scalar field Φ (2.4) with a 'mexican hat potential' $V(\Phi)$ shown in equation 2.5 [8] and figure 2.1. By choosing a specific ground state of Φ the $SU(2)_L \times U(1)_Y$ symmetry of the Lagrangian is spontaneously broken into $U(1)_{em}$ [5].

$$\Phi(x) = \frac{1}{\sqrt{2}} [\Phi_1(x) + i\Phi_2(x)] \quad (2.4)$$

$$V(\Phi) = -\mu^2|\Phi|^2 + \lambda^2|\Phi|^4 \quad (2.5)$$

$$\mathcal{L} = (\partial_\mu\Phi)(\partial^\mu\Phi) - V(\Phi) \quad (2.6)$$

By expanding the scalar field around the ground state in azimuthal and radial direction, mass terms for the two W boson fields, W^\pm , and the Z-boson appear, while the photon as gauge boson of $U(1)_{em}$ stays massless. The quark and fermion masses originate through coupling to the scalar Higgs field. On top of the mass generation, an additional massive scalar boson appears, the Higgs boson.

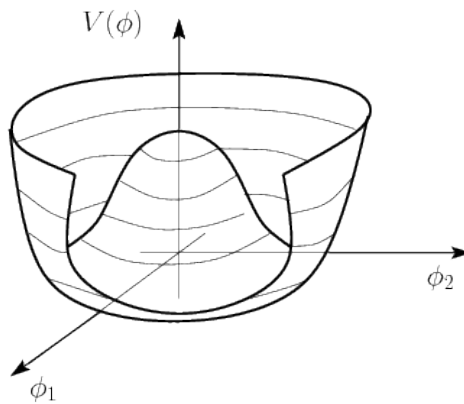


Figure 2.1: Mexican hat potential [9]

2.1.4 Particle content of the SM

Within the last decades, all SM particles have been precisely studied at particle colliders. An overview of all particles in the SM and their masses and charges is shown in table 2.1. The electric charge together with the spin, colour and weak isospin I_3 determines all couplings in the SM. The masses are determined through the coupling of the particles to the Higgs boson.

Particle	electric charge	spin	color	weak I_3 (L)	mass
electron e	-1	1/2	-	+1/2	0.511 MeV
electron neutrino ν_e	0	1/2	-	-1/2	< 2 eV
muon μ	-1	1/2	-	+1/2	105.7 MeV
muon neutrino ν_μ	0	1/2	-	-1/2	< 2 eV
tau τ	-1	1/2	-	+1/2	1776.86 MeV
tau neutrino ν_τ	0	1/2	-	-1/2	< 2 eV
up quark u	+ 2/3	1/2	r,g,b	+1/2	2.2 MeV
down quark d	-1/3	1/2	r,g,b	-1/2	4.7 MeV
charm quark c	+2/3	1/2	r,g,b	+1/2	1.28 GeV
strange quark s	-1/3	1/2	r,g,b	-1/2	96 MeV
top quark t	+2/3	1/2	r,g,b	+1/2	173.1 GeV
bottom quark b	-1/3	1/2	r,g,b	-1/2	4.18 GeV
photon γ	1	-	0	0	0
gluon g	0	1	8	0	0
W boson W	+/- 1	1	-	+/- 1	80.385 GeV
Z boson Z	0	1	-	0	91.1876 GeV

Table 2.1: Overview of all SM particles and their properties, here I_3 is the third weak isospin component [10]

2.1.5 Limitations of the SM

Dark Matter

One of the most striking shortcomings of the Standard Model is its failure to provide a candidate for cold Dark Matter. Dark Matter presents 26.8% of the energy density of our universe, while ‘ordinary’, luminous, matter only makes up 4.9% [11]. Hints for the existence of Dark Matter were already provided in the early 1930’s, by comparing rotational curves of galaxies with the expected velocity distributions calculated by the consideration of visible stars [12]. This showed that non-luminous matter is present in galaxies through its gravitational effects. Colliding galaxies like the bullet cluster [13] [14], provide compelling limitations to the possible Dark Matter self-interaction, since gravitational lensing showed that the mass centres of both galaxies were moving through each other almost unaffected, compared to the deceleration and shock the gas in the galaxies was going under.

The Hierarchy Problem

A shortcoming of the Standard Model from the theoretical point of view is the Higgs mass sensitivity to heavy particles. Calculating one-loop corrections to the Higgs mass, fermionic (2.7) and scalar (2.8) loop contributions depend on a high-energy cut-off scale, as well as the particle mass in the loop [3].

$$\Delta m_H^2 = -\frac{|\lambda_f|^2}{8\pi^2} \Lambda_{UV}^2 + \dots (\propto m_f) \quad (2.7)$$

$$\Delta m_H^2 = \frac{\lambda_S}{16\pi^2} [\Lambda_{UV}^2 - 2m_S^2 \ln(\Lambda_{UV}/m_S) + \dots] \quad (2.8)$$

In contrast to one-loop corrections to masses of fermions or bosons, these contributions are quadratic, not logarithmic, and therefore divergent. This is worrisome from two points of view. First, by choosing a cut-off value of the loop integrals at a ultraviolet cut-off scale, for example the Planck scale, the loop corrections depend on the cut-off scale, which is causing large contributions to the Higgs mass when the cut-off scale is as large as the Planck scale. The Planck scale as upper validity of the SM is a reasonable assumption, since gravitational effects get comparable in size to elementary particle interactions at the Planck scale, and therefore gravity is no longer negligible in particle interactions. Secondly, the mass corrections are proportional to the mass of the contributing particles in the loop and thus proportional to potential unknown heavy particles. This is the key of the hierarchy problem: Why is the Higgs mass at its measured mass at the electroweak scale, while its mass corrections are sensitive to the scale of new physics?

2.2 Supersymmetry

The following section presents an introduction to the basic mathematical description of supersymmetry and its phenomenological consequences. A complete introduction is given in [3] and [15] as well as in [16].

2.2.1 Introduction

The Higgs mass hierarchy problem can only be solved through exact cancellation of fermionic and bosonic contributions to the loop corrections to the Higgs mass. Including an additional symmetry between fermions and bosons, known as supersymmetry (SUSY), introduces a transformation of fermions into bosons and vice versa [3].

$$Q|b\rangle = |f\rangle \quad Q|f\rangle = |b\rangle \quad (2.9)$$

Supersymmetry as an extension to the Standard Model Poincare group presents a unique solution to the hierarchy problem. Unique because it is the only possible connection of space-time and internal symmetries that overcomes the Coleman-Mandula no-go theorem [16]. This theorem presents strict requirements to the fermionic supersymmetry generator Q and leads to the defining SUSY algebra given in equations (2.10) - (2.12), where all spinor indices have been suppressed [3]. In principle, more than one set of generators would be possible, but some extended SUSY models would not allow for parity violating interactions as observed in the Standard Model, therefore only the simplest case with one set of generators is considered in the following.

$$\{Q, Q^\dagger\} = P^\mu \quad (2.10)$$

$$\{Q, Q\} = \{Q^\dagger, Q^\dagger\} = 0 \quad (2.11)$$

$$[P^\mu, Q] = [P^\mu, Q^\dagger] = 0 \quad (2.12)$$

Here P^μ is the four-momentum generator of spacetime translations. As can be seen in 2.12 the SUSY generators commute with spacetime translations. Therefore also the squared mass operator P^2 commutes with Q . As can be seen in equation 2.13, bosonic and fermionic states connected through a supersymmetric transformation have the same mass eigenvalues in an unbroken symmetry.

$$\begin{aligned} \text{from (2.10):} \quad & [Q, P^\mu P_\mu] = 0 \\ \text{using (2.9)} \quad & P^\mu P_\mu Q|b\rangle = P^\mu P_\mu |f\rangle \\ & Q P^\mu P_\mu |b\rangle = m_f^2 |f\rangle \\ & m_b^2 Q|b\rangle = m_f^2 |f\rangle \quad \Rightarrow m_b = m_f \end{aligned} \quad (2.13)$$

Since supersymmetric particles would already have been seen at collider experiments if SM and SUSY particles had the same masses, SUSY needs to be a broken symmetry to allow for different masses of SM particles and their SUSY partners. The concept of supersymmetry breaking is sketched in the following section.

2.2.2 Supersymmetry breaking

Since no supersymmetric particles have been observed so far, the symmetry must be broken. Currently, the knowledge about this breaking mechanism is limited. But the mechanism of the breaking has a large impact on the supersymmetric parameters defining coupling strengths and masses of SUSY particles. For the Minimal Supersymmetric Standard Model, the smallest possible extension of the SM to supersymmetric interactions, the breaking needs to be soft, so that SUSY still potentially provides a solution to the hierarchy problem.

2.2.3 Particle spectrum of the MSSM

The Minimal Supersymmetric Standard Model orders the single particle states into irreducible representations of the SUSY algebra, so called supermultiplets, containing the same amount of fermionic and bosonic degrees of freedom.

A chiral or matter supermultiplet consists of a single Weyl fermion¹ with two helicity eigenstates and therefore two degrees of freedom. This is completed with two real scalar fields, naturally combined into a complex scalar field, with two degrees of freedom. A gauge supermultiplet consists of a vector boson of spin 1 with two helicity eigenstates and a spin 1/2 Weyl-fermion, also with two degrees of freedom. The standard model quarks and leptons are part of a chiral supermultiplet, completed through scalar quarks (squarks, denoted \tilde{q}) and scalar leptons (sleptons, denoted $\tilde{\ell}$). Since a SUSY transformation conserves all internal charges, also the electroweak hypercharge, there are separate multiplets for left-handed and right-handed SM particles. The subscript L or R in squarks and sleptons emphasises this separation, where the index has only a helicity reference to the SM partner (since scalar squarks and sleptons do not have helicity eigenstates). SM vector bosons (W^+ , W^- , W_0 and B_0) are part of a gauge multiplet, where their SUSY partners are referred to as gauginos (Wino, Bino). The SM Higgs boson fits into a chiral multiplet, where two Higgs doublets are needed within supersymmetric models to avoid gauge anomalies. The H_u doublet is giving all up type quarks their mass, whereas the H_d gives all down type quarks and leptons their masses. The complete set of chiral and gauge multiplets is summarised in table 2.2 and 2.3, where the multiplets are ordered according to their $SU(2)_L$ doublets and singlets for the first generation of quarks and leptons exemplarily.

¹ A Dirac spinor can be decomposed into two two-dimensional representations of the Lorentz group, called Weyl spinors [5]

Names		spin 0	spin 1/2	SU(3) _C , SU(2) _L , U(1) _Y
squarks, quarks (x 3 families)	Q	$(\tilde{u}_L \tilde{d}_L)$	$(u_L d_L)$	$(\mathbf{3}, \mathbf{2}, \frac{1}{6})$
	\bar{u}	\tilde{u}_R^*	u_R^\dagger	$(\bar{\mathbf{3}}, \mathbf{1}, -\frac{2}{3})$
	\bar{d}	\tilde{d}_R^*	d_R^\dagger	$(\bar{\mathbf{3}}, \mathbf{1}, \frac{1}{3})$
sleptons, leptons (x 3 families)	L	$(\tilde{\nu} \tilde{e}_L)$	(νe_L)	$(\mathbf{1}, \mathbf{2}, -\frac{1}{2})$
	\bar{e}	\tilde{e}_R^*	e_R^\dagger	$(\mathbf{1}, \mathbf{1}, 1)$
Higgs, higgsinos	H _u	$(H_u^+ H_u^0)$	$(\tilde{H}_u^+ \tilde{H}_u^0)$	$(\mathbf{1}, \mathbf{2}, +\frac{1}{2})$
	H _d	$(H_d^0 H_d^-)$	$(\tilde{H}_d^0 \tilde{H}_d^-)$	$(\mathbf{1}, \mathbf{2}, -\frac{1}{2})$

Table 2.2: Chiral supermultiplets in the MSSM. The spin 1/2 fields are conjugated to present left-handed Weyl fermions (from [3])

Names	spin 1/2	spin 1	SU(3) _C , SU(2) _L , U(1) _Y
gluino, gluon	\tilde{g}	g	$(\mathbf{8}, \mathbf{1}, 0)$
winos, W bosons	$\tilde{W}^\pm \tilde{W}^0$	$W^\pm W^0$	$(\mathbf{1}, \mathbf{3}, 0)$
bino, B boson	\tilde{B}^0	B^0	$(\mathbf{1}, \mathbf{1}, 0)$

Table 2.3: Gauge supermultiplets in the MSSM (from [3])

Higgs bosons in the MSSM

With the additional Higgs doublet introduced in the MSSM and the corresponding superpartners, the MSSM Higgs sector has eight degrees of freedom. Three of them generate the electroweak gauge boson masses. The five other degrees of freedom manifest themselves in additional particles. Two CP-even, neutral Higgs bosons, h^0 and H^0 appear, where h^0 is considered to be the SM Higgs boson. In addition, a CP-odd transforming neutral Higgs, A^0 , and two charged Higgs bosons, H^+ and H^- , emerge.

Charginos and neutralinos in the MSSM

The gaugino fields of the MSSM mix with each other since their quantum numbers are identical. This leads to neutral and charged mass eigenstates (called neutralinos and charginos respectively). This mixing is visible in the MSSM Lagrangian mass terms ((2.14), (2.15)) in the mixing matrices, given in (2.16) and (2.17) [3].

$$\begin{aligned}\mathcal{L}_{\text{neutralino mass}} &= -\frac{1}{2}(\psi^0)^T \mathbf{M}_{\tilde{\chi}_j^0} \psi^0 + c.c., \\ \text{with } \psi^0 &= (\tilde{B}^0, \tilde{W}^0, \tilde{H}_d^0, \tilde{H}_u^0)\end{aligned}\quad (2.14)$$

$$\begin{aligned}\mathcal{L}_{\text{chargino mass}} &= -\frac{1}{2}(\psi^\pm)^T \mathbf{M}_{\tilde{\chi}_i^\pm} \psi^\pm + c.c., \\ \text{with } \psi^\pm &= (\tilde{W}^+, \tilde{H}_u^+, \tilde{W}^-, \tilde{H}_d^-)\end{aligned}\quad (2.15)$$

The parameters of the mixing matrices originate from the soft supersymmetry breaking Lagrangian, $\mathcal{L}_{\text{soft}}$. M_1 and M_2 are the bino and wino mass parameters respectively, μ the higgsino mass parameter. The vacuum expectation values $\langle H_{u/d}^0 \rangle$ are noted as $v_{u/d}$, g and g' describe the standard model coupling constants.

$$\mathbf{M}_{\tilde{\chi}_i^0} = \begin{pmatrix} M_1 & 0 & -g'v_d/\sqrt{2} & g'v_u/\sqrt{2} \\ 0 & M_2 & gv_d/\sqrt{2} & -gv_u/\sqrt{2} \\ -g'v_d/\sqrt{2} & gv_d/\sqrt{2} & 0 & \mu \\ g'v_u/\sqrt{2} & -gv_u/\sqrt{2} & -\mu & 0 \end{pmatrix}\quad (2.16)$$

$$\mathbf{M}_{\tilde{\chi}_j^\pm} = \begin{pmatrix} \mathbf{0} & \mathbf{X}^T \\ \mathbf{X} & \mathbf{0} \end{pmatrix}, \text{ with } \mathbf{X} = \begin{pmatrix} M_2 & gv_u \\ gv_d & \mu \end{pmatrix}\quad (2.17)$$

Depending on the comparable size of M_1 , M_2 and μ , neutralinos can be bino-dominated ('bino-like'), wino-dominated ('wino-like'), higgsino-dominated ('higgsino-like') or mixed with no clear dominating component. In table 2.4 the mass and gauge eigenstates of charginos and neutralinos are summarised.

Names	mass eigenstates	gauge eigenstates
neutralinos	$\tilde{\chi}_1^0, \tilde{\chi}_2^0, \tilde{\chi}_3^0, \tilde{\chi}_4^0$	$\tilde{B}^0, \tilde{W}^0, \tilde{H}_u^0, \tilde{H}_d^0$
charginos	$\tilde{\chi}_1^\pm, \tilde{\chi}_2^\pm$	$\tilde{W}^\pm, \tilde{H}_u^\pm, \tilde{H}_d^\pm$

Table 2.4: Mass and gauge eigenstates of neutralinos and charginos

Interactions in the MSSM

Interactions in the MSSM follow the same regularities as in the SM. For the specific supersymmetric model considered in this thesis and explained in the next paragraph, the vertices shown in figure 2.2 are the most interesting ones. Possible vertices of neutral binos and winos as well as charged winos are shown [17]. This elucidates the couplings of the corresponding fields, manifesting in the chargino neutralino mass eigenstates constructed from (2.14) to (2.17). The composition of the charginos and neutralinos determines the dominating interactions. In figure 2.3 the production of charginos and neutralinos at hadron colliders is shown, each of the depicted processes and each vertex can be associated to one of the field interaction vertices in figure 2.2. Since charginos and neutralinos are not colour-charged, they are produced via electroweak interactions.

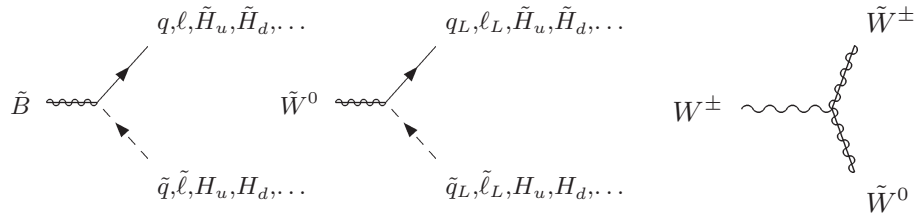


Figure 2.2: Wino and bino field vertices in the MSSM [17]

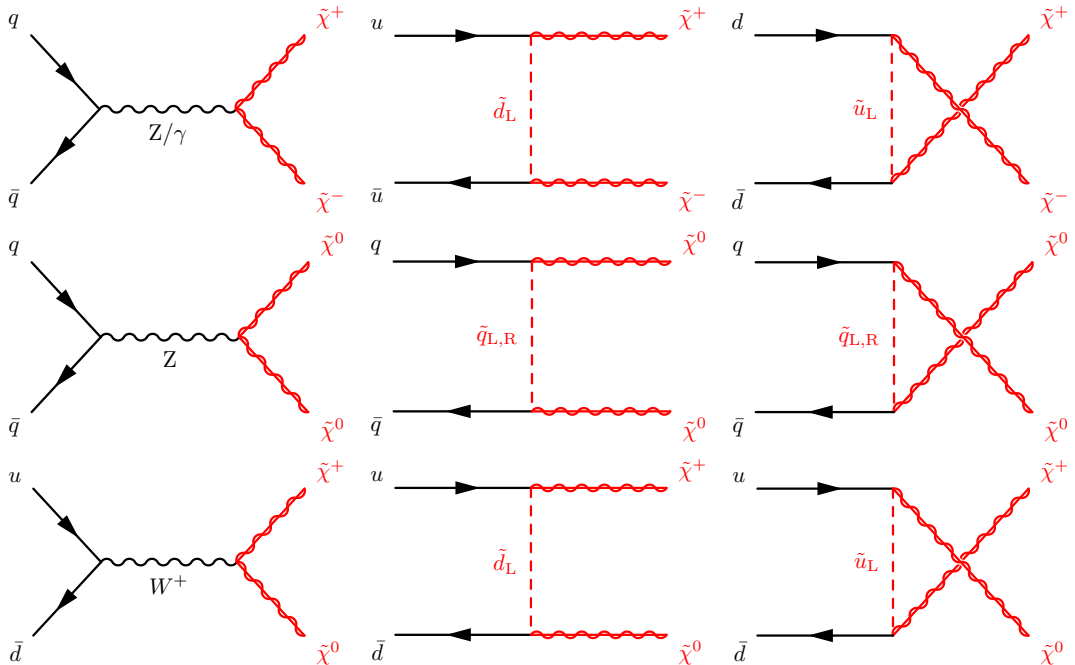


Figure 2.3: Electroweak production of neutralinos and charginos at hadron colliders, adapted from [3].

R-parity conservation

To guarantee baryon (B) and lepton number (L) conservation and thus proton stability in supersymmetric models, conservation of a new quantum number, called R-parity, is introduced (2.18) [3].

$$P_R = (-1)^{3(B-L)+2s} \quad (2.18)$$

Connecting the baryon and lepton number as well as the spin (s) of a particle, the R-parity is equal to +1 for Standard Model particles and -1 for SUSY particles. R-parity conservation suppresses possible L and B violating terms in the MSSM Lagrangian and has some remarkable phenomenological consequences:

- SUSY particles can only be produced in pairs,
- SUSY particles can only decay into an odd number of SUSY particles,
- The lightest supersymmetric particle (LSP) is stable, since it cannot decay further into only SM particles without violating R-parity,
- The LSP is thus stable, weakly interacting and presents a good DM candidate.

It should nevertheless be clear that R-parity is an additionally introduced, though well-motivated symmetry through an additional quantum number, but not the only way to guarantee proton stability in supersymmetric models. Further perspectives on the possibility of R-parity violating couplings are given in [3]. Within this thesis, R-parity conservation is considered.

2.2.4 Model considered in this thesis

Similar to many ATLAS SUSY analyses, in this thesis a simplified model [18] was used as a way to search for supersymmetric particles. Simplified models originate from a complete MSSM model, in which all particles not participating in the interaction are considered to be very heavy. This causes them to decouple from the considered process. The simplified model considered in this thesis is depicted in figure 2.4

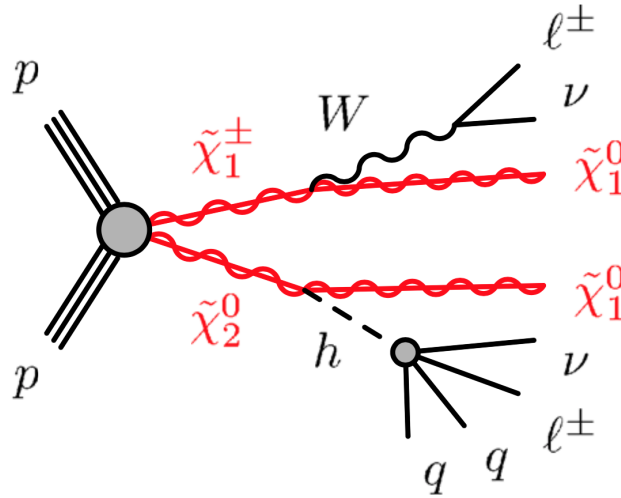


Figure 2.4: Benchmark model of chargino neutralino pair production considered in this analysis [19]

It considers the electroweak production of the second lightest neutralino and the lightest chargino. Both decay into a Higgs boson or a W boson, respectively, and the lightest neutralino. These decays are assumed to be the only possible decays. W and Higgs bosons decay either into leptons (leptonically) or quarks and gluons (hadronically). The Higgs boson has all possible Higgs decay modes. The final state considered in this thesis is a two lepton final state, with both leptons having the same electric charge (referred to as same-sign leptons). This assumption vetoes around 50 % of the possible decay modes of chargino neutralino production into two leptons, but is suppressing standard model backgrounds with two leptons (more about the SM backgrounds see chapter 5). Since the neutralino is considered to be the lightest supersymmetric particle, it leaves the detector without signal and results in missing transverse energy. The lightest chargino and second lightest neutralino are wino-like, which causes both to be dependent on the same MSSM mass parameter M_2 , and can therefore be degenerate. The LSP is bino-like, dependent on M_1 . Choosing the mass parameters to be ordered like $M_1 < M_2 \ll \mu$ can cause the $\tilde{\chi}_1^\pm, \tilde{\chi}_2^0, \tilde{\chi}_1^0$ mass hierarchy [20] shown in figure 2.5 and all other charginos and neutralinos are considered to be heavy and without reach of the LHC. For the Higgs boson to be produced on-shell the mass difference between the $\tilde{\chi}_1^\pm$ and $\tilde{\chi}_1^0$ needs to be larger than 130 GeV.

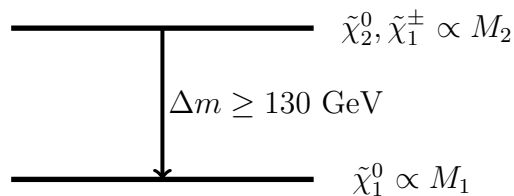


Figure 2.5: Mass hierarchy in the chargino-neutralino pair production scenario

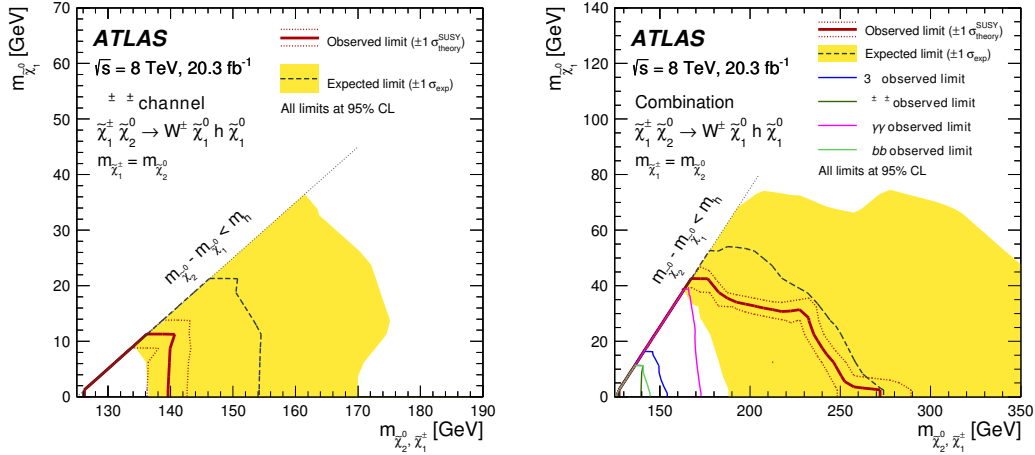
The observed dark matter abundance can be reached through a light, bino $\tilde{\chi}_1^0$ LSP, motivating the choice of a bino LSP [21]. The lightest chargino decaying into a bino LSP and a W boson is well motivated through the charged Wino component in the lightest chargino (see vertices in figure 2.2).

An additional benefit of the choice of this simplified model is the direct coupling of the Higgs boson to two SUSY particles. Discovering this decay would be a direct evidence of SUSY particles contributing to Higgs boson mass corrections and therefore possibly solving the Hierarchy problem.

2.2.5 Current status

A previous analysis looking for the simplified chargino neutralino production described in section 2.2.4 used 8 TeV data with a total integrated luminosity of 20.3 fb^{-1} . This analysis was not observing any deviation from the SM expectation and therefore set limits on the chargino and neutralino masses. In figure 2.6a, the excluded parameter space through the two same-sign leptons final state can be seen. The analysis was able to exclude chargino masses up to 136 GeV for a massless LSP. Several Higgs and W boson decay channels², leading to different final states, were statistically combined in the last iteration of the analysis [22]. In the combined exclusion, chargino masses up to 250 GeV have been excluded. Comparing the previous 8 TeV result to other chargino neutralino searches within ATLAS, the WH limit seems rather small. This can be due to the constraint of an on-shell Higgs boson, restraining the possible phase space. The model presented here is especially interesting not because of a possible large mass reach of charginos and neutralinos, but because of its direct coupling of charginos and neutralinos to the Higgs boson, which is a requirement of supersymmetric models. A Higgs coupling to stop quarks typically has a larger contribution to the Higgs mass corrections [3], but has not been probed so far. Therefore the chosen simplified model with the bino LSP and wino $\tilde{\chi}_1^\pm$, $\tilde{\chi}_2^0$ enabling a dominant on-shell Higgs decay is a rare probe of a direct coupling of SUSY particles to the Higgs boson, necessary for stabilising the Higgs boson mass.

²The decay channel of charginos and neutralinos decaying via a on-shell Higgs boson and a on-shell W-boson is referred to as WH in this work



(a) Exclusion limit in the WH SS analysis (b) Exclusion limit with all WH analysis combined

Figure 2.6: Previous ATLAS analysis searching for the simplified chargino neutralino production presented [22]

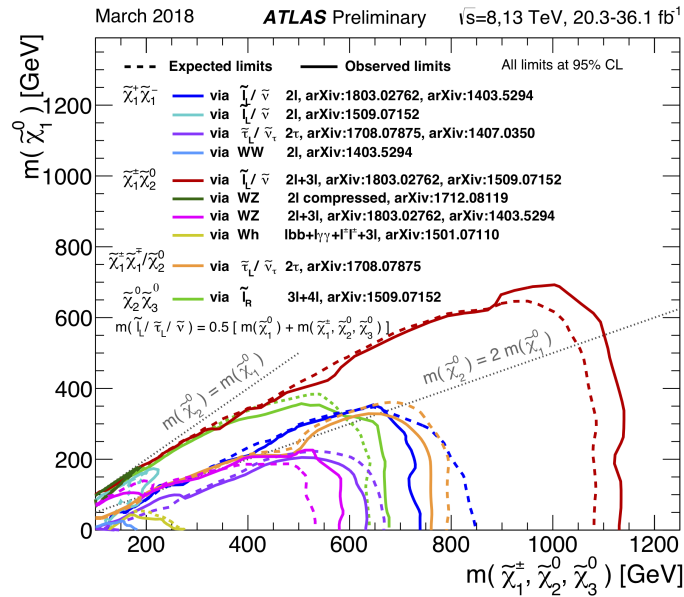


Figure 2.7: Summary plot of the ATLAS searches for electroweak production of SUSY particles, in the chargino-neutralino mass plane [23]

3 Experimental Setup

One of the largest research centres in the world, CERN (Conseil Européen pour la Recherche Nucléaire) or the European Organization for Nuclear Research, is located at the franco-swiss border. It has 22 member states and has a wide range of experiments and several particle (de)accelerators. The largest accelerator at CERN is the Large Hadron Collider, which will be presented in the next section [24].

3.1 The Large Hadron Collider

The Large Hadron Collider (LHC) with its 27 km (26659m) circumference is the largest particle collider built so far. It lies in average 100 m under ground, with a tilt of 1.4% [25]. It constitutes of 9593 magnets, 1232 of which being main dipole magnets to obtain the circular particle trajectory. Eight radiofrequency cavities accelerate the protons (or ions) in two separate beam pipes in opposite directions along the ring, reaching 6.5 TeV proton energy. The distance between the proton ‘bunches’, packages of protons accelerated together, is approximately 7.5m, or 25ns. Beginning from a hydrogen bottle, the protons first get accelerated in the linear accelerator LINAC2 to 50 MeV, secondly, they are accelerated to 1.4 GeV with the Proton Synchrotron Booster (PSB). Afterwards they are inserted into the Proton Synchrotron (PS), brought up to 26 GeV and further accelerated to 450 GeV by the Super Proton Synchrotron (SPS). Eventually, the proton bunches get injected into the LHC, in which they are brought to 6.5 TeV in roughly 20 minutes [26]. The accelerator chain is shown in figure 3.1, together with an overview of experiments and accelerators at CERN. At the LHC, there are seven experiments using the proton or ion beams: ALICE (A Large Ion Collider Experiment), ATLAS (A Toroidal LHC ApparatuS), CMS (Compact Muon Solenoid), LHCb (Large Hadron Collider beauty), LHCf (Large Hadron Collider forward), TOTEM (Total Elastic and diffractive cross section measurement) and MoEDAL (Monopole and Exotics Detector at the LHC). The four large particle-detectors ATLAS, CMS, LHCb and ALICE are installed in own caverns at LHC collisions points [25].

3.2 The ATLAS Detector

The ATLAS detector is a 44 m long and 25 m high particle detector, being the largest detector at the LHC. Different layers of detectors are installed around the beam pipe,

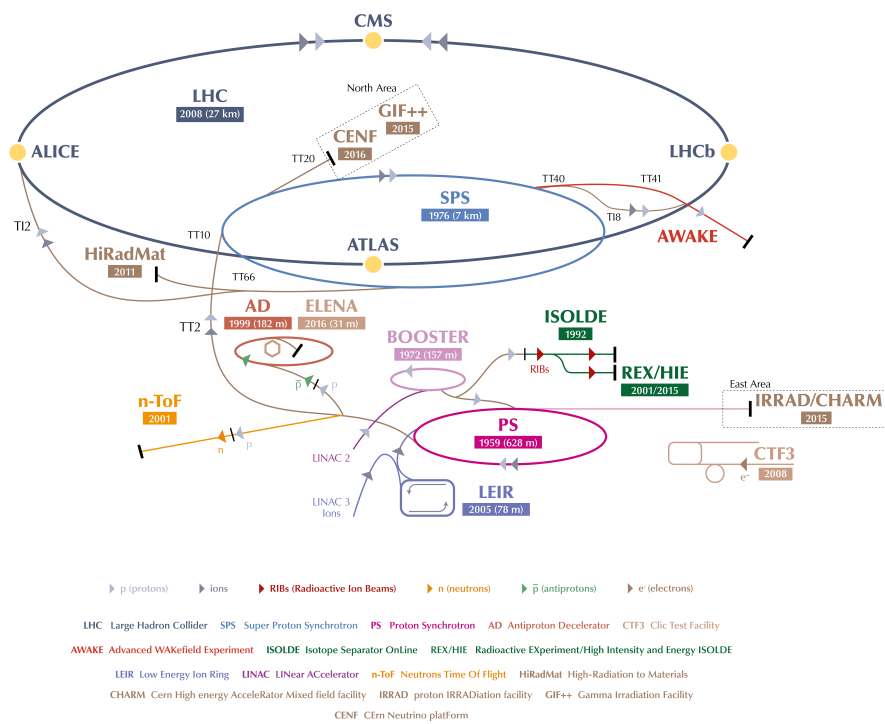


Figure 3.1: The CERN accelerator complex [27]

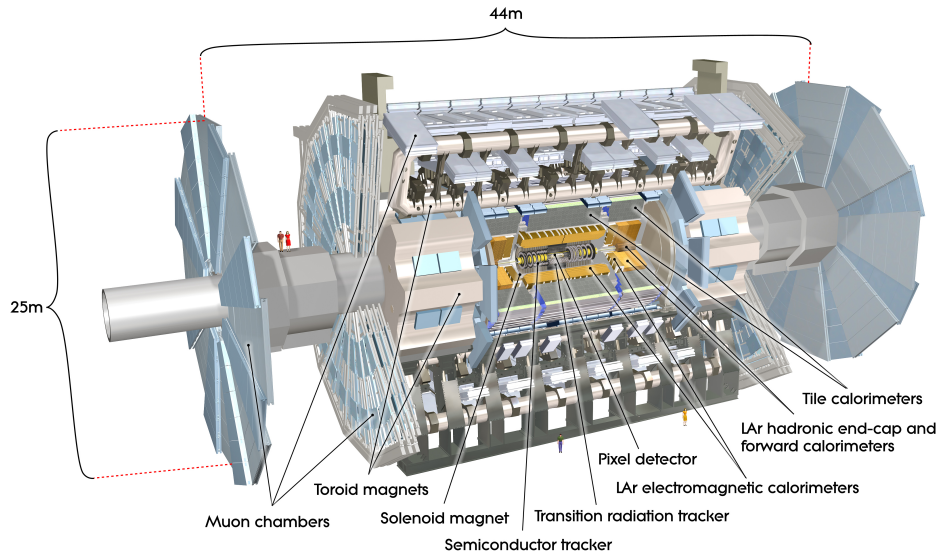


Figure 3.2: Computer generated image of the ATLAS detector [29]

surrounding the collision point. Detector layout and structure vary between the ‘barrel’ region, symmetrically surrounding the beam pipe, and the end-caps, enclosing the forward regions - a computer generated overview of the ATLAS detector is given in Figure 3.2. The following sections present the detector parts in brief, beginning with the subdetector closest to the beam pipe and moving further out. All details about the detector layout are taken from [28]. ATLAS is using a right-handed coordinate system, with the z-axis being aligned with the beam axis. The y-axis points upwards, whereas the x-axis points towards the centre of the LHC. The particle trajectories are given in terms of the pseudorapidity [10]:

$$\eta = -\ln \tan \left(\frac{\theta}{2} \right) \quad (3.1)$$

3.2.1 The Inner Detector

The Inner Detector (ID) is the innermost detector part, directly enclosing the beam pipe. It reaches up to 1150 mm [28] radial distance to the beam pipe. Pixel and silicon microstrip trackers (SCT) provide tracking information in a $|\eta| < 2.5$ range. Typically three pixel and eight silicon microstrip layers are crossed by each track. Additional to the high-precision pixel and SCT detectors, the outermost part of the ID is the transition radiation tracker (TRT), with straw tubes providing R - ϕ information with typically 36 hits in the TRT per track. The TRT covers an η range up to $|\eta| = 2.0$ [28]. In 2014, an additional layer close to the beam pipe (at 3.3 cm radial distance to the beam axis) was installed, the Insertable B-Layer (IBL) [30, 31]. This improved

the tracking performance close to the beam pipe significantly. The reconstruction of the primary vertex (PV) in the collision and the longitudinal (z_0) and transverse (d_0) impact parameter³ of a track to this vertex is key in different reconstruction and identification steps, as described in chapter 4. The primary vertex in a collision is the vertex with the highest sum of squared transverse momenta tracks leaving from that vertex. The inner detector is enclosed in a 2T solenoid magnet field. This allows for momentum and charge reconstruction in the ID.

3.2.2 Calorimeters

Energy measurements are performed in the calorimeters. They are designed to fully absorb a high percentage of traversing particles through shower building. The electromagnetic calorimeter is based on bremsstrahlung and pair-creation of particles, leading to the traversing particle showering and leaving energy as deposits in the electromagnetic calorimeter if the traversing particle is electromagnetically interacting. The hadronic calorimeter also reconstructs the energy via shower properties, with the showering based on nuclei-interactions. The electromagnetic calorimeter has > 22 radiation lengths⁴ in the barrel region and > 24 in the end-cap [28]. The electromagnetic calorimeter (ECal) is placed next to the ID, the barrel part of the ECal ($|\eta| < 1.475$) is a lead-liquid-argon sampling calorimeter. Enclosing the electromagnetic calorimeter, the hadronic calorimeter is a steel-scintillator sampling calorimeter, with a barrel region of $|\eta| < 1.0$ and an extended barrel region with $0.8 < |\eta| < 1.7$, with a size of 9.7 interaction lengths. The hadronic calorimeter in the end-cap is also built with liquid argon [28].

3.2.3 Muon Spectrometers

The muon spectrometer is the outermost detector part, with only muons, neutrinos and only weakly interacting particles passing the calorimeter system. Due to toroid magnets, the muon momentum can be additionally measured in the muon system. The muon system consists of four detector types. Most of the precision measurements are done with monitored drift tubes (MDT), while for large η , cathode strip chambers (CSC's) are used. For triggering muons in the barrel region, Resistive Plate Chambers (RPC's) are used, whereas in the end-caps Thin Gap Chambers (TGC's) are used for triggering.

³The impact parameter describes the distance of a scattered particle from the collision centre, if it would have continued on its unscattered path [4]

⁴The radiation length (interaction length) describes the distance after which the initial energy of the particle has decreased to $1/e$ due to radiation losses (nuclei interactions) [32]

3.2.4 Trigger System

The trigger system in ATLAS guarantees that the event rate is low enough to write it on tape and selects physics processes of interest. A hardware component, the level one (L1) trigger, is followed by a software based trigger, the High-Level-Trigger (HLT). The L1 trigger is based on calorimeter and muon spectrometer information, selecting regions of interest and passing it to the HLT, reducing the event rate from around 30 MHz to 100 kHz. Within $2.5 \mu\text{s}$ the L1 trigger decides to keep an event or not. The High-Level-Trigger is able to perform reconstruction algorithms using higher granularity information and the whole detector information. Reducing the event rate from 100 kHz to approximately 1 kHz, the HLT has a processing time of around 200 ms [33].

3.2.5 Reconstruction

All detector components together are used to identify the traversing particles and measure their properties. As sketched in figure 3.3, charged particles like electrons, muons or charged constituents of jets leave a track in the inner detectors, through ionisation charges. Neutral particles like neutrons, photons or neutrinos leave the ID without signal. Electrons and photons leave the majority of their energy in the electromagnetic calorimeters, whereas jets, neutrons and protons get stopped in the hadronic calorimeter. Muons cause hits in the inner detector parts, but traverse through the calorimeters without suffering large energy losses, therefore they lead to only small energy deposits (since muons are minimum ionising particles). They thus traverse to and leave tracks in the muon spectrometer. Neutrinos and other electrically neutral, stable, only weakly interacting particles, leave the detector without signal. They can be reconstructed by momentum considerations, since no momentum in the transverse plane of the collision was present before the collision. The missing transverse momentum reconstruction is further described in 4.5.

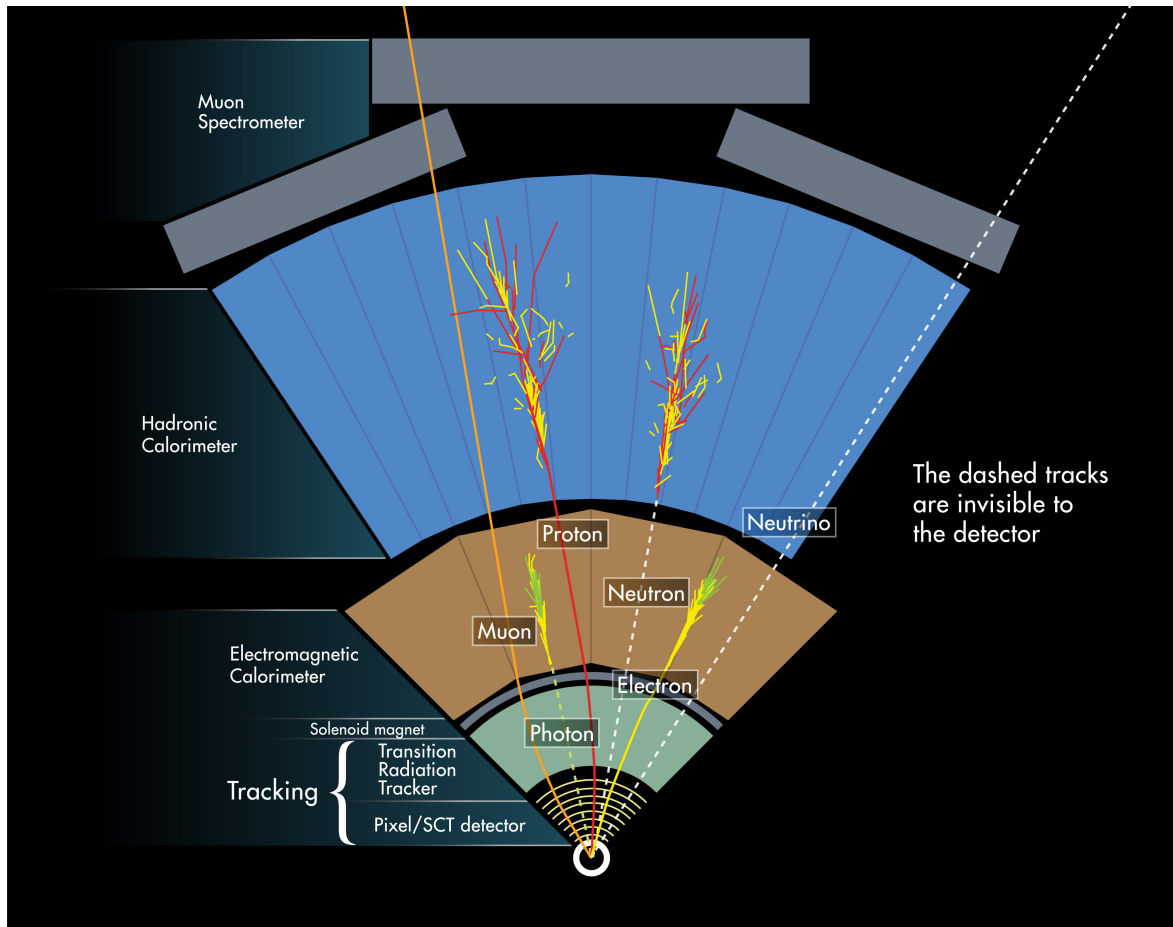


Figure 3.3: Reconstruction principle of several particles [34]

4 Monte Carlo simulation and Data

4.1 Data

For this analysis, proton-proton collisions recorded by the ATLAS experiment in 2015 and 2016 at a centre-of-mass energy of $\sqrt{s} = 13$ TeV are used.

A total of $\int \mathcal{L} dt = 36.1 \text{ fb}^{-1}$ data, consisting of 3.2 fb^{-1} from the 2015 data-taking and 32.86 fb^{-1} from the 2016 collisions are used. The luminosity \mathcal{L} can be calculated through equation (4.1) and is a measure of the amount of particles in the accelerator and how many particles are available for collisions [35]:

$$\mathcal{L} = \frac{N_1 N_2 f N_b}{4\pi \sigma_x \sigma_y} \quad (4.1)$$

The number of particles per bunch N_1 and N_2 enters this expression for both colliding bunches, and also the bunch collision frequency f , the number of bunches N_b and the spacial bunch extensions $\sigma_{x/y}$, assuming a Gaussian bunch shape. In figure 4.1a and 4.1b, the peak luminosities reached by the LHC in proton-proton collisions in 2015 and 2016 is given.

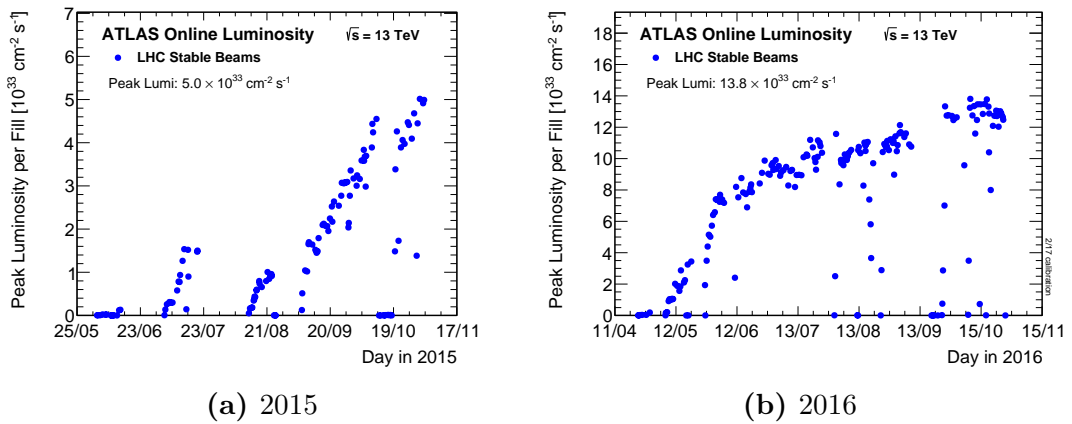


Figure 4.1: Peak Luminosity in 2015 and 2016 [36, 37]

4.2 Monte Carlo simulations

To get an estimation of the expected SM processes in the recorded proton-proton collisions and to predict the events of possible SUSY processes, Monte Carlo (MC) simulations are used. Different general-purpose MC generators are used within this analysis to generate predictions for all considered SM and SUSY processes. More details on the considered SM processes are given in section 5.1. Monte Carlo generation is based on consecutive steps, separating the process in parts where perturbative QCD can be used (small α_S , short distance) and other, non-perturbative regimes, where approximative methods need to be taken into account. The simulation can be separated into [38]:

- **Hard process:** a parton-level interaction with high momentum-transfer or heavy produced particles, calculated with perturbative QCD
- **Parton shower:** radiation of gluons from the initial and final state particles
- **Hadronisation:** building of colour-singlets out of the final state quarks and gluons, non-perturbative
- **Underlying event:** parton collisions happening simultaneously to the hard process, 'pile-up', calculated with perturbative QCD
- **Unstable particle decays:** decay of unstable hadrons formed during hadronisation

In order to obtain the amount of events of a simulated process at a given luminosity the simulated events need to be normalised to the cross section σ of the process. This is done through the reweighting given in (4.2), where N_{MC} is the number of simulated MC events, ϵ is the filter-efficiency and the k-factor k . The filter-efficiency represents the rate of events passing a certain requirement e.g asking for two leptons (two lepton filter). The k-factor accounts for next-to-leading-order corrections to the matrix element calculation.

$$\frac{\int \mathcal{L} dt \times \sigma \times \epsilon_f \times k}{N_{MC}} \quad (4.2)$$

As a final step, to be able to compare Monte Carlo simulation and data, the MC is run through a detector simulation done with **Geant4** [39] or a fast simulation [40] and is further treated like data.

4.3 Event cleaning

Data events recorded need to pass a selection of event cleaning requirements to be considered in the analysis. Those criteria are:

- **Jet Cleaning:** to suppress non-collision background and detector noise, events are required to pass the LooseBad requirement of the JetCleaningTool, described in [41]
- **Primary Vertex:** events must have a primary vertex with the highest quadratic sum of p_T of associated tracks, with at least two associated tracks to this vertex
- **Bad Muon Veto:** an event containing a muon with $\sigma(q/p)/|q/p| > 0.2$ is removed, with q the charge and p the momentum of the muon and $\sigma(q/p)$ the uncertainty on the q/p measurement, this suppresses muon mis-measurements
- **Cosmic Muon Veto:** events containing cosmic muons are rejected. Based on the longitudinal and transverse impact parameters z_0, d_0 with respect to the PV as a discriminant ($|z_0| < 1.0$ mm, $|d_0| < 0.2$ mm required). Cosmic muon tracks crossing the detector are not originating from the collision point and can be suppressed through the impact parameters.

4.4 Trigger strategy

As described in section 3.2.4, the ATLAS trigger system is based on the Level 1 (L1) trigger in hardware, followed by the HLT. The High Level Trigger nomenclature relevant in this thesis is given through the following scheme (adapted from [42]):

HLT_Base_Identification_Isolation_Additional

The Base is given through the object multiplicity and the p_T threshold, e.g 2e17 describes a di-electron trigger with a requirement of $p_T > 17$ GeV on the two electrons. This basic information is followed by additional criteria on the identification and isolation requirement, followed by additional information (details in [42]). The identification is based on a likelihood discriminant, using information from the electromagnetic calorimeter, the track quality, TRT information and matching of tracks to electromagnetic clusters. It has three main working points, lhloose, lhmedium and lhtight. An additional criteria on the isolation can be introduced for further rate reduction. The isolation is based on different criteria on the sum of p_T of tracks around the considered lepton in comparison to its energy deposit in the calorimeter. This gives an estimate of the momentum originating from tracks not belonging to the lepton.

After studying the trigger efficiency in data and Monte Carlo for the main SM backgrounds and the simplified chargino neutralino model, a logical OR of single lepton and di-lepton trigger was chosen to be used. The combination of single-lepton trigger with the dilepton trigger has shown to raise the efficiency compared to di-lepton trigger alone (see [19]). A summary of the single-lepton and di-lepton trigger used is shown in table 4.1 and 4.2. The trigger efficiency in dependence of the lepton p_T is not well

	2015	2016
single electron	HLT_e24_lhmedium_L1EM20VH HLT_e60_lhmedium HLT_e120_lhloose	HLT_e26_lhtight_nod0_ivarloose HLT_e60_lhmedium_nod0 HLT_e140_lhloose_nod0
single muon	HLT_mu20_iloose_L1MU15 HLT_mu40	HLT_mu26_imedium HLT_mu50

Table 4.1: Single-lepton trigger used in the WH SS analysis

	2015	2016
di-electron	HLT_2e12_lhloose_L12EM10VH	HLT_2e17_lhvloose_nod0
di-muon	HLT_mu18_mu8noL1	HLT_mu22_mu8noL1
electron-muon	HLT_e17_lhloose_mu14	HLT_e17_lhloose_nod0_mu14
	HLT_e7_lhmedium_mu24	HLT_e7_lhmedium_nod0_mu24

Table 4.2: Dilepton trigger used in the WH SS analysis

simulated in MC estimations. To have an identical trigger behaviour in data and MC, trigger scale factors need to be applied on Monte Carlo. Trigger scale factors depend on the lepton momentum and are given by the ratio of the trigger efficiency for data over the trigger efficiency in Monte Carlo. Lepton trigger efficiencies are derived by the combined performance groups [43, 44]. In the combination of single and di-lepton trigger, the scale factors need to be combined event-by-event. This is done using the `TrigGlobalEfficiencyCorrectionTool` [45].

4.5 Object definitions

Within this thesis, physics objects like electrons, muons or jets are separated in consecutive steps. In a first step, 'baseline' objects are defined with a small purity. The aim of this step is to have a high acceptance for the several objects and the baseline objects are e.g used to construct the missing transverse momentum in an event. After an overlap procedure to remove ambiguities between baseline objects, stricter requirements on the isolation and identification of the objects are placed. Those 'signal' objects are designed to have a high identification efficiency and are used in the analysis as physical particles.

Electrons

Baseline electrons are required to pass the `LooseAndBLayerLLH` identification requirement, have a transverse momentum larger than 10 GeV and the calorimeter clusters should be within $|\eta^{\text{clust}}| < 2.47$. The identification is based on a likelihood method, providing loose, medium and tight working points, the `LooseAndBLayerLLH` requirement used here is taking the innermost tracking part, the insertable B-layer tracking information into account in the likelihood [46] (as opposed to the loose requirement). Signal electrons are required to pass the `FixedCutTight` isolation working point, have a transverse momentum larger than 25 GeV, a identification quality of `MediumLH` and pass the overlap removal procedure described further below. The isolation working point `FixedCutTight` has fixed cuts on the isolation parameters $\text{topoetcone20}/p_T < 0.06$ and $\text{ptvarcone20}/p_T < 0.6$. Both present the sum of transverse energy of calorimeter clusters or momentum of tracks around the considered electron and restrict electron energy contributions from other particles than the electron. On top of that, the `ElectronChargeIDSelector` [47] is applied to reduce leptons with a charge misreconstruction. The `medium 97%` working point of this multivariate classifier was used, providing a 97% efficiency for correctly measured electrons. Finally, the longitudinal and vertical impact parameters need to fulfil $|z_0 \sin(\theta)| < 0.5$ mm and $|d_0/\sigma(d_0)| < 5.0$.

Muons

Baseline muons must have `medium` identification quality and have a transverse momentum larger than 10 GeV and lie within $|\eta| < 2.4$. Signal muons are also of `medium` quality, but need $p_T > 25$ GeV and a `GradientLoose` isolation. This isolation working point is p_T dependent in comparison to the previous `FixedCutTight` working point. Additionally, the impact parameters need to fulfil $|z_0 \sin(\theta)| < 0.5$ mm and $|d_0/\sigma(d_0)| < 5.0$, as well as $|d_0| < 0.2$ mm to veto cosmic muons.

More information about the lepton isolation working points is given in [48], on the identification procedure and working points in [46, 49].

Jets

Baseline jets are constructed using the `AntiKt4EMTopo` jet clustering algorithm [50] with a radius parameter of $R = 0.4$ to limit the jet size. They are required to have a transverse momentum of at least 20 GeV and lie within $|\eta| < 2.8$. Signal jets have to undergo the overlap procedure described further below. For jets with $p_T < 60$ GeV and $|\eta| < 2.4$ GeV, the jet vertex tagger working point at 92% is additionally required for pile-up reduction, where the jet vertex tagger (JVT) is a multivariate combination of tracking information related to the primary vertex, designed to suppress pile-up jets [51]. The jet energy is corrected to achieve the true jet energy from the reconstructed jet energy, accounting for e.g. damaged calorimeter cells and different response of

hadronic and electromagnetic calorimeters [52].

b-tagged Jets

B-jets are defined as signal jets, with $|\eta| < 2.5$. The MV2c10 [53] b-tagging classifier is used at a 77% working point. The MV2c10 b-tagging discriminator is using charged particle tracks as input and uses the displaced vertex properties of b-tags, originating from b-meson decays. This information is used in three distinct algorithms which are then later combined into the MV2 classifier. The MV2c10 boosted decision tree uses 10 percent of charm jets and 90 percent of light jets in the training. The composition of the training sample influences the performance of the final classifier. The MV2c10 algorithm was significantly improved through the information of the insertable B-layer used. At the 77% working point, the classifier has a 77% b-jet efficiency while for one misidentified charm-quark, 6 have been rejected [53].

Missing tranverse energy

The missing transverse energy is reconstructed using fully calibrated electrons, muons, photons and jets. The E_T^{miss} is based on the following equation [54]:

$$E_{x(y)}^{\text{miss}} = - \sum_{i \in \{\text{hard objects}\}} p_{x(y),i} - \sum_{j \in \{\text{soft signal}\}} p_{x(y),j} \quad (4.3)$$

Where the hard objects include the mentioned particles. The soft signal is referring to tracks not associated to any hard objects mentioned before. A detailed explanation of the missing transverse energy reconstruction and its performance in 2015 data can be found in [54].

Overlap removal

Baseline objects can have some ambiguities, therefore an overlap procedure is performed with the baseline objects to remove those ambiguities:

1. Jets within a distance $\Delta R = \sqrt{(\Delta y)^2 + (\Delta \phi)^2} = 0.2$ of a baseline electron are discarded, to avoid considering calorimeter deposits from the electron shower as jets
2. If the jet is b-tagged the lepton will be discarded, since it's considered to come from a leptonic b-meson decay
3. Electrons within a distance of $\Delta R = 0.4$ to a jet will be discarded to remove electrons from leptonic charm- or bottom-quark-hadrons
4. Muons within a distance of $\Delta R = 0.4$ to a jet will be discarded to remove muons from leptonic charm- or bottom-quark-hadrons

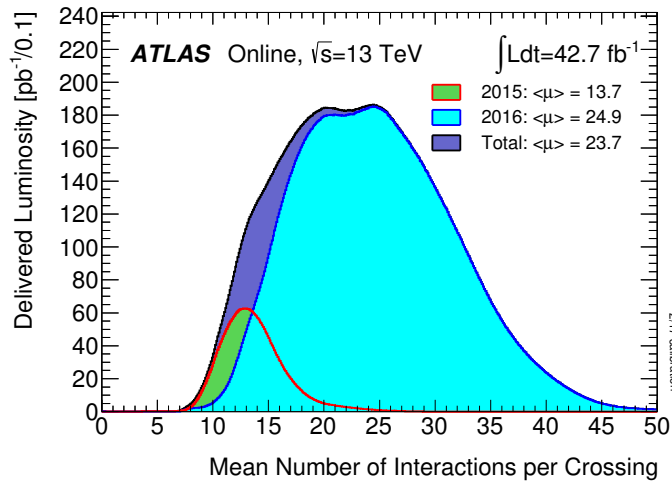


Figure 4.2: Average collisions per bunch crossing in 2015 and 2016 data [55]

5. A muon with deposits in the calorimeters having the same ID track as an electron is removed
6. Electrons sharing an ID track with muons are removed

Pileup-reweighting

As pile-up within ATLAS, simultaneous proton-proton collisions parallel to the considered hard-collision event are an additional source of background. This is accounted for in the Monte Carlo simulations. Since the amount of pile-up events is largely dependent on the exact bunch and luminosity conditions, the simulation is not always produced with the same pile-up properties. Therefore a reweighting is performed, to synchronise the simulated pile-up conditions with the ones in data. The pile-up conditions in 2015 and 2016 can be seen in figure 4.2, where the averaged proton-proton collisions per bunch crossing are shown.

Analysis preselection

With the physics objects defined as described, the analysis applies a selection of at least two same-sign signal leptons. Apart from that requirement, a ‘truth-matching’ is applied to Monte Carlo simulations, using the `McTruthClassifier` [56]. This is using MC generator information to remove non-prompt leptons in the MC simulation, which are estimated using data-driven methods (described in section 7.1) in this analysis.

5 The WH two same-sign leptons analysis

This work was part of an analysis searching for the benchmark model described in section 2.2.4. The chargino and neutralino production decaying via a W and Higgs boson can result in several final states, depending on the Higgs and W decay. In total, five analyses look for final states including one lepton and two b-jets, one lepton and two photons, three leptons, and a fully hadronic decay to jets [57, 58, 59, 60]. The analysis described here is looking at a final state with two same-sign leptons, which can come from a leptonic W decay (with a W boson branching ratio into leptons of 37.78% [10]) and a semileptonic Higgs decay or an hadronic W decay (with a W boson branching ratio into hadrons of 67,4 % [10]) and a fully leptonic Higgs decay. Semi- or fully leptonic Higgs decays include the decay via two W-bosons, two τ leptons decaying into leptons, two muons or two Z bosons. An overview of the Higgs branching ratios is given in figure 5.1. The dominant decay of a Higgs boson into leptons is given through $H \rightarrow WW$. Apart from the two same-sign leptons, jets and missing transverse energy are part of the considered final state. The jets can originate from e.g a semi-leptonic Higgs decay (e.g. $H \rightarrow WW \rightarrow \ell\nu q\bar{q}'$), whereas the missing transverse energy is due to the $\tilde{\chi}_1^0$ in the signal model, which is stable and neutral.

This final state could not only be caused by the supersymmetric model searched for, but also by Standard Model processes.

After presenting those SM processes, the analysis strategy to reduce those SM backgrounds will be introduced, concluded by the problem of estimating non-prompt leptons in this analysis.

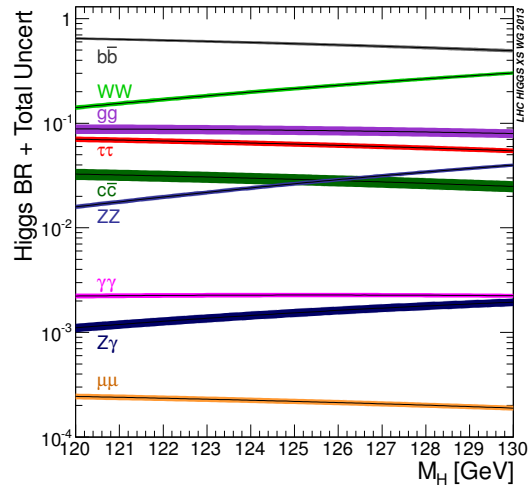


Figure 5.1: Overview of the SM Higgs branching ratios [61]

5.1 Standard Model backgrounds

Many standard model processes result in a final state with oppositely charged leptons, e.g. through Drell-Yan processes, a decay of a (virtual) photon or Z boson. Due to this, this analysis only considers same-sign leptons, to suppress the contribution of those oppositely charged leptons. Exemplary processes for single-top quark production and Drell-Yan processes, both leading to opposite-sign leptons, are shown in figure 5.2. A percentage of this processes can nevertheless contribute to the same-sign final state by a so called ‘charge-flip’, a mis-identification of the leptons charge, caused through interaction with the detector material. More details on the data-driven estimation of this contribution and its origin is given in section 7.2. Before considering dedicated estimation techniques for this background, Monte Carlo simulations are taken for its estimation in the optimisation of the signal regions (chapter 6).

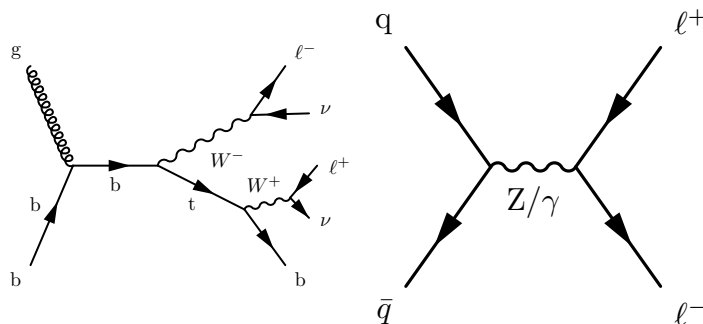


Figure 5.2: Exemplary Feynman diagrams for Wt single-top production and a Drell-Yan process, both later on referred to as charge-flip processes

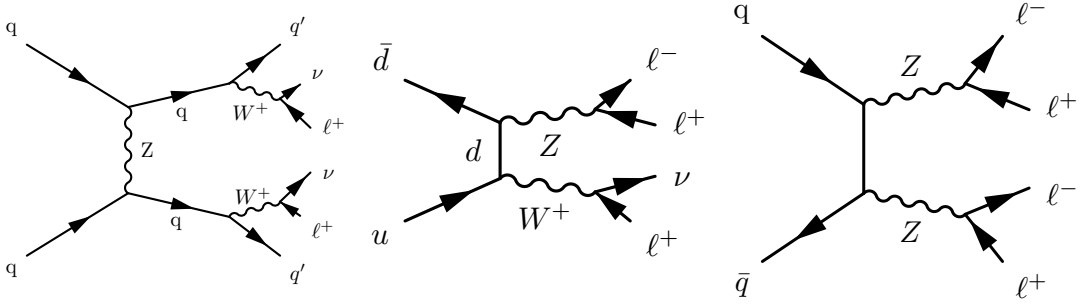


Figure 5.3: Exemplary Feynman diagrams for WW, WZ and ZZ production

The main contribution of genuine SM processes, producing two same-sign leptons, is given through diboson processes. Here WZ production is the dominant reaction, with one lepton not being reconstructed as lepton or not fulfilling the signal lepton requirements defined in section 4.5.

Non-prompt leptons constitute another important source of backgrounds. Non-prompt leptons refer to processes like W/Z plus additional jets in figure 5.4. These are semi-leptonic or even hadronic processes with no lepton in the hard process. A jet gets misidentified as a signal lepton in the detector. More details on the origins of non-prompt leptons are given in section 7.1.

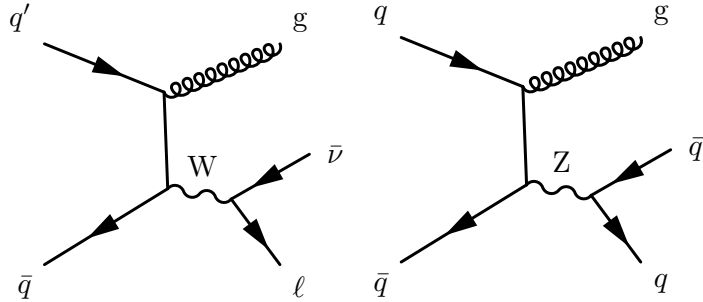


Figure 5.4: Exemplary Feynman diagrams for W/Z + jets production

Lastly, processes like an associated production of a vectorboson and a Higgs boson, top pair production with a Higgs boson, triboson production and multi-top processes can also produce a final state with jets, missing transverse energy and two same-sign leptons. In the following, multi-top processes, top pair production with a Higgs boson, Higgs-associated processes and triboson production are considered as 'Rare' processes.

All Monte Carlo samples used for the different processes, the generators used and the production cross sections can be found in appendix A.1, including an overview on the used categorisation.

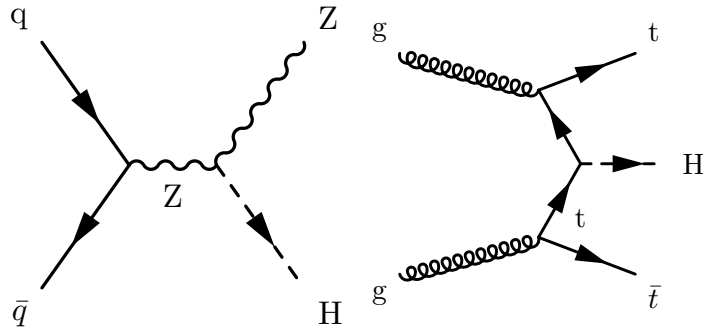


Figure 5.5: Exemplary Feynman diagrams for ZH and ttH production

5.2 Analysis strategy

Being able to distinguish the mentioned SM backgrounds from the chargino neutralino production is crucial to make a statistical statement whether the SUSY process was seen in data or not. The signal model explained in section 2.2.4 has two free parameters, which also influences the kinematics and cross section of the signal process. The varied parameters are $m_{\tilde{\chi}_1^\pm}$, set equal to $m_{\tilde{\chi}_2^0}$, and the LSP mass, $m_{\tilde{\chi}_1^0}$. An overview of the simulated mass points is given in figure 5.6, the Monte Carlo samples used are listed in appendix A.1.

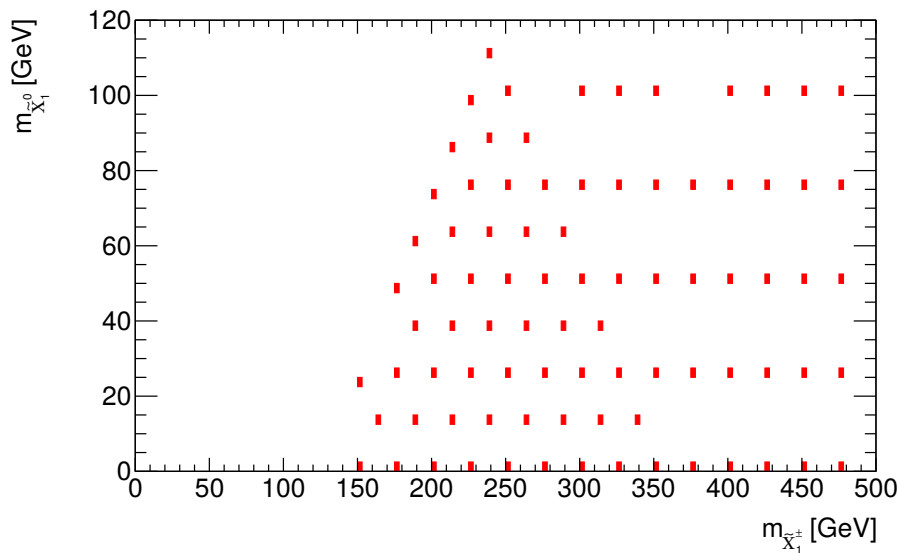


Figure 5.6: Simulated grid of signal samples

A typical ATLAS search for new physics designs three kinds of kinematic regions: Control regions, Validation regions and Signal regions.

Control regions (CR) are regions in the parameter space with a very low and ideally zero signal contamination. They are used to estimate the background processes by comparing the Monte Carlo simulation to data. Multiple control regions for multiple processes can be used. The regions should have a high purity in the considered background process. Normalisation factors are defined, to scale the MC to agree with the data in this regions. The normalisation of this process is then extrapolated to signal or validation regions.

In **validation regions** (VR), this extrapolation is validated by comparing the prediction, including the derived normalisation parameters, to data. Also in these regions, the signal contamination should be small, even though validation regions are chosen to be close to the signal regions, to guarantee a good background estimation through a small extrapolation.

Signal regions (SR) are regions where the comparison of data to the SM backgrounds and the signal hypothesis is done and hypothesis tests are carried out. The aim of these regions is to have a high amount of signal events versus low expected background yields.

In this analysis, no normalisation factors and therefore no control regions will be defined. Instead, the main backgrounds will be either taken directly from data or additionally validated in Monte Carlo through validation region. An attempt was made to design diboson control regions, but first attempts showed the necessity of further sophisticated studies for their definition.

5.3 The problem of fakes

Non-prompt leptons as well as charge-flip leptons present a challenging SM background, as arising mainly from mis-measurements in the detector. Since non-prompt leptons and charge-flip leptons are based on mis-measurements in the detector, interaction with the detector material or secondary particle decays, it cannot be fully simulated with Monte Carlo, or the exact rate of such interactions cannot be predicted by MC simulations. In case of the charge-flip background, the agreement between a data-driven estimate and the MC simulation is fairly good, whereas for the fake leptons, MC is underestimating the rate of non-prompt leptons. This can be seen in figure 5.7. A direct comparison of the Monte Carlo simulation of non-prompt leptons and the data-driven estimation is shown, further explained in section 7.1. The overall kinematic distributions have a similar behaviour, but a scaling difference of around two is observed. This was also observed by other analysis, e.g [62]. Therefore the signal region optimisation was done using the data driven fake estimation, whereas all other backgrounds have been taken from Monte Carlo simulation.

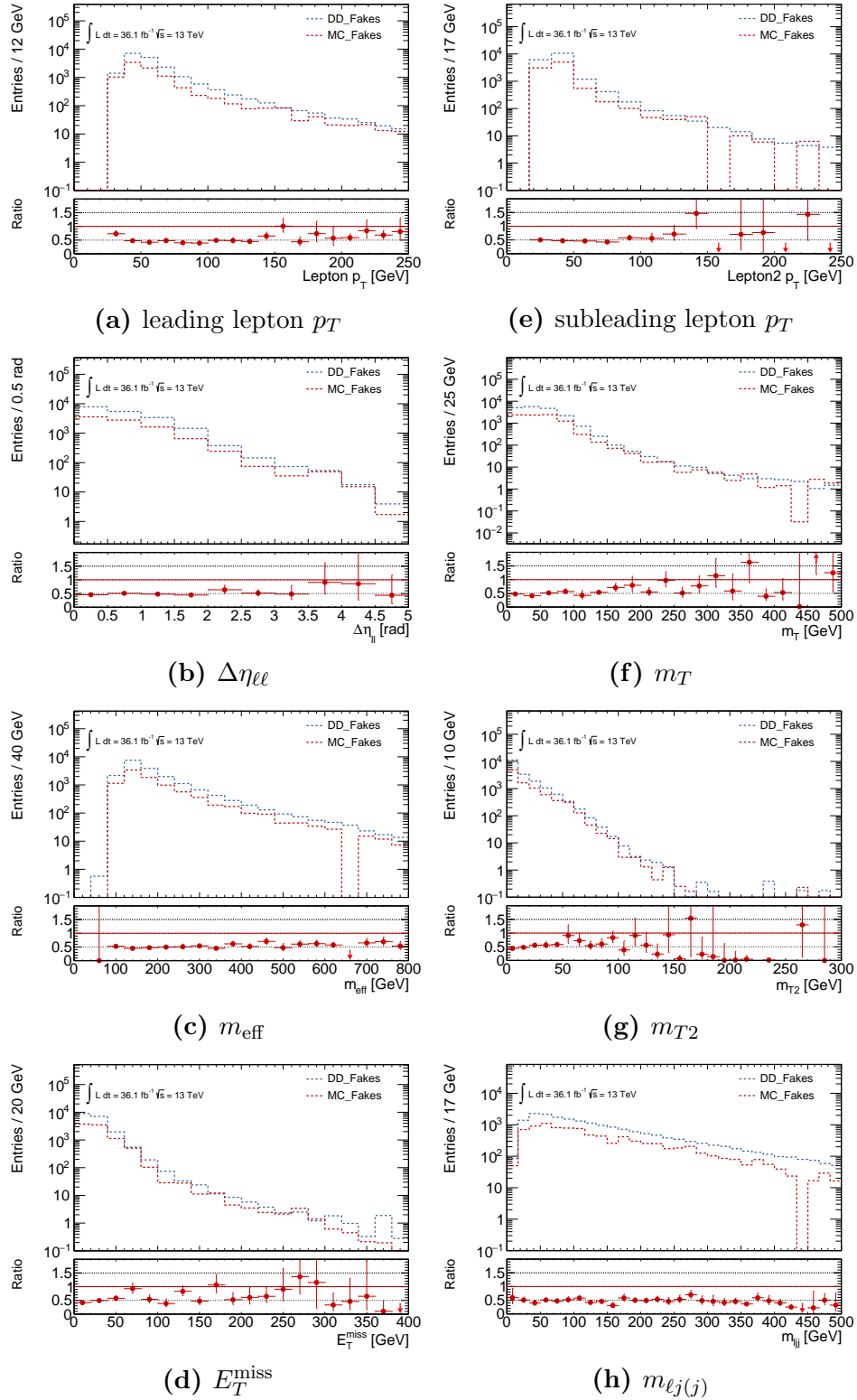


Figure 5.7: Comparison of data-driven (DD) fake estimation and fakes predicted by MC simulation. Events with one, two or three jets are considered and a veto on b-jets is applied.

6 Optimisation of the signal regions

6.1 Discriminating variables

This section summarises the kinematic variables used in this work and highlights the separation between SM backgrounds, explained in section 5, and the benchmark SUSY model considered.

Number of leptons, jets and b-tagged jets

In figure 6.1 the distributions of baseline and signal leptons are shown, each background normalised to its overall yields in the depicted kinematic range. A preselection of at least two signal and baseline leptons, two of them of same-sign is applied. Already at this preselection level it can be seen that roughly 10 percent of the signal events end up in a final state with three leptons. Since this analysis is designed to be combined with an analysis considering three leptons in the final state [59], a veto on the third lepton is placed, although this reduces the signal efficiency. The charge-flip and non-prompt lepton estimation has an exactly two baseline and signal lepton requirement applied. For the data driven background estimates of charge-flip and non-prompt leptons, over fifty percent of each background has no jet in the event. Whereas for the signal process there is only around ten percent of the events without jets. This is due to a possible partial hadronic Higgs decay in the simplified model (e.g in $H \rightarrow WW \rightarrow q\bar{q}t\ell\nu$) as well as the W boson decaying into hadrons in the case of a fully-leptonic Higgs decay. Many background processes including a top quark in the decay chain can be largely suppressed by applying a b-jet veto (figure 6.1d), since the dominant top quark decay is via $t \rightarrow Wb$. while the benchmark model considered only has under ten percent of the events including a b-tagged jet.

Lepton momenta and pseudorapidity difference - p_T , $\Delta\eta_{\ell\ell}$

The transverse momenta of both leptons are shown in figures 6.2a and 6.2b for the backgrounds and one exemplary signal process. The distributions are normalised to the overall yields of the respective process. Leptons originating from a chargino neutralino pair production have higher momentum, since the mass of the mother particles is heavier than for the SM background processes. The lepton p_T distribution of charge-flipped particles peaks around 40-50 GeV for the leading and the subleading lepton,

reconstructing the Z-boson mass of 91 GeV [10]. The pseudorapidity difference (figure 6.2c) between both leptons shows similar behaviour for SM processes and the benchmark model considered.

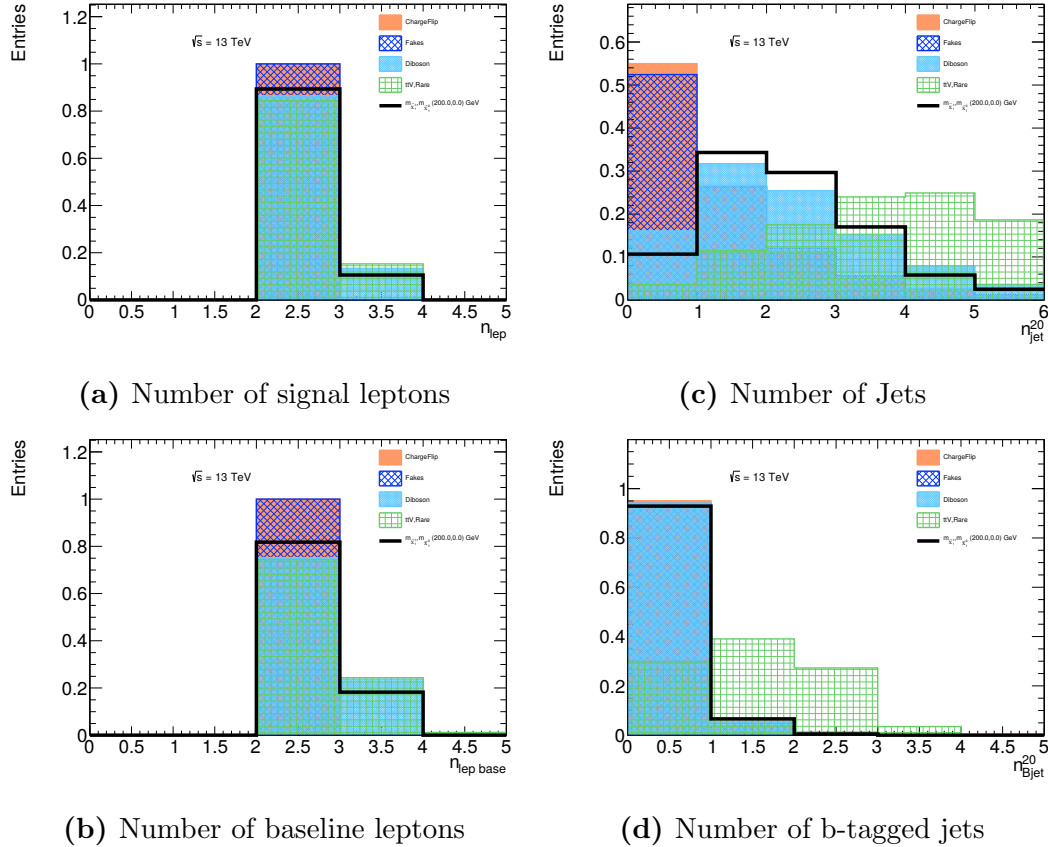


Figure 6.1: Normalised kinematic distributions with at least 2 same-sign leptons for all background processes and one signal mass point (in black). The processes are normalised to their respective yield in the shown kinematic range.

Missing transverse energy - E_T^{miss}

The missing transverse momentum and its absolute value, the missing transverse energy (as described in section 4.5) is caused by neutrinos in standard model backgrounds. Charge-flip processes as well as non-prompt leptons are mainly located at low E_T^{miss} , since no or low $-p_T$ neutrinos are produced. For SUSY processes, the neutralino escapes the detector without signal. Therefore the SUSY process has a high amount of missing transverse energy.

Effective mass - m_{eff}

The effective mass is the sum of the transverse momenta of leptons (6.1), jets and the missing transverse energy. It aims to reconstruct the initially produced particles via summing their decay products.

$$m_{\text{eff}} = \sum_{\text{leptons}} p_T + \sum_{\text{jets}} p_T + E_T^{\text{miss}} \quad (6.1)$$

Consequently, SUSY particles, being heavier than SM particles, show a higher effective mass than SM processes (see figure 6.3a). Additionally, the effective mass has a sensitivity to the mass difference between $\tilde{\chi}_1^\pm$ and $\tilde{\chi}_1^0$ [63].

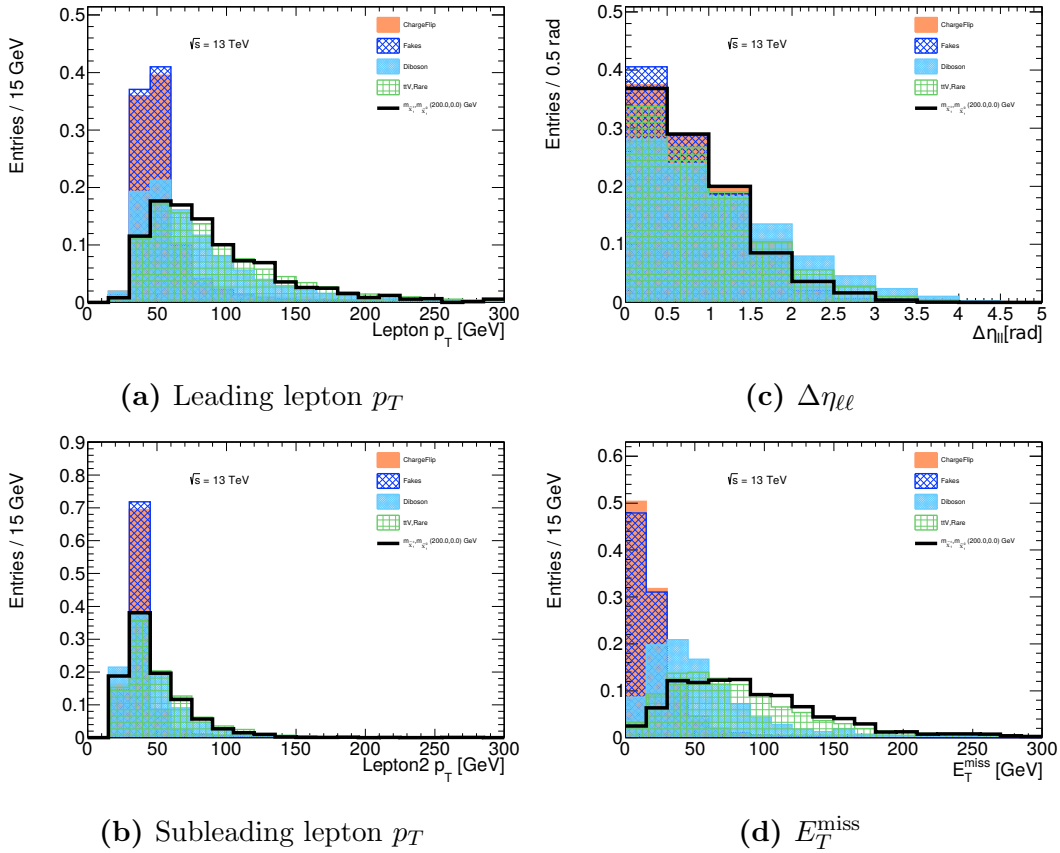


Figure 6.2: Normalised kinematic distributions with at least 2 same-sign leptons for all background processes and one signal mass point (in black). The processes are normalised to their respective yield in the shown kinematic range.

Transverse mass - m_T

m_T (figure 6.3d) is defined via equation (6.2) (neglecting the lepton rest mass).

$$m_T = \sqrt{2p_T^\ell E_T^{\text{miss}}(1 - \cos(\Delta\phi(\ell, \mathbf{p}_T^{\text{miss}}))} \quad (6.2)$$

It builds the mass from the four-vectors of the highest p_T lepton and the missing transverse momentum. Originally it was constructed to constrain the W boson mass in leptonic W decays with a neutrino causing the missing transverse momentum. In dileptonic final states, it is still useful to suppress Standard Model backgrounds with a W-boson as well as low- p_T and low E_T^{miss} processes. For the chargino neutralino production it reaches higher values compared to the SM processes due to the higher E_T^{miss} and higher lepton p_T .

Stransverse mass - m_{T2}

The stransverse mass is a generalization of the transverse mass, considering two decay arms with an invisible particle. Following the definition by Barr, Lester and Stephens [64]:

$$m_{T2}^2(\mathbf{p}_T^{\ell_1}, \mathbf{p}_T^{\ell_2}, \mathbf{p}_T^{\text{miss}}; \chi) \equiv \min_{\mathbf{p}_1^{\text{miss}} + \mathbf{p}_2^{\text{miss}} = \mathbf{p}_T^{\text{miss}}} \left[\max\{m_T^2(\mathbf{p}_T^{\ell_1}, \mathbf{p}_T^{\text{miss}}, \chi), m_T^2(\mathbf{p}_T^{\ell_2}, \mathbf{p}_T^{\text{miss}}, \chi)\} \right] \quad (6.3)$$

This definition has the nice feature for pair produced SUSY particles that it is bound from above by the mass of the pair produced particle. The normalised distributions of m_{T2} in events with at least two same-sign leptons for signal and background is shown in figure 6.3b. SM processes with its lower m_T also cluster at low m_{T2} values.

Invariant mass of jets and lepton - $m_{\ell j(j)}$

The invariant mass of jets and leptons is calculated by using the highest p_T jet or a dijet system of leading and subleading jet if the jet multiplicity is larger or equal to one. Using the closest lepton (taking ΔR as distance measure), the invariant mass is calculated. The $m_{\ell j(j)}$ variable aims to reconstruct the semileptonic Higgs decay in the chargino neutralino simplified model, thus in figure 6.3c the signal distribution peaks below 125 GeV. The missing momentum in the Higgs reconstruction is due to the missing neutrino or second lepton in the invariant mass. Standard Model processes can reach higher $m_{\ell j(j)}$ through leptons and jets from different initial particles. The first bin in figure 6.3c is due to zero-jet events.

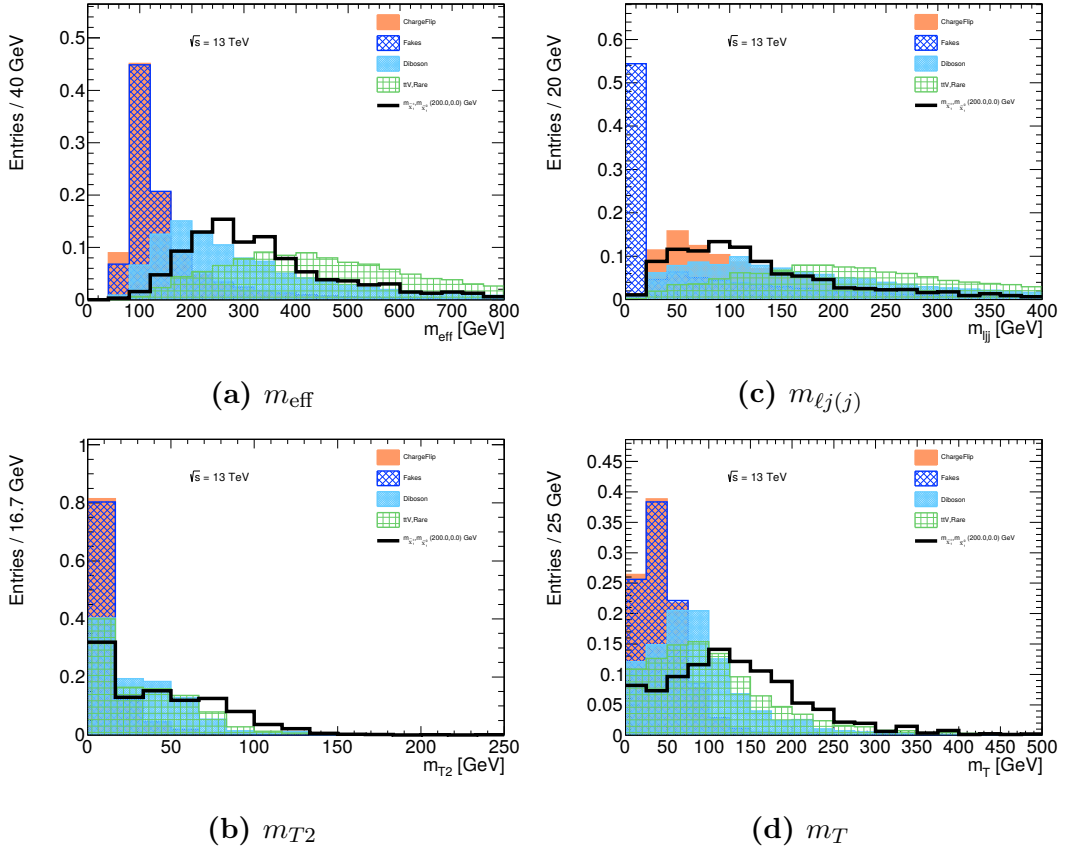


Figure 6.3: Normalised kinematic distributions with at least 2 same-sign leptons for all background processes and one signal mass point (in black). The processes are normalised to their respective yield in the plotted kinematic range.

6.2 Optimisation procedure

The following section describes the procedure to optimise and define signal regions. The discriminating power of the kinematic variables listed in section 6.1 has been studied using their distributions after preselection requirements. Splitting the distributions according to the number of jets in the event is an initial step to define signal regions. This was done in run 1 [22] and is motivated by the different kinematics, allowing to set higher/lower requirements on different variables, dependent on their jet-multiplicity. Both regions will be statistically combined, since they are orthogonal due to their jet multiplicity. Figure 6.4 and Figure 6.5 show the kinematic variables after the preselection criteria as given in table 6.1, requiring exactly one jet or two or three jets. In contrast to the normalised kinematic distributions above, all the following plots do not include the data-driven charge flip estimation, but Monte Carlo simulation for charge-flipped leptons, as used throughout the optimisation procedure, since at the

optimisation stage in the analysis, no data-driven estimation of charge-flipped leptons was available and the deviations from the Monte Carlo estimation were considered to be small.

preselection cut	SRjet1	SRjet23
number of jets	1	2 or 3
baseline leptons	2	2
signal leptons	2	2
charge of leptons	same-sign	same-sign

Table 6.1: Preselection requirements, applied in the optimisation procedure

b-Jets
$\Delta\eta_l$
E_T^{miss}
m_T
m_{eff}
$E_T^{\text{miss}}/m_{\text{eff}}$
$m_{l_j(j)}$
m_{T2}

Table 6.2: Variables considered in the optimisation

Based on the distributions after preselections, the variables listed in table 6.2 were used in the optimisation.

The optimisation was performed with a multidimensional scanning tool, ARRGH, developed by Nikolai Hartmann [65]. Each variable is varied within predefined values. The resulting combinations of kinematic requirements are sorted into one hundred signal efficiency bins. For each bin the tool selects the region definition with the best background suppression, assuming that this leads to a higher significance.

The discovery significance is calculated including statistical uncertainties and a 25 % flat systematic uncertainty to account for the experimental and theoretical uncertainties. The choice of configuration for this tool was iterative, mainly considering the variable interval. Only a small selection of configurations and results, which led to the final signal region choice for the analysis, is presented.

Based on the distributions under preselection (figure 6.4, 6.5), the setup given in table

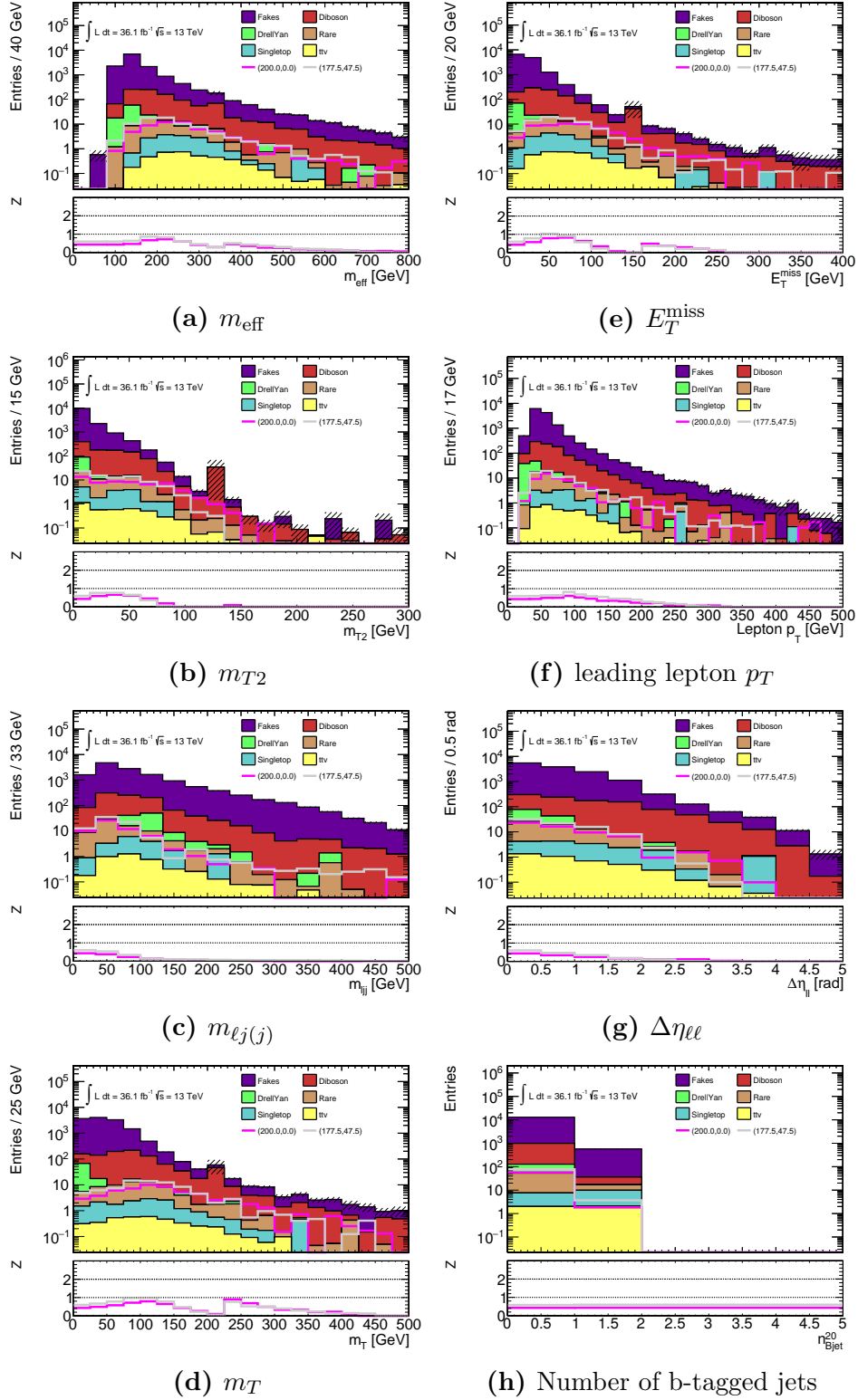


Figure 6.4: Distributions for a one jet preselection. Shown in the lower panel is the discovery significance, calculated including the statistical uncertainty only. For all but the b-jet distribution, the significance calculation refers to lower bounds.

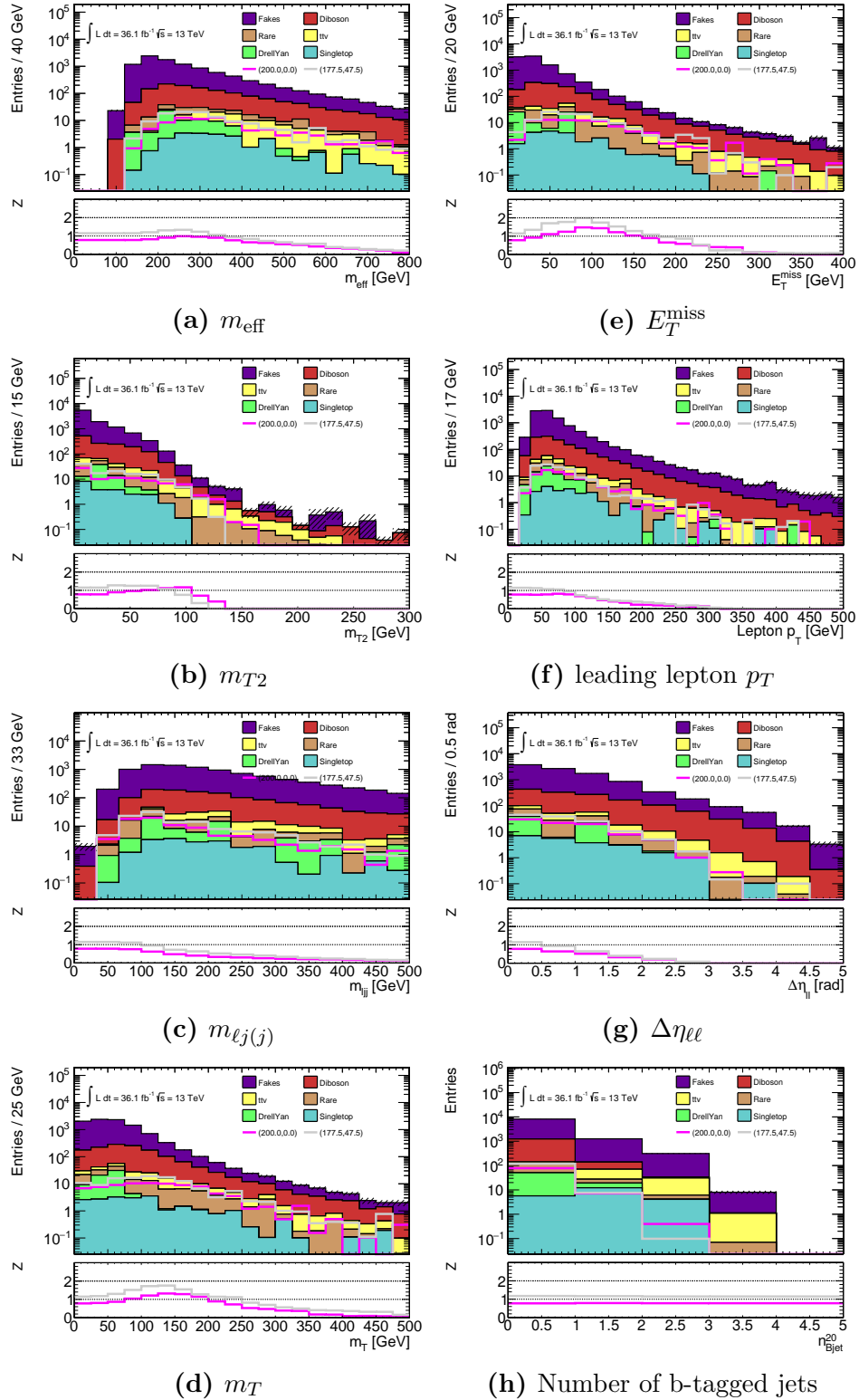


Figure 6.5: Distributions for a two or three jet preselection. Shown in the lower panel is the discovery significance, calculated including the statistical uncertainty only. For all but the b-jet distribution, the significance calculation refers to lower bounds.

	one jet	two or three jets
signal point	$m_{\tilde{\chi}_1^\pm} = 225.0 \text{ GeV}$ $m_{\tilde{\chi}_1^0} = 75.0 \text{ GeV}$	$m_{\tilde{\chi}_1^\pm} = 187.5 \text{ GeV}$ $m_{\tilde{\chi}_1^0} = 37.5 \text{ GeV}$
N_{bjets}	$< [1, 2]$	$= 0$
$\Delta\eta_{\ell\ell}$	$\leq [3., 1.5]$	-
E_T^{miss}	$> [0., 20, 40, 60, 80, 90., 100, 110, 120.]$	$> [0, 30, 60, 90, 120, 150]$
m_{eff}	$> [0., 120, 140, \dots, 240, 270, 290, 300]$	$> [0., 90., 120., \dots, 240, 270, 300, 400]$
$E_T^{\text{miss}}/m_{\text{eff}}$	$> [0., 0.1, 0.2, 0.3, 0.4, 0.5, 0.6]$	-
$m_{\ell_j(j)}$	$\leq [50, 70, 80, 100, 110, 130, 150, 180, 200, 300]$	$\leq [50., 80., 100, 110, 120, 140, 150, 180, 200, 300]$
m_T	$> [0., 30., 60., 90., 120., 150., 180]$	$> [0., 30., 60., 90., 100, 120., 150., 180]$
m_{T2}	$> [0, 10, 20, 30, 40, 50, 60, 70, 80, 90, 100]$	$> [0, 10, 20, 30, 40, 50, 60, 70]$

Table 6.3: Configuration of the multivariate scanning tool

6.3 was chosen. For the different jet multiplicities, two distinct signal mass points were chosen, to involve a spectrum of signal kinematics in the optimisation.

Within the optimisation, different background constraining criteria can be tested. In figure 6.6 and 6.7 the optimisation results for the one jet and two or three jets configuration is shown. Depicted is the discovery significance as described above versus the signal efficiency and total background yields for the criteria listed in table 6.4, each point refers to one possible signal region. To not allow for kinematic regimes with low Monte Carlo statistics in the main backgrounds, at least ten unweighted Monte Carlo events for diboson processes and top quark pair production with an associated vector boson were required. This is limiting the statistical uncertainties from diboson and $t\bar{t} + V$ processes.

criteria	explanation
nom	overall background yields need to be larger than 0
bulk_dt	at least 10 unweighted $t\bar{t}V$ and diboson events
alg0	weighted diboson, $t\bar{t}V$ and non-prompt lepton background yields ≥ 0
30p	statistical uncertainty needs to be less than 30 %
5bg	at least 5 weighted background events
2bg	at least 2 weighted background events

Table 6.4: Definition of all background criteria

In general, the analysis only reaches low signal efficiencies, since requiring both leptons to have same sign removes around 50% of the signal events. Within the one hundred possible signal regions for each jet multiplicity bin, the highest significance was chosen for the jet two or three optimisation, whereas for the single jet region the second highest significance combination was chosen to recover more background statistics. The kinematic requirements for those two regions are defined in table 6.5, the N-1 plots are shown in figure 6.8 and 6.9.

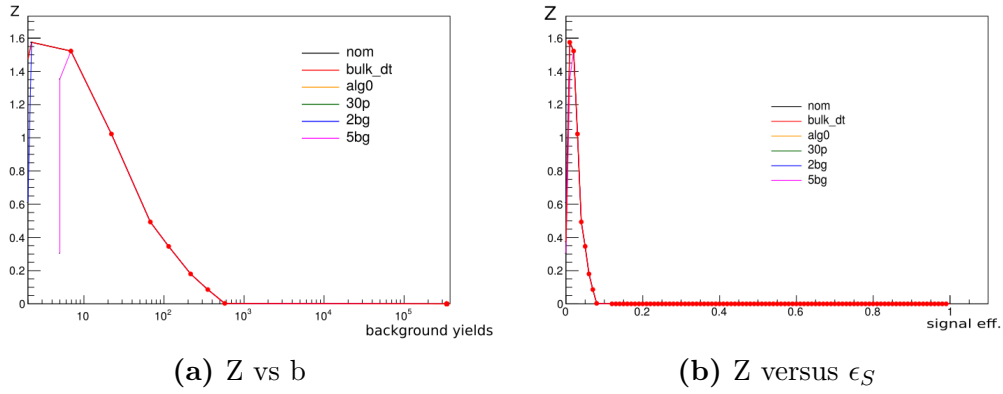


Figure 6.6: Significance in Gaussian standard deviations versus background yields and signal efficiency respectively, for the one jet optimisation.

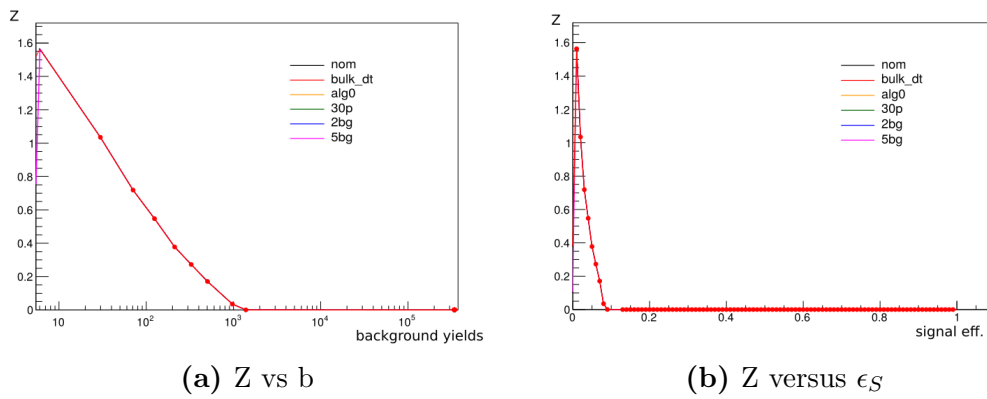


Figure 6.7: Significance in Gaussian standard deviations versus background yields and signal efficiency respectively, for the two or three jet optimisation.

variable	jet1	jet23
BJets	< 1	–
p_T^{l1}	≥ 25	≥ 25
p_T^{l2}	≥ 25	≥ 25
$\Delta\eta_{ll}$	≤ 1.5	–
E_T^{miss}	> 100	> 100
m_T	> 140	> 120
m_{eff}	> 220	> 240
$E_T^{\text{miss}}/m_{\text{eff}}$	> 0.3	–
$m_{lj(j)}$	≤ 180	≤ 140
m_{T2}	> 80	> 70
Significance	1.522	1.56

Table 6.5: Optimisation results with the highest (second highest) significances

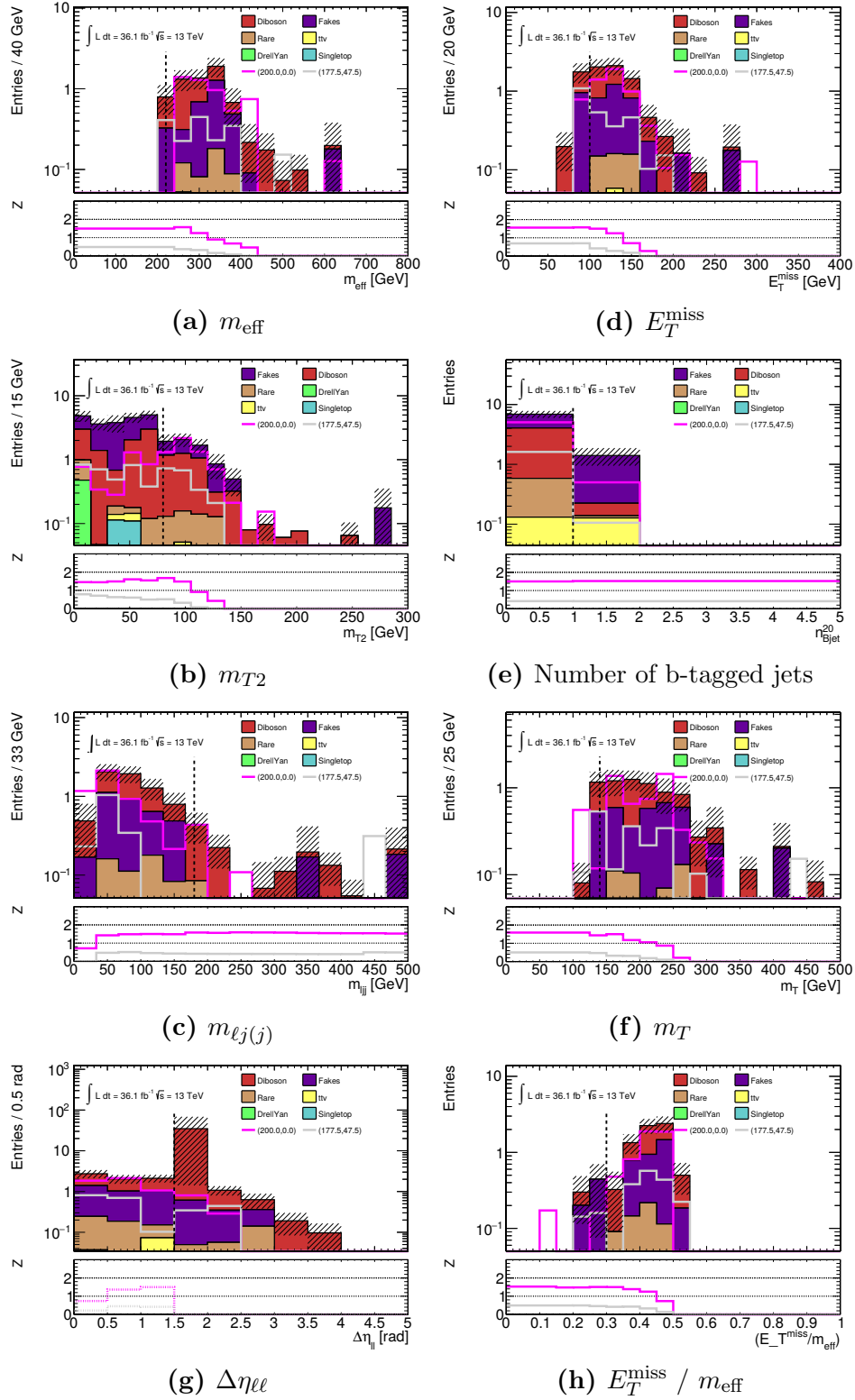


Figure 6.8: Optimisation result chosen for the one jet multiplicity. Shown in the lower panel is the discovery significance, calculated including the statistical uncertainty only.

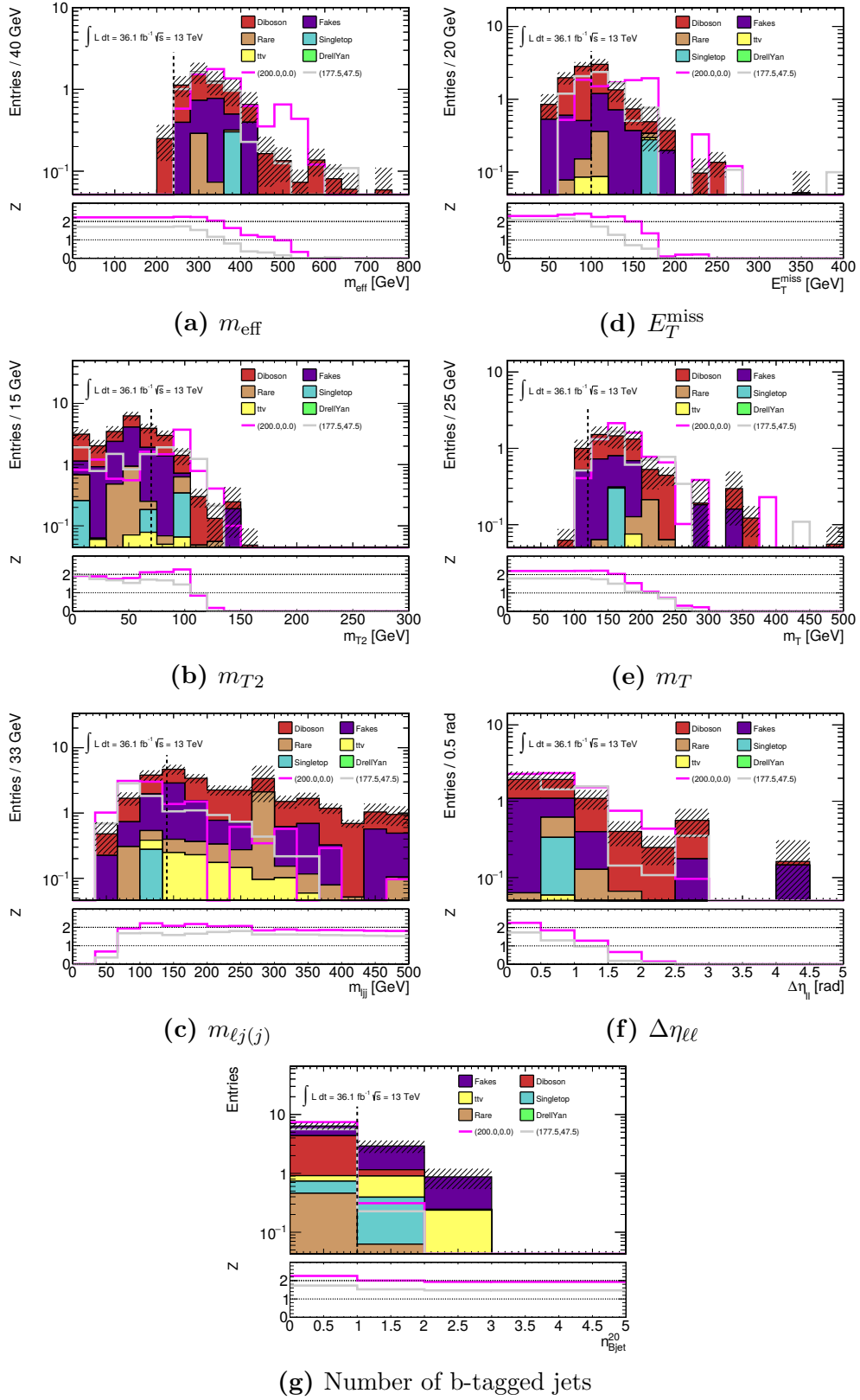


Figure 6.9: Optimisation result chosen for the two or three jets region. Shown in the lower panel is the discovery significance, calculated including the statistical uncertainty only.

6.3 Signal region definitions

Based on the N-1 variable distributions for both optimisation results, the cuts were further tuned, also taking other signal mass points in the distributions into account. Even though the m_{eff} and m_T cut have a small contribution to the overall significance (which can be seen in the lower pad showing the significance without the m_{eff} and m_T cuts in figure 6.8 and 6.9), this was further checked and found to contribute to the exclusion of some points, and therefore kept in the signal region definition. (See appendix A.2) The final signal region definition in the analysis is shown in table 6.6. The corresponding N-1 plots are shown in figure 6.10 and 6.11 for the different jet-multiplicity bins, showing that the strongest signal to background discrimination is given through m_{T2} and $m_{\ell j(j)}$.

	SRjet1	SRjet23
$N_{\text{b-Jets}}$	0	0
$\Delta\eta_{ll}$ [rad]	≤ 1.5	–
E_T^{miss} [GeV]	≥ 100	≥ 100
m_T [GeV]	≥ 140	≥ 120
m_{eff} [GeV]	≥ 260	≥ 240
$m_{\ell j(j)}$ [GeV]	< 180	< 130
m_{T2} [GeV]	≥ 80	≥ 70

Table 6.6: Final signal region definitions

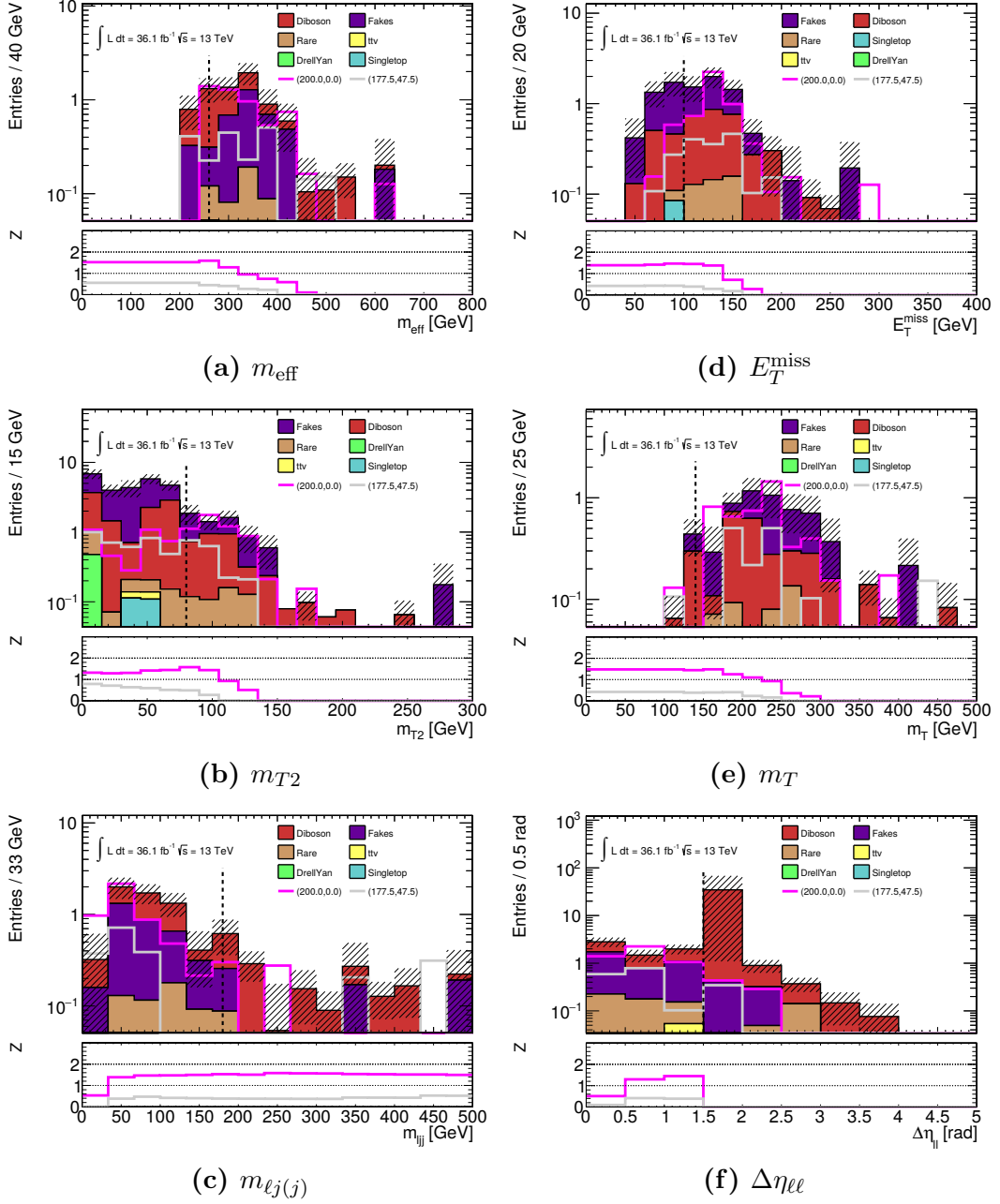


Figure 6.10: N-1 distributions for SRjet1. Shown in the lower panel is the discovery significance, calculated including the statistical uncertainty only.

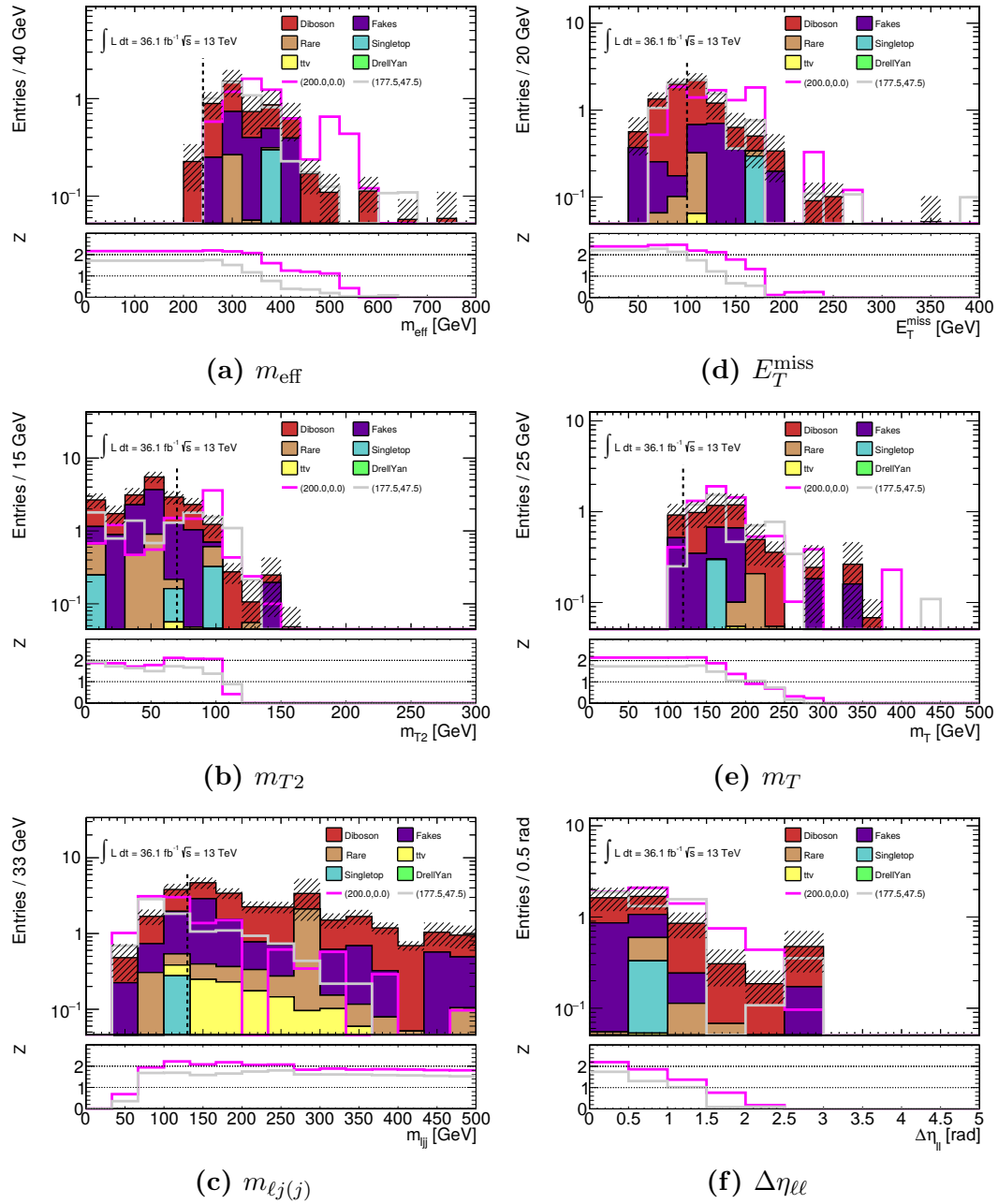


Figure 6.11: N-1 distributions for SRjet23. Shown in the lower panel is the discovery significance, calculated including the statistical uncertainty only.

6.3.1 Expected Significance

The expected significance, shown through the one-sided Gaussian standard deviations of the exclusion CLs value (further discussion of statistical interpretation of results is given in section 9) is shown in figure 6.12. The optimised signal regions are sensitive to chargino-neutralino production with low $\tilde{\chi}_1^\pm$ and $\tilde{\chi}_1^0$ masses, as well as towards the diagonal, above which $m_{\tilde{\chi}_1^\pm} - m_{\tilde{\chi}_1^0} \leq 130$ GeV, and consequently the Higgs boson is no longer produced on-shell. In figure 6.13 the signal yields for both signal regions are depicted. The one jet signal region is sensitive to the considered benchmark model for $\tilde{\chi}_1^\pm$ masses around 200 GeV for $\tilde{\chi}_1^0$ masses up to 25 GeV. With SRjet23, the analysis' sensitivity extends to the lowest considered mass point, with $m_{\tilde{\chi}_1^\pm} = 150$ GeV and a massless $\tilde{\chi}_1^0$ and an additional point towards the diagonal. This exclusion power projections are done with a flat 25% systematic uncertainty assumed, without theoretical uncertainties and without the data-driven charge-flip estimation.

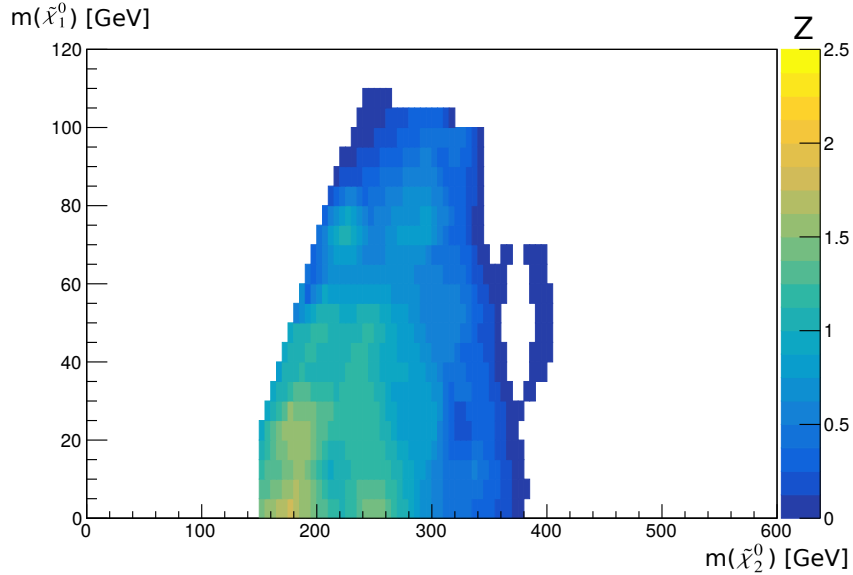
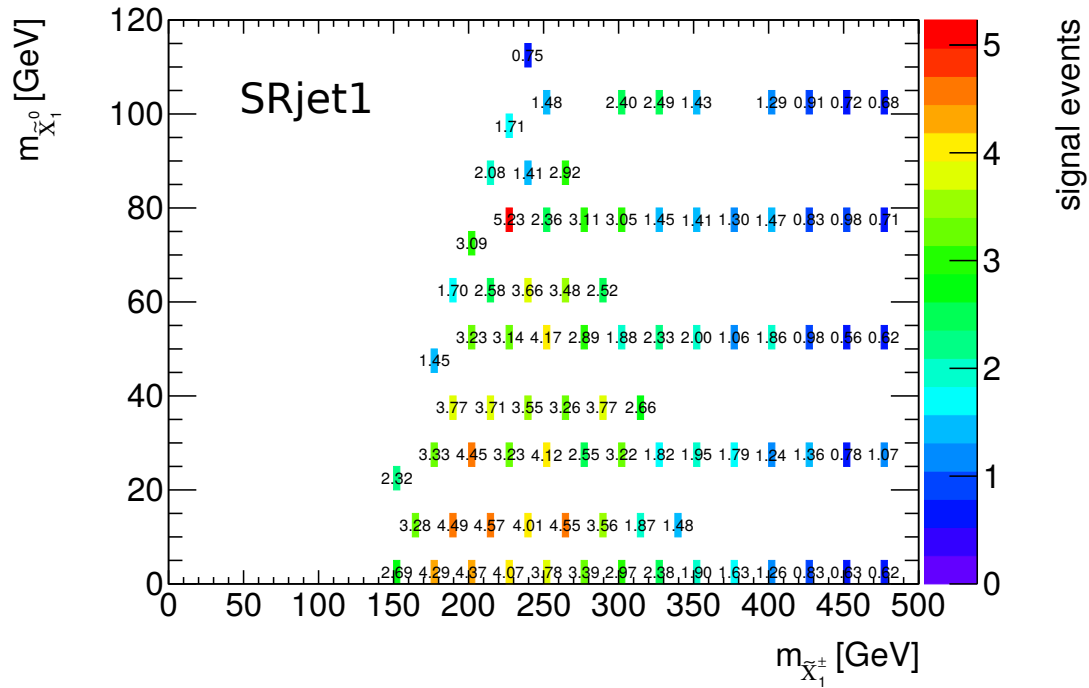
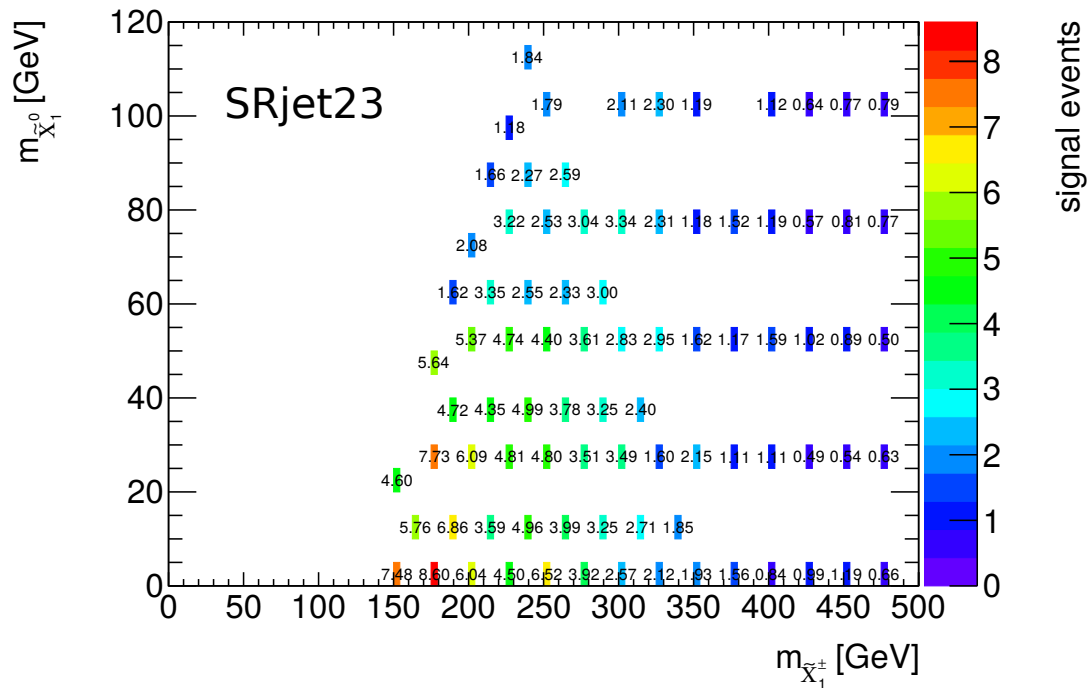


Figure 6.12: Expected CLs value for the statistical combination of SRjet1 and SRjet23. A 25% systematic uncertainty is assumed.



(a) Signal yields in SRjet1



(b) Signal yields in SRjet23

Figure 6.13: Signal yields over the signal mass spectrum in the signal regions

7 Background estimation

In the following chapter, the data-driven background estimations for non-prompt leptons and charge-flipped leptons is summarised. Additionally, the definition of diboson validation regions is described.

7.1 Fake lepton estimation

The estimation of the non-prompt ‘fake’ lepton background is described in the following section since it presents the main background contribution in this analysis. The work presented was done by Peter Tornambe and Martina Javurkova and is fully described in [19]. Mathematical details of the generalised matrix method can be found in [66].

7.1.1 The generalised Matrix Method

Non-prompt leptons can originate within ATLAS through mainly three different categories:

- **photon conversion** e.g. Bremsstrahlung photons from muons causing the muon ID track to be identified as electron track
- **light meson decay** e.g. jets from a light meson leaves a ID track and photons in the decay of the meson cause the calorimeter signature
- **heavy meson decay** e.g. b-mesons decaying semi-leptonically

Fake leptons tend to have poorer isolation properties compared to prompt leptons, which can be used for estimating their contribution in the analysis regions. The basic idea of the matrix-method is the definition of a loose (L) and tight (T) lepton requirement, where real leptons are dominantly tight and fake leptons are dominantly loose. Within this analysis, loose leptons are baseline leptons passing the overlap removal procedure, tight leptons are defined to be signal leptons. With this classification, one can estimate the expected number of real (\hat{n}_R) and fake (\hat{n}_F) leptons in a region by connecting them to the number of tight and loose leptons (n_T, n_L) via efficiencies. Here ϵ_r is the propability of a real lepton being identified as a tight lepton, ϵ_f is the respective probability for a fake lepton, with $\bar{\epsilon}_{f/r} = 1 - \epsilon_{f/r}$ being the inverse probability.

$$\begin{pmatrix} \hat{n}_R \\ \hat{n}_F \end{pmatrix} = \frac{1}{\epsilon_r - \epsilon_f} \begin{pmatrix} \bar{\epsilon}_f & -\epsilon_f \\ -\bar{\epsilon}_r & \epsilon_r \end{pmatrix} \begin{pmatrix} n_T \\ n_L \end{pmatrix} \quad (7.1)$$

To receive an estimate of the fake lepton expectation, we are interested in the number of tight and fake leptons, given in (7.2)

$$\hat{n}_{T \cap F} = \frac{\epsilon_f}{\epsilon_r - \epsilon_f} (\epsilon_r (n_T + n_L) - n_T) \quad (7.2)$$

Generalising the procedure above to events with more than one lepton, all possible cases of fake lepton contribution to events with two tight leptons must be considered, as shown in (7.3)

$$\begin{pmatrix} \langle n_{tt} \rangle \\ \langle n_{tl} \rangle \\ \langle n_{lt} \rangle \\ \langle n_{ll} \rangle \end{pmatrix} = \begin{pmatrix} \epsilon_{r1} & \epsilon_{f1} \\ \bar{\epsilon}_{r1} & \bar{\epsilon}_{f1} \end{pmatrix} \otimes \begin{pmatrix} \epsilon_{r2} & \epsilon_{f2} \\ \bar{\epsilon}_{r2} & \bar{\epsilon}_{f2} \end{pmatrix} \begin{pmatrix} n_{rr} \\ n_{rf} \\ n_{fr} \\ n_{ff} \end{pmatrix} \quad (7.3)$$

To predict the expectation of non-prompt leptons, the real and fake efficiencies need to be determined. This is described briefly in the following two sections.

7.1.2 Measurement of the real lepton efficiency

The efficiency of a real lepton to pass from the baseline into the signal criteria, the ‘real lepton efficiency’, was determined with a Z tag-and-probe method in data. A tag lepton has to pass the signal lepton requirements, the probe lepton is a baseline lepton passing the overlap procedure, has the same flavor as the tag lepton and has to be in an invariant mass window around the Z boson mass. All permutations of tag and probe lepton are considered. The real lepton efficiency is then determined by the ratio of probe leptons passing the signal criteria and the probe leptons passing only the baseline criteria. Determining the efficiency in terms of p_T and η for electrons and muons guarantees that the efficiencies for the first and second lepton can be mutually independent.

7.1.3 Measurement of the fake lepton efficiency

The efficiency of a non-prompt lepton to pass from baseline into the signal criteria, the ‘fake lepton efficiency’ was measured in dedicated control regions. In these regions,

exactly two same-sign leptons have to be present, one of them satisfying the signal criteria and a requirement of $p_T > 40$ GeV. This ‘tag’ lepton is also required to have fired a lepton trigger. On top, a b-tagged jet is required in the control region, to enhance top processes, leading to heavy-flavour originated fakes.

7.2 Charge Flip estimation

Charge-flip processes within this analysis refer to SM processes with two oppositely charged leptons in the hard process, where one of the charges gets mis-identified. This is mostly caused by a Bremsstrahlungs photon, where the photon pair produces a subsequent pair of leptons, where one has a high enough p_T to pass the signal lepton criteria and has the same charge as the original lepton the Bremsstrahlung was originating from. Another, rarer, possibility of a charge-flip in the detector is a mis-measurement of the curvature. The charge reconstruction within ATLAS is based on the curvature measurement in the tracking detector. If the lepton is of high p_T , the curvature is small, therefore the curve fitted through the separate inner detector hits can reconstruct the wrong curvature and therefore a wrong charge. The estimation of the charge-flip background was done by Gabriel Gallardo and is fully described in [19], a brief overview is given in the following.

The charge-flip background is suppressed using the `ElectronChargeIDSelector` [47]. Within this boosted decision tree tool, the information of track and calorimeter information together with the isolation of the leptons is used to distinguish between genuine SM same-sign lepton processes and charge-flip. This tool already reduces the charge-flip background. The remaining component is estimated using a likelihood method in data. It is based on a comparison of SS and OS events in a clean $Z \rightarrow ee$ process and determines the rate in η and p_T bins of the leptons. Charge-flip for muons is negligible in this analysis, due to the lower interaction cross-sections of muons with the detector material (needed for the emission of Bremsstrahlungs photons) and the measurement of the muon momentum and muon curvature in the inner detector as well as in the muon spectrometer. Details on the likelihood method and its validation in Monte Carlo simulation is given in [19].

7.3 Diboson validation regions

Looking at the background contributions in both signal regions shown in figure 7.1, WZ production makes up the largest SM background next to non-prompt leptons.

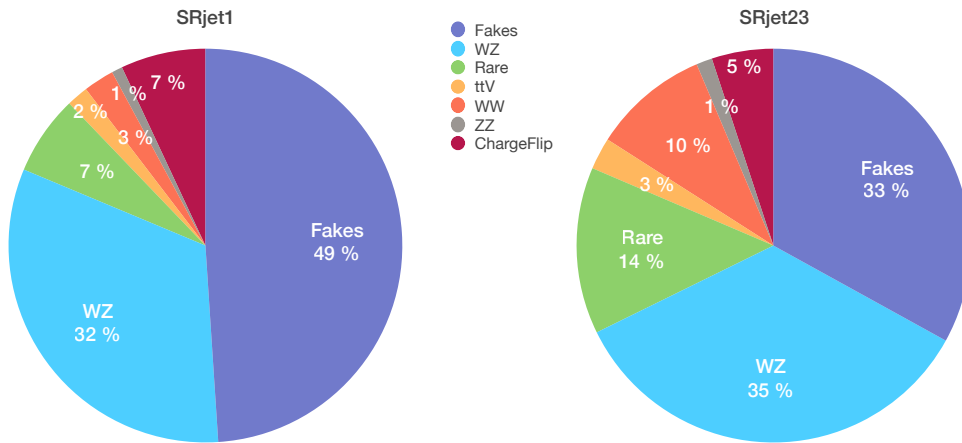


Figure 7.1: Background contributions in SRjet1 and SRjet23 in percentages

Therefore it is important to validate the MC estimation of this process. For this purpose, validation regions have been designed. Validation regions need to be close in kinematic phase space to the signal regions, being able to validate the background estimations in a similar phase space. The validation regions designed for this analysis should not only validate the diboson background, but also serve as a validation of the non-prompt lepton estimation. Therefore they are designed to have a high purity in both processes and assemble the background contribution as in the signal regions as closely as possible. As described in section 6.1, $m_{\ell j(j)}$ is focused to values below the Higgs mass for the simplified chargino neutralino production. Looking at the 2D distributions of $m_{\ell j(j)}$ versus m_{T2} for dileptonic diboson processes, top pair production with an associated vector boson and non-prompt leptons in the SRs (without the respective cut on $m_{\ell j(j)}$ and m_{T2}) in figure 7.2, one can see this behaviour also in the one-jet signal region. For the dileptonic diboson processes, the $m_{\ell j(j)}$ distribution also reaches higher values, over 180 GeV. Therefore, the invariant jet-lepton mass cut was released, to enrich the region in diboson events. To constrain the signal contribution and enrich the fake events, the m_{T2} cut was inverted.

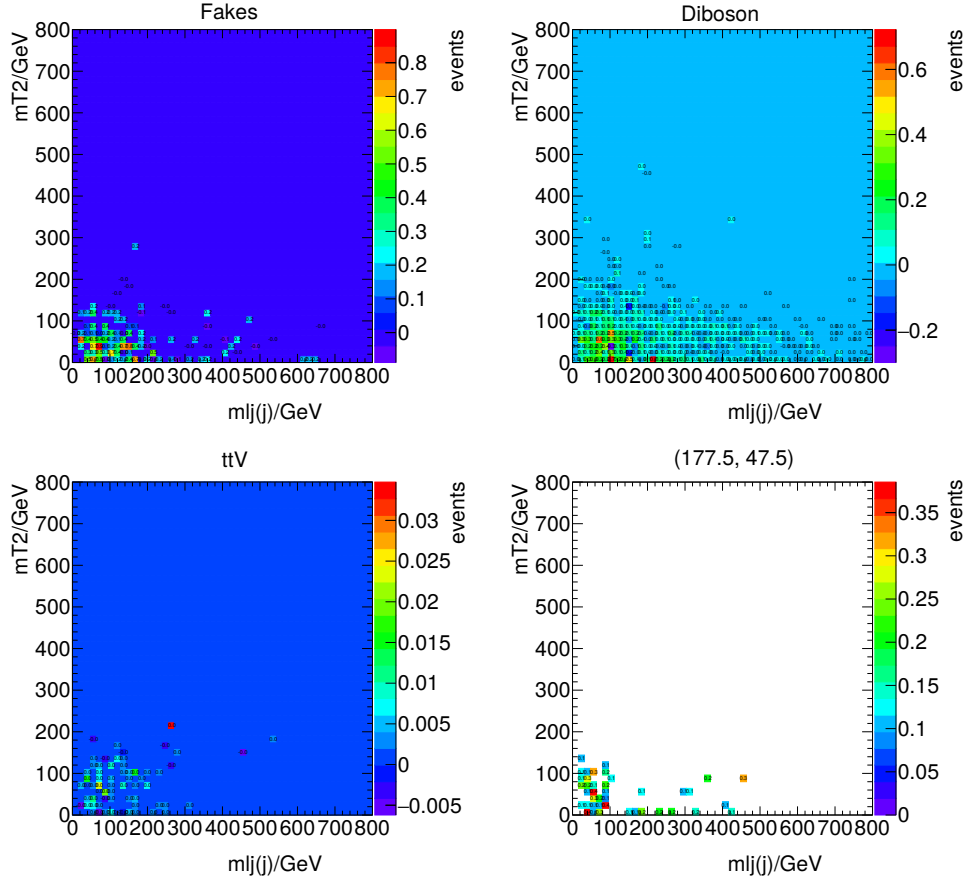


Figure 7.2: m_{T2} versus $m_{\ell j(j)}$ distributions for all SRjet1 cuts applied, except the m_{T2} and $m_{\ell j(j)}$ requirement. The z-axis and the printed numbers show the yields per bin. Shown is the diboson, fake and ttV background and one signal mass point with $m_{\tilde{\chi}_1^\pm} = 177.5$ GeV and $m_{\tilde{\chi}_1^0} = 47.5$ GeV.

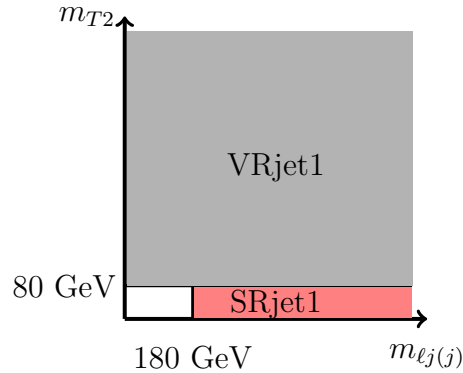


Figure 7.3: Phase space location of VRjet1 in comparison to SRjet1

Comparing the kinematic distributions for the SRjet23, especially the missing transverse energy and $m_{\ell j(j)}$ distribution, shown in figure 7.4 for diboson, fake, ttV and a signal mass point, a clear concentration at low E_T^{miss} values is visible for diboson and fake processes. This is due to only neutrinos (and possible energy mis-measurements) contributing to the missing transverse energy for the background processes. For the two or three jet validation region, a window cut on the E_T^{miss} was chosen, since a good suppression of the fake lepton contribution could be reached through variation of the interval. The $m_{\ell j(j)}$ cut was reversed to reach a low signal contamination. The definition of the validation regions, derived using the 2D distributions, is shown in table 7.1. A schematic explanation of these cuts in comparison to the phase space location of the signal regions can be seen in figure 7.3 and 7.5.

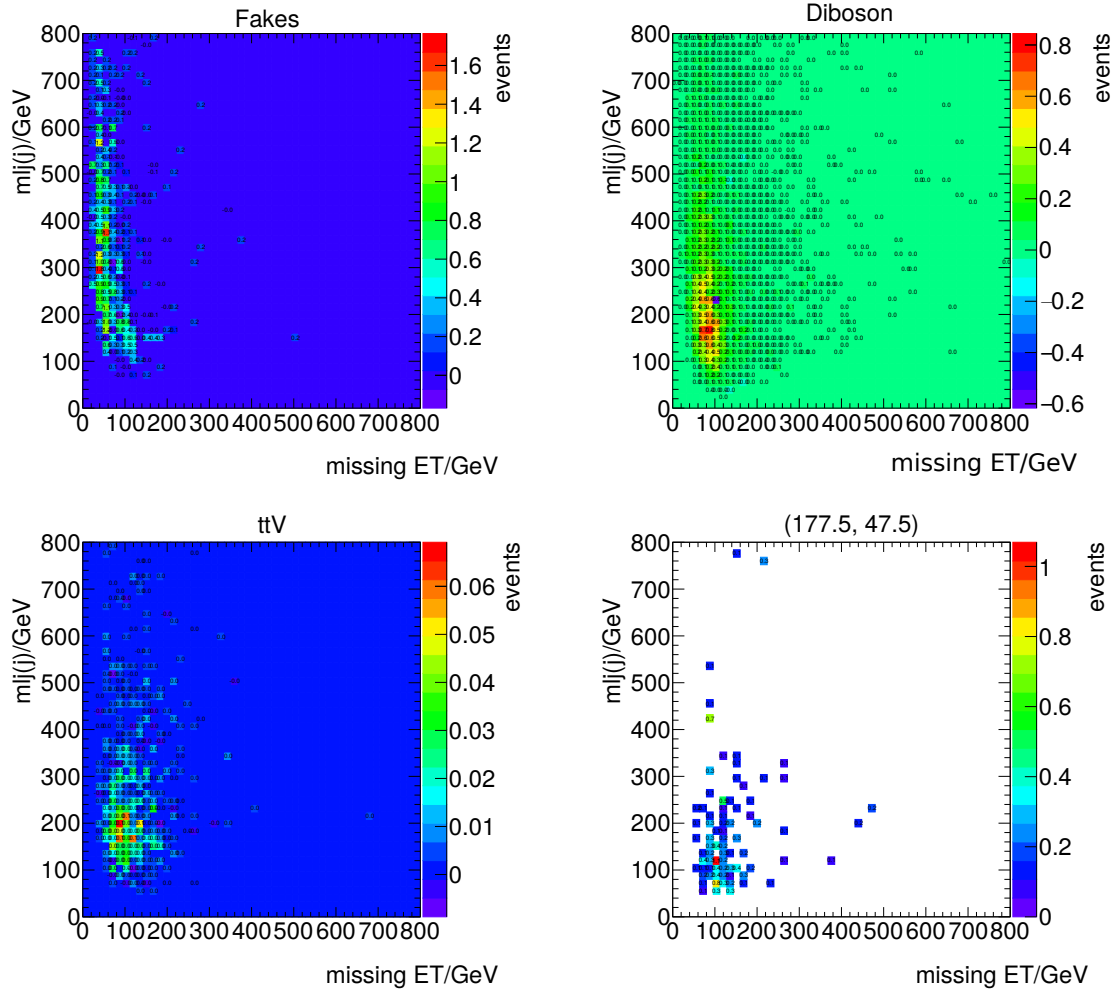


Figure 7.4: E_T^{miss} versus $m_{\ell j(j)}$ distributions for all SRjet23 cuts applied, despite the E_T^{miss} and $m_{\ell j(j)}$ requirement. The z-axis and the printed numbers show the yields per bin. Shown is the diboson, fake and ttV background and one signal mass point with $m_{\tilde{\chi}_1^\pm} = 177.5$ GeV and $m_{\tilde{\chi}_1^0} = 47.5$ GeV.

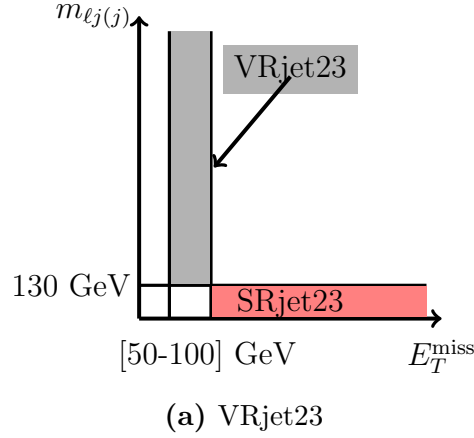


Figure 7.5: Phase space location of VRjet23 in comparison to SRjet23

	VRjet1	VRjet23
number of jets	1	2 or 3
$N_{\text{b-Jets}}$	0	0
$\Delta\eta_{\ell\ell}$ [GeV]	≤ 1.5	-
E_T^{miss} [GeV]	≥ 100	[50 – 100]
m_T [GeV]	≥ 140	≥ 240
m_{eff} [GeV]	≥ 260	≥ 240
$m_{\ell j(j)}$ [GeV]	-	≥ 130
m_{T2} [GeV]	< 80	≥ 70

Table 7.1: Validation region definition as chosen through the 2D distributions. The requirements differing from the SR definitions are marked in red.

For both validation region proposals, the signal contamination was checked over the signal grid (figure 7.6), with a maximum of 12 percent contribution in VRjet1 for the $m_{\tilde{\chi}_1^\pm} = 152.5$ GeV, $m_{\tilde{\chi}_1^0} = 22.5$ GeV mass point and the massless LSP, $m_{\tilde{\chi}_1^\pm} = 150$ GeV mass point. For VRjet23, the maximum signal contamination is 10 percent for a chargino mass of 175 GeV and a massless LSP. In figure 7.7, the background contributions in both validation regions can be seen.

Comparing figure 7.1 and 7.7, the WZ background contribution in SRjet1 of 32 % is resembled by 30% in VRjet1, with a slightly increased fake lepton contribution of 52%, compared to 49% in SRjet1. The contributions in VRjet23 shifted from 33 % Fakes and 35% WZ in SRjet23 to 43% Fakes and 23% WZ, which is mainly caused through

a rise in the charge-flip contribution from 5% to 22%. This deviation is not worrisome, as long as the agreement of MC with data in the proposed validation regions is within the uncertainties. This is indeed the case, as shown in the distributions in figure 7.8 and 7.9. The remaining kinematic distributions for VRjet1 and VRjet23 not shown here can be found in appendix A.3.

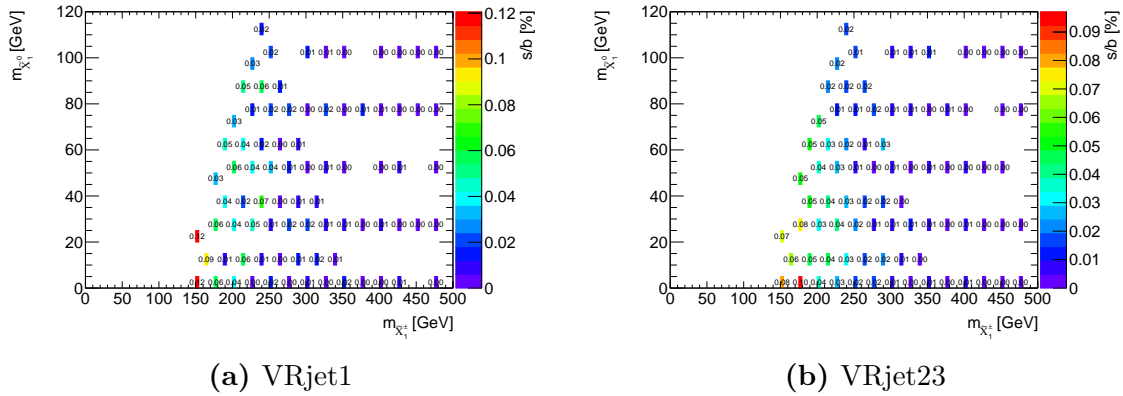


Figure 7.6: Signal contamination in VRjet1 and VRjet23

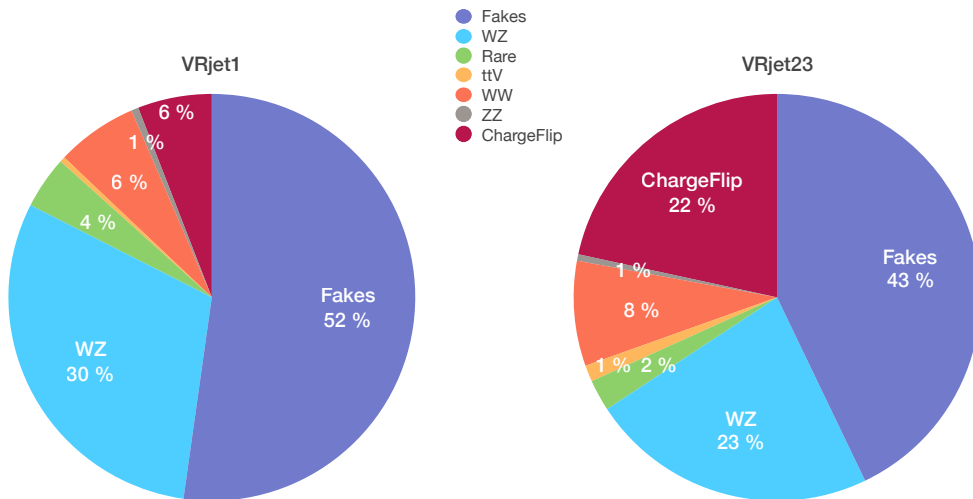


Figure 7.7: Background contributions in VRjet1 and VRjet23 in percentages

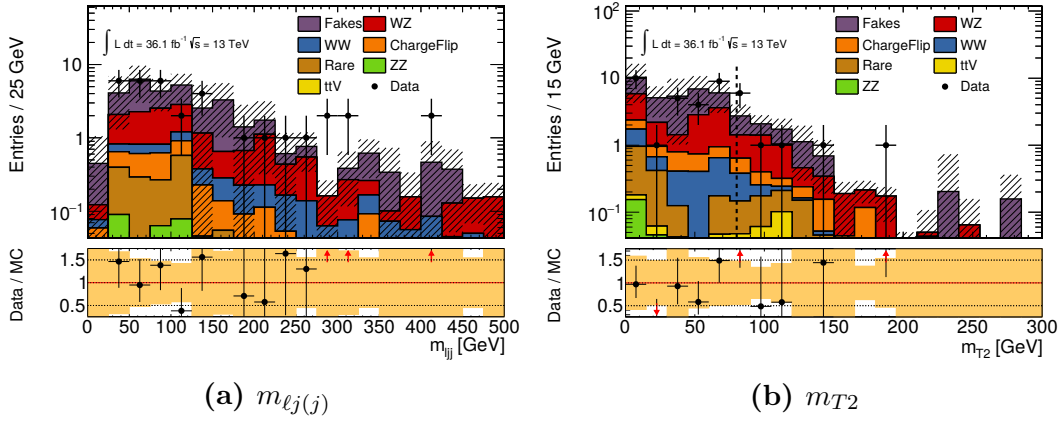


Figure 7.8: Data to Monte Carlo comparison in VRjet1 for $m_{l_{j(j)}}$ and m_{T2} . All VR cuts despite the variable shown are applied. The error bands include experimental and statistical uncertainties

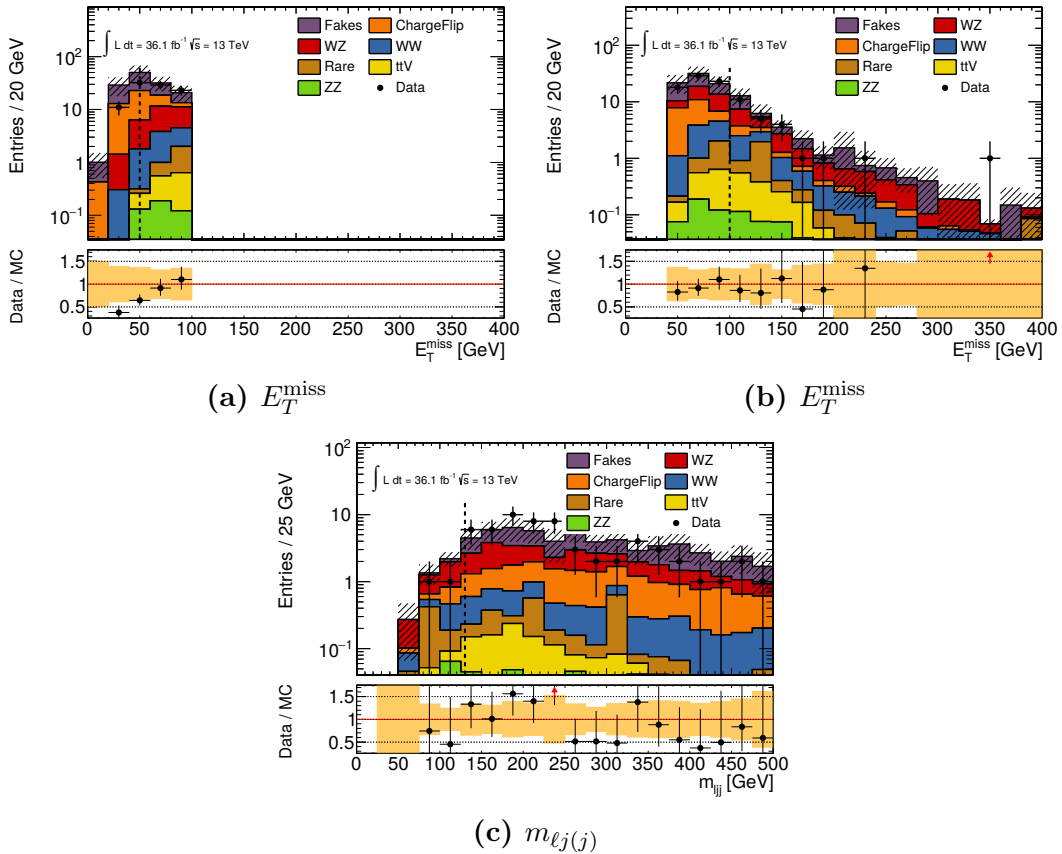


Figure 7.9: Data to Monte Carlo comparison in VRjet23 for $m_{l_{j(j)}}$ and m_{T2} . All VR cuts despite the shown variable are applied. The error bands include experimental and statistical uncertainties

Eventually, another set of validation regions was chosen to be considered in the analysis. Their background contribution was optimised to resemble the SR background composition. The optimisation is described in [19], the definition of the regions is given in table 7.2. These validation regions have been defined by D. Paredes and are further on considered in this work as the validation regions of the WH SS analysis.

	VRjet1	VRjet23
number of jets	1	[2, 3]
$\Delta\eta_{\ell\ell}$	< 1.5	–
E_T^{miss} [GeV]	[70, 100]	> 100
m_{eff} [GeV]	–	> 240
m_T	> 140	[65, 120]
$m_{\ell j(j)}$ [GeV]	> 130	> 130
m_{T2} [GeV]	–	–

Table 7.2: Final validation region definition as used in the WH SS analysis, adapted from [19]

8 Treatment of uncertainties

Within this chapter, the sources of uncertainties within the analysis are presented, distinguishing between experimental and theoretical uncertainties. Also the corresponding nuisance parameter are mentioned, further explained in section 9.2.

8.1 Experimental uncertainties

8.1.1 Object definition and weighting uncertainties

The isolation and identification working points as well as energy and momentum reconstruction within ATLAS have efficiencies which are not always modelled in MC to high enough precision. Therefore this efficiencies are corrected to the data efficiencies with scale factors. The uncertainties on reconstruction, identification and other experimental values are then presented as a variation of those scale factors. In this analysis the following variations have been taken into account. Here only a brief overview of the considered uncertainties is given, for details on the variations and how they have been calculated and provided by the different groups within ATLAS, the corresponding sources are given:

EG_Id Variation of the electron identification working point scale factor [67]

EG_Iso Uncertainty on the electron isolation working point scale factor [67]

EG_Reco Uncertainty on the electron reconstruction scale factor [67]

EG_RESOLUTION_ALL Uncertainty on the electron energy resolution [68]

EG_SCALE_ALL Uncertainty on the electron momentum scale [68]

JER Uncertainty on the jet energy resolution scale factor [69]

JES_Group1/2/3, JET Variations of the jet energy scale [70]

JVT Uncertainty on the jet vertex tagger scale factor [51]

MET_SoftTrk E_T^{miss} Soft-term scale uncertainties [54]

MET_SoftTrk_ResoPara E_T^{miss} Soft-term resolution uncertainties parallel to the hard term [54]

MET_SoftTrk_ResoPerp E_T^{miss} Soft-term resolution uncertainties perpendicular

to the hard term [54]

`MUON_Eff_Iso_stat` Stat. uncertainty on the muon isolation working point scale factor [48]

`MUON_Eff_Iso_sys` Sys. uncertainty on the muon isolation working point scale factor [48]

`MUON_Eff_stat(_lowpt)` Stat. uncertainty on the reconstruction efficiency scale factor [49]

`MUON_Eff_sys(_lowpt)` Syst. uncertainty on the reconstruction efficiency scale factor [49]

`MUON_ID` Uncertainty of the muon momentum resolution correction of the inner detector momentum reconstruction [49]

`MUON_MS` Uncertainty of the muon momentum resolution correction of the muon spectrometer momentum reconstruction [49]

`MUON_SCALE` Muon momentum scale uncertainty [49]

`MUON_TTVA_stat` Stat. uncertainty on the muon track-to-vertex association scale factor [71]

`MUON_TTVA_sys` Syst. uncertainty on the muon track-to-vertex association scale factor [71]

`TRIG` Uncertainty of the trigger scale factors calculated with the `TrigGlobalEfficiencyCorrectionTool` [45]

`btag_BT(CT,Extra,ExtraFromCharm,LightT)` Scale factor uncertainties on the different tagging efficiencies [53]

`pileup_bkg` Uncertainty on the pile-up reweighting [72]

8.1.2 Fake lepton uncertainties

The fake lepton estimation is affected by uncertainties originating in the determination of the real and fake lepton efficiencies described in section 7.1, details to the determination of those uncertainties are given in [19], here only a concise overview is given. The real lepton efficiency can vary when changing the choice of the invariant mass Z window as the probe lepton needs to be matched to the tag lepton. This is accounted for in a separate systematic uncertainty obtained through varying the Z window cut. A different trigger strategy than the one chosen in the analysis also affects the real lepton efficiency, therefore this is accounted for with an additional systematic uncertainty. The final uncertainty in the real lepton efficiency lies within the extrapolation of the kinematics in the Z tag and probe sample to the parameter space of the SRs. Additionally, the fake lepton efficiency has uncertainties in its estimation. This can be separated in an uncertainty correlated over the SR's and one uncertainty uncorrelated

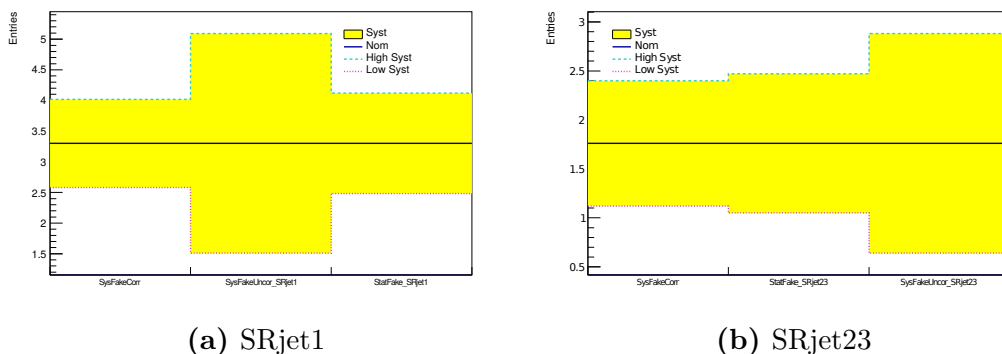


Figure 8.1: Fake lepton uncertainties in terms of up (High_Syst) and down (Low_Syst) variation of the nominal fake lepton estimation

between signal regions. The uncorrelated uncertainty originates in the variation of the fake-lepton process contributions by varying the control region cuts. Correlated between the SRs is the influence of the prompt-lepton background contribution in the control regions used to extract the real lepton efficiency. A different prompt lepton contribution is taken into account by varying the composition by 30%. This accounts for cross section uncertainties in the control region. Finally, the statistical uncertainty on the fake estimation in both signal regions is taken into account. This results in 5 nuisance parameters considered in the fit. Here `StatFake_SRjet1`, `StatFake_SRjet23`, `SysFakeUncor_SRjet1` and `SysFakeUncor_SRjet23` are the overall statistic and uncorrelated uncertainties, taking the real and fake lepton efficiency uncertainties into account. `SysFakeCorr` presents the correlated uncertainties over both signal regions, therefore only one nuisance parameter is used. In figures 8.1a and 8.1b, the uncertainties on the fake lepton estimation are summarised in comparison to the nominal fake lepton estimation.

8.1.3 Charge flip uncertainties

Uncertainties of the charge flipped lepton estimation originate from two main sources. First the efficiency of the `ElectronChargeIDSelectorTool` working point used has uncertainties, accounted for in the `ChFlip` variation. Second, the likelihood method used to estimate the remaining charge flip events has uncertainties originating from the bias of the likelihood method and the background subtraction in the likelihood method, both accounted for with the `DDChargeFlip` nuisance parameter. The likelihood method and its uncertainties are further described in [19].

8.2 Theoretical uncertainties

The theoretical uncertainties include uncertainties on the QCD scales (renormalization and factorisation scales), choice and uncertainty of the parton density function (PDF) used and the uncertainty on the cross section of the processes. For the main MC processes, WZ and Triboson (VVV), the PDF and QCD uncertainty was calculated through variations in the MC generators, a detailed description how this was estimated can be found in [19]. The cross section variation for triboson and WZ processes was taken from the ATLAS physics modelling group [73].

VVV_PDF, VVV_QCD, VVV_XSEC: Triboson PDF, QCD, cross section variation [19]

WW_PMG: WW theoretical uncertainty as proposed by [74]

WZ_PDF WZ_QCD WZ_XSEC: WZ PDF, QCD and cross section variation [19]

ZZ_PMG: ZZ theoretical uncertainty as proposed by [74]

ttH_PMG: ttH theoretical uncertainty as proposed by [75]

ttV_ttW ttV_ttWW ttV_ttZ: $t\bar{t}W$, $t\bar{t}WW$ and $t\bar{t}Z$ theoretical uncertainty as calculated by [74, 76, 75]

Process	Physics Modelling Group uncertainty
Diboson (WW,WZ,ZZ)	6% (cross section)
VVV	20% (cross section)
$t\bar{t}Z$	12% (PDF, QCD)
$t\bar{t}W$	13% (PDF, QCD)
$t\bar{t}WW$, $t\bar{t}H$, tZ	50% (PDF, QCD)

Table 8.1: Theoretical uncertainties provided by [73, 75, 74]

8.3 Summary of uncertainties before the fit

In tables 8.2, 8.3, 8.4 and 8.5, the dominant uncertainties in the validation regions and signal regions can be seen. The naming convention for nuisance parameters can already be seen, `alpha_` is used for systematic uncertainties, whereas `gamma_` is used for the statistical uncertainty. In all regions, the uncorrelated fake estimation uncertainty makes up the largest contribution, followed by the other statistical and correlated fake uncertainties. Theoretical WZ uncertainties also belong to the larger uncertainties, since WZ is the (second) largest background in the regions, next to the fake lepton background. All uncertainty contributions are given before a fit of the background

model to data, as described in the following chapter.

Uncertainty of channel	VRjet1
Total background expectation	16.84
Total background systematic	± 6.06 [35.98%]
alpha_SysFakeUncor_VRjet1	± 5.20 [30.9%]
alpha_SysFakeCorr	± 2.58 [15.3%]
alpha_StatFake_VRjet1	± 1.39 [8.3%]
gamma_stat_VRjet1_cuts_bin_0	± 0.66 [3.9%]
alpha_JER	± 0.37 [2.2%]
alpha_WZ_QCD	± 0.31 [1.8%]
alpha_WZ_Xsec	± 0.29 [1.7%]
alpha_MET_SoftTrk	± 0.28 [1.7%]
alpha_DDChargeFlip	± 0.26 [1.5%]
alpha_JES_Group3	± 0.20 [1.2%]
alpha_WZ_PDF	± 0.20 [1.2%]
alpha_MET_SoftTrk_ResoPerp	± 0.15 [0.92%]
alpha_JES_Group1	± 0.14 [0.84%]
alpha_JES_Group2	± 0.10 [0.59%]
alpha_MUON_Eff_sys	± 0.07 [0.42%]
alpha_MUON_TRIG_STAT	± 0.06 [0.38%]
alpha_EG_Id	± 0.05 [0.32%]
alpha_VVV_XSEC	± 0.05 [0.29%]
alpha_WW_PMG	± 0.05 [0.29%]
alpha_JET	± 0.05 [0.28%]
alpha_EG_SCALE_ALL	± 0.05 [0.28%]
alpha_MUON_SCALE	± 0.04 [0.26%]
alpha_EG_RESOLUTION_ALL	± 0.03 [0.15%]
alpha_MUON_MS	± 0.03 [0.15%]
alpha_EG_Iso	± 0.03 [0.15%]
alpha_ChFlip	± 0.02 [0.15%]
alpha_btag_LightT	± 0.02 [0.14%]
alpha_btag_CT	± 0.02 [0.11%]
alpha_ZZ_PMG	± 0.02 [0.11%]

Table 8.2: Breakdown of the dominant systematic uncertainties on background estimates in the various signal and validation regions. The percentages show the size of the uncertainty relative to the total expected background.

Uncertainty of channel	VRjet23
Total background expectation	55.62
Total background systematic	± 14.41 [25.90%]
alpha_SysFakeUncor_VRjet23	± 12.82 [23.0%]
alpha_SysFakeCorr	± 4.45 [8.0%]
alpha_WZ_QCD	± 3.74 [6.7%]
alpha_StatFake_VRjet23	± 2.02 [3.6%]
alpha_WZ_Xsec	± 1.16 [2.1%]
alpha_JER	± 1.02 [1.8%]
gamma_stat_VRjet23_cuts_bin_0	± 0.95 [1.7%]
alpha_WW_PMG	± 0.63 [1.1%]
alpha_WZ_PDF	± 0.55 [0.99%]
alpha_JES_Group3	± 0.53 [0.96%]
alpha_JES_Group1	± 0.50 [0.91%]
alpha_btag_CT	± 0.41 [0.73%]
alpha_MUON_TRIG_STAT	± 0.28 [0.50%]
alpha_MUON_Eff_sys	± 0.27 [0.49%]
alpha_JES_Group2	± 0.27 [0.48%]
alpha_btag_LightT	± 0.27 [0.48%]
alpha_MET_SoftTrk	± 0.23 [0.42%]
alpha_EG_Id	± 0.21 [0.38%]
alpha_JET	± 0.20 [0.35%]
alpha_btag_BT	± 0.19 [0.34%]
alpha_DDChargeFlip	± 0.17 [0.30%]
alpha_MET_SoftTrk_ResoPara	± 0.14 [0.26%]
alpha_JVT	± 0.12 [0.22%]
alpha_ttV_ttW	± 0.11 [0.20%]
alpha_MET_SoftTrk_ResoPerp	± 0.11 [0.19%]
alpha_EG_Iso	± 0.09 [0.17%]
alpha_ChFlip	± 0.09 [0.16%]
alpha_MUON_Eff_Iso_sys	± 0.07 [0.13%]
alpha_pileup_bkg	± 0.07 [0.12%]
alpha_VVV_XSEC	± 0.07 [0.12%]
alpha_MUON_Eff_stat	± 0.06 [0.12%]

Table 8.3: Breakdown of the dominant systematic uncertainties on background estimates in the various signal and validation regions. The percentages show the size of the uncertainty relative to the total expected background.

Uncertainty of channel	SRjet1
Total background expectation	6.74
Total background systematic	± 2.17 [32.16%]
alpha_SysFakeUncor_SRjet1	± 1.79 [26.6%]
alpha_StatFake_SRjet1	± 0.82 [12.2%]
alpha_SysFakeCorr	± 0.72 [10.7%]
gamma_stat_SRjet1_cuts_bin_0	± 0.42 [6.2%]
alpha_JES_Group1	± 0.20 [3.0%]
alpha_WZ_Xsec	± 0.13 [1.9%]
alpha_WZ_PDF	± 0.12 [1.8%]
alpha_MET_SoftTrk	± 0.10 [1.6%]
alpha_VVV_XSEC	± 0.08 [1.2%]
alpha_MET_SoftTrk_ResoPara	± 0.07 [1.1%]
alpha_DDChargeFlip	± 0.07 [1.1%]
alpha_JET	± 0.07 [1.0%]
alpha_JER	± 0.07 [0.98%]
alpha_WZ_QCD	± 0.07 [0.97%]
alpha_MET_SoftTrk_ResoPerp	± 0.06 [0.95%]
alpha_MUON_ID	± 0.05 [0.80%]
alpha_MUON_TRIG_STAT	± 0.03 [0.48%]
alpha_MUON_Eff_sys	± 0.03 [0.46%]
alpha_JES_Group2	± 0.03 [0.39%]
alpha_VVV_QCD	± 0.03 [0.37%]
alpha_VVV_PDF	± 0.02 [0.37%]
alpha_JES_Group3	± 0.02 [0.26%]
alpha_btag_CT	± 0.02 [0.25%]
alpha_btag_BT	± 0.01 [0.19%]
alpha_EG_Id	± 0.01 [0.17%]
alpha_EG_SCALE_ALL	± 0.01 [0.16%]
alpha_ttV_ttW	± 0.01 [0.15%]
alpha_WW_PMG	± 0.01 [0.15%]
alpha_JVT	± 0.01 [0.13%]
alpha_MUON_MS	± 0.01 [0.13%]
alpha_btag_LightT	± 0.01 [0.12%]
alpha_pileup_bkg	± 0.01 [0.11%]
alpha_MUON_Eff_Iso_sys	± 0.01 [0.11%]
alpha_ChFlip	± 0.01 [0.11%]
alpha_MUON_Eff_stat	± 0.01 [0.11%]

Table 8.4: Breakdown of the dominant systematic uncertainties on background estimates in the various signal regions. The percentages show the size of the uncertainty relative to the total expected background.

8.3 Summary of uncertainties before the fit

Uncertainty of channel	SRjet23
Total background expectation	5.33
Total background systematic	± 1.59 [29.75%]
alpha_SysFakeUncor_SRjet23	± 1.12 [21.0%]
alpha_StatFake_SRjet23	± 0.71 [13.3%]
alpha_SysFakeCorr	± 0.64 [12.0%]
gamma_stat_SRjet23_cuts_bin_0	± 0.34 [6.4%]
alpha_MET_SoftTrk	± 0.24 [4.6%]
alpha_WZ_QCD	± 0.24 [4.4%]
alpha_JES_Group1	± 0.23 [4.2%]
alpha_JER	± 0.12 [2.2%]
alpha_WZ_Xsec	± 0.11 [2.1%]
alpha_MET_SoftTrk_ResoPara	± 0.10 [1.8%]
alpha_btag_BT	± 0.10 [1.8%]
alpha_WZ_PDF	± 0.07 [1.4%]
alpha_MET_SoftTrk_ResoPerp	± 0.05 [0.88%]
alpha_MUON_TRIG_STAT	± 0.04 [0.66%]
alpha_MUON_Eff_sys	± 0.03 [0.63%]
alpha_btag_LightT	± 0.03 [0.60%]
alpha_btag_CT	± 0.03 [0.60%]
alpha_VVV_XSEC	± 0.03 [0.58%]
alpha_WW_PMG	± 0.03 [0.58%]
alpha_MUON_SCALE	± 0.03 [0.56%]
alpha_EG_SCALE_ALL	± 0.03 [0.55%]
alpha_JES_Group3	± 0.03 [0.55%]
alpha_DDChargeFlip	± 0.03 [0.51%]
alpha_EG_RESOLUTION_ALL	± 0.03 [0.50%]
alpha_JVT	± 0.03 [0.48%]
alpha_MUON_MS	± 0.02 [0.45%]
alpha_JET	± 0.02 [0.40%]
alpha_JES_Group2	± 0.02 [0.37%]
alpha_ttV_ttW	± 0.02 [0.31%]
alpha_EG_Id	± 0.01 [0.28%]
alpha_VVV_QCD	± 0.01 [0.23%]
alpha_ttH_PMG	± 0.01 [0.20%]
alpha_pileup_bkg	± 0.01 [0.17%]
alpha_MUON_Eff_Iso_sys	± 0.01 [0.16%]
alpha_MUON_Eff_stat	± 0.01 [0.14%]
alpha_EG_Iso	± 0.01 [0.13%]
alpha_VVV_PDF	± 0.01 [0.13%]
alpha_ChFlip	± 0.01 [0.11%]

Table 8.5: Breakdown of the dominant systematic uncertainties on background estimates in the various signal regions. The percentages show the size of the uncertainty relative to the total expected background. 73

9 Results

After estimating all Standard Model backgrounds with a similar final state as the SUSY signal, validating their estimation and considering all possible sources of uncertainties, the SM expectation in the signal regions can be compared to ATLAS data. The final results of this comparison are presented in the following chapter.

9.1 Expected and observed yields

In figure 9.1, the kinematic distributions in SRjet1 are shown. Within the pseudorapidity range of $\Delta\eta_{\ell\ell} \in [1.5, 2.0]$ the Monte Carlo simulation of WZ processes includes an event with high Monte Carlo weights. This is due to low statistics, preventing a compensation of this one highly weighted event. In SRjet1, two data events have been observed, this is an underfluctuation of data in comparison to the overall 6.74 expected SM events. In the two and three jet signal region, SRjet23, in figure 9.2 a slight overfluctuation of data with respect to SM expectation was observed, which is still in agreement with the background prediction. This is shown in the m_T distribution. Comparing the ratio of data to Monte Carlo expectation next to the SR shows a good agreement, ensuring a validated background estimation. Table 9.1 shows a breakdown of the SM background expectation in comparison to the 36.1 fb^{-1} of $\sqrt{s} = 13\text{TeV}$ collision data collected with ATLAS in 2015 and 2016, all experimental and theoretical uncertainties are considered.

9.2 Statistical interpretation

Comparing the compatibility of the observed events with the SM backgrounds, hypotheses tests have been carried out. To elaborate the results of those tests, in the following the mathematical concepts of the statistical interpretation of results is presented, as well as the software setup used to perform hypothesis tests. The mathematical description follows [77], whereas the technical implementation largely follows descriptions in [78] and [79].

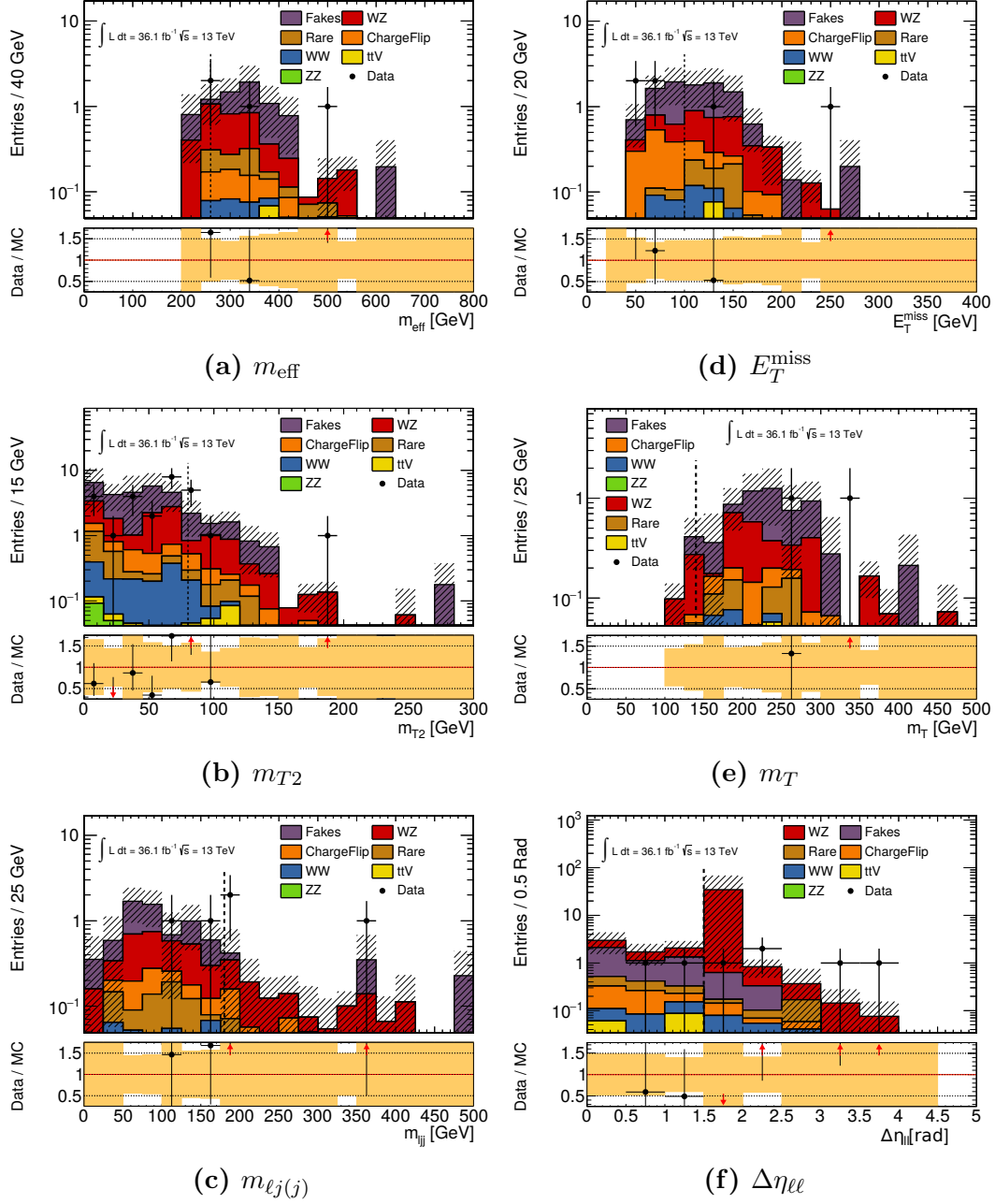


Figure 9.1: Data versus Monte Carlo expectation for SRjet1. For each plot the requirement on the shown variable is dropped. The uncertainty band includes all experimental uncertainties, without considering theoretical uncertainties.

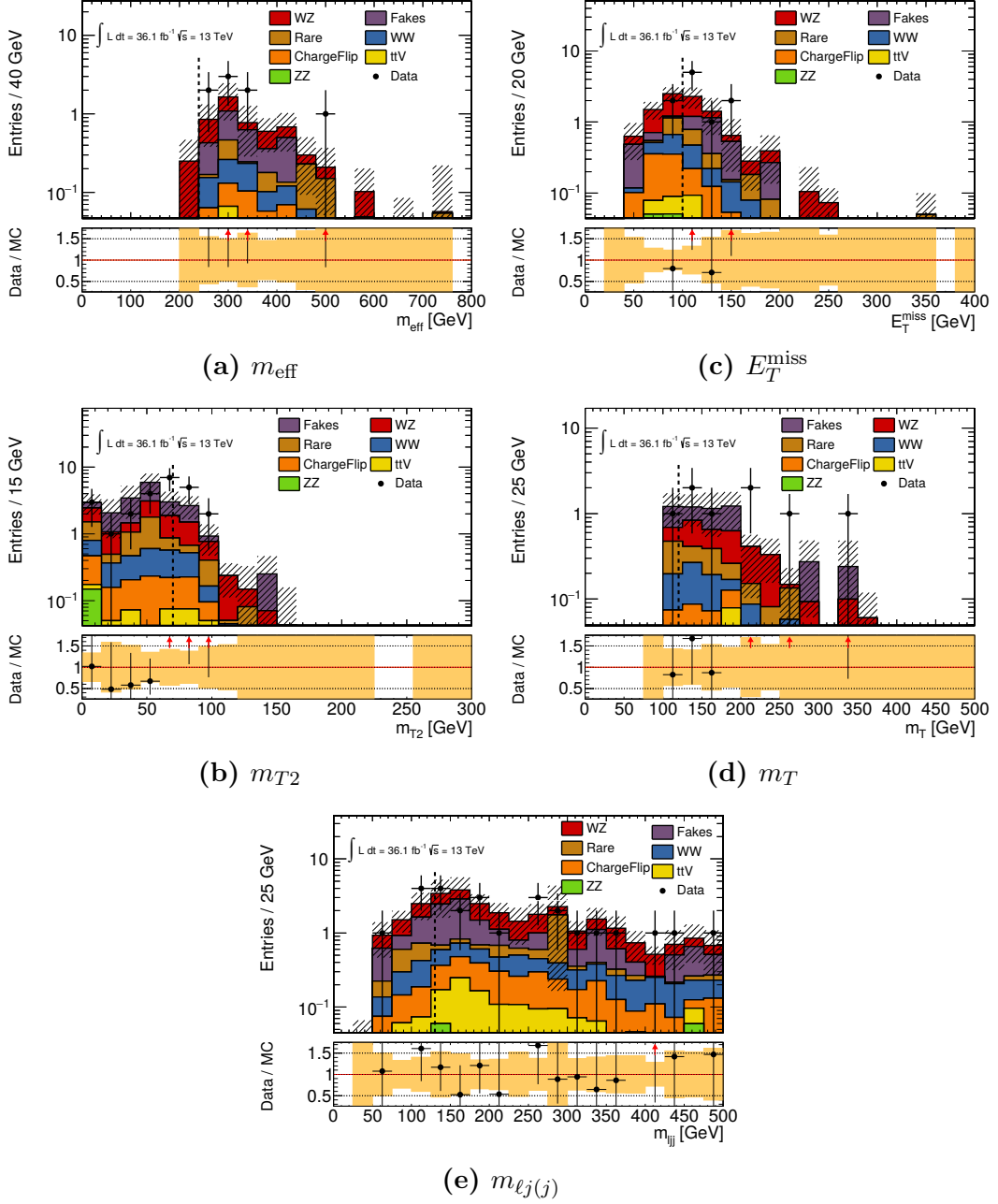


Figure 9.2: Data versus Monte Carlo expectation for SRjet23. For each plot the requirement on the shown variable is dropped. The uncertainty band includes all experimental uncertainties, without considering theoretical uncertainties.

	SRjet1	SRjet23	VRjet1	VRjet23
Observed events	2	8	17	54
SM events	6.74 ± 2.17	5.33 ± 1.59	16.84 ± 6.06	55.62 ± 14.41
Fakes events	3.30 ± 2.10	1.76 ± 1.47	8.02 ± 5.97	20.08 ± 13.72
WZ events	2.18 ± 0.42	1.85 ± 0.52	4.91 ± 0.83	19.33 ± 4.16
Rare events	0.44 ± 0.13	0.73 ± 0.17	0.78 ± 0.33	2.47 ± 0.43
ttV events	0.12 ± 0.04	0.14 ± 0.04	0.04 ± 0.01	0.96 ± 0.14
WW events	0.17 ± 0.03	0.51 ± 0.07	0.80 ± 0.12	10.48 ± 0.78
ZZ events	0.06 ± 0.02	0.07 ± 0.02	0.30 ± 0.06	0.25 ± 0.08
ChargeFlip events	0.47 ± 0.07	0.27 ± 0.03	2.00 ± 0.26	2.07 ± 0.17

Table 9.1: Breakdown of the SM Monte Carlo expectation in comparison to observed data. The errors shown include theoretical, experimental as well as statistical uncertainties.

9.2.1 Statistical concepts

In a simple counting experiment, the probability density function (PDF) is given by a Poisson distribution, with the expectation value given by the measured number of events. In a distribution with multiple bins, each bin content is described by a Poissonian, eventually taking the product of all single bins to describe the whole distribution.

Describing both signal regions in this analysis, a likelihood function as in 9.1 [78] is constructed. The Poisson distribution is determined through the observed number of events in the signal regions, n_S , the expectation value λ_S , depending on the signal strength μ , background expectation \mathbf{b} and nuisance parameters $\boldsymbol{\theta}$. An additional constraint term is included in the likelihood. Variations originating from different uncertainties are mapped onto a Gaussian distribution C_{syst} in a way that the $\pm 1\sigma$ variations refer to the up and down variations, whereas the mean is the nominal Monte Carlo expectation. Each Gaussian describes one nuisance parameter, determined through one uncertainty. Here $\boldsymbol{\theta}^0$ are the central values of the auxiliary measurements determining the uncertainties.

$$\begin{aligned}
 L(n, \boldsymbol{\theta}^0 | \mu, \mathbf{b}, \boldsymbol{\theta}) &= P_{\text{SR}} \times C_{\text{syst}} \\
 &= P(n_S | \lambda_S(\mu, \mathbf{b}, \boldsymbol{\theta})) \times C_{\text{syst}}(\boldsymbol{\theta}^0, \boldsymbol{\theta})
 \end{aligned}
 \tag{9.1}$$

Using this likelihood, a test statistic can be constructed. The profile likelihood ratio (9.2) is built, being the fraction of conditionally maximised likelihood for a given signal strength μ , over the unconditionally maximised likelihood function, with $\hat{\mu}$, $\hat{\boldsymbol{\theta}}$ being the maximum-likelihood estimators of signal strength and nuisance parameters.

$$\lambda(\mu) = -2 \ln \frac{L(\mu, \hat{\boldsymbol{\theta}})}{L(\hat{\mu}, \hat{\boldsymbol{\theta}})} \quad (9.2)$$

With this profile likelihood ratio a test statistic t_μ is built:

$$t_\mu = -2 \ln \lambda(\mu) \quad (9.3)$$

A test statistic serves as single-number comparative value of repeated experiments. In the case of an exclusion limit, one is interested in discarding the 'signal plus background' null hypothesis, assuming that a specific SUSY signal model with certain fixed parameters is realised in nature, on top of the SM backgrounds. With the p-value p_μ , the probability of obtaining a similar or even more 'extreme' outcome can be quantified. A more extreme outcome can refer to a lower amount of events observed in the signal-plus-background hypothesis or a higher amount of events observed in the background-only hypothesis. The p-value is defined as the integral of the test-statistic distribution $f(t_\mu|\mu)$, under a certain signal strength assumption:

$$p_\mu = \int_{t_{\mu,obs}}^{\infty} f(t_\mu|\mu) dt_\mu \quad (9.4)$$

The test-statistic distribution $f(t_\mu|\mu)$ usually needs to be obtained through pseudo experiments, but in the large statistics limit, the distribution can be asymptotically estimated, as described by Wilks' theorem [77].

The probability obtained through the p-value can also be interpreted in terms of Gaussian standard deviations: How many σ standard deviations is the measured value away from the expectation value? The 'significance' in standard deviations can be obtained from the p-value through the quantile function [77]:

$$Z = \Phi^{-1}(1 - p) \quad (9.5)$$

Within this work, the CLs value (9.6) [80] is used as a sensitivity measure in terms of exclusion limits. It is defined as the ratio of the p-value calculated under the signal plus background hypothesis over $1 - p_b$, with p_b being the p-value under the SM only hypothesis.

$$CL_S = \frac{p_{s+b}}{1 - p_b} \quad (9.6)$$

An exclusion of the signal plus background hypothesis at 95% confidence level refers to a CL_S value smaller than 5%.

9.2.2 HistFitter setup

The statistical interpretation is done using the HistFitter software framework [78]. It is a wrapper around RooStats, RooFit and HistFactory methods [81, 82, 83] including some further tools, where analysis concepts like signal and control regions are already included and complex statistical models are easily built. All experimental, theoretical and statistical uncertainties are included in the likelihood function via Gaussian constraint terms, each describing one nuisance parameter. Uncertainties influencing the SRs simultaneously are correlated across regions. No control regions have been defined in this analysis, therefore the statistical interpretation is only dependent on the signal regions and the corresponding yields and uncertainties within them.

9.2.3 Exclusion limits

For each signal model across the signal grid detailed in section 5.2, a model-dependent exclusion fit was performed, testing the agreement of data with the hypothesis of this signal model on top of the SM expectation. As already mentioned, systematic uncertainties can be correlated with each other. This is accounted for within the exclusion in the correlation matrix, graphically shown in figure 9.3. This is the only difference between the quadratic addition of uncertainties, which is assuming uncorrelated uncertainties. The total error on the background is given by error propagation. Within this analysis, no large correlation between uncertainties is visible.

If the observed data events are deviating from the expected Monte Carlo estimation, taking the uncertainties into account, the fit can shift the nominal background values through shifting the nominal uncertainty values. This ‘profiling’ or pull is visible in figure 9.4. All nuisance parameters are listed, with their values after the fit shown, including $\pm 1\sigma$ variations. Most of the nuisance parameters remain at their nominal value, whereas one nuisance parameter attached to the uncertainty on the jet energy scale (JES) and the uncorrelated non-prompt lepton estimation uncertainties get pulled. This is due to the underfluctuation of data seen in SRjet1 and the slight overfluctuation of data in SRjet23. The fake uncertainties are the largest uncertainties within this analysis and therefore offer some scope of variation in the fit of the likelihood to data. The JES uncertainty receives a slight pull, since it influences the number of jets and is therefore able to shift events from one SR into the other one, due to varying the jet multiplicity. This shift in the fake yields in the exclusion fit is also visible in table 9.2, where the post- and pre-fit yields are shown. The exemplary signal point presented in the table is fitted to almost zero, but also the non-prompt lepton estimation is pulled to low values through the corresponding uncorrelated uncertainties.

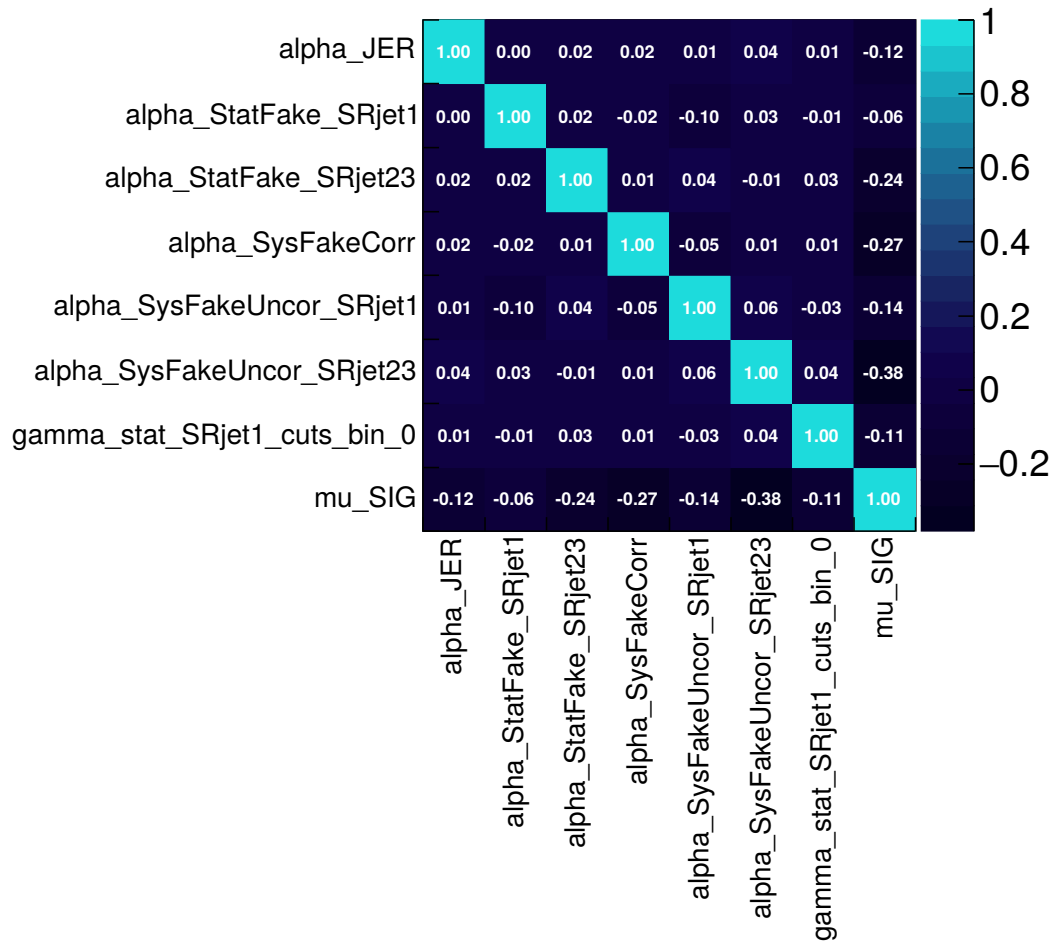


Figure 9.3: Correlation matrix of the dominating nuisance parameters included in the likelihood

table.results.yields channel	SRjet1	SRjet23
Observed events	2	8
Fitted bkg events	4.54 ± 1.52	6.35 ± 1.34
Fitted Fakes events	$0.93^{+1.54}_{-0.93}$	2.07 ± 1.46
Fitted WZ events	2.08 ± 0.38	1.93 ± 0.57
Fitted Rare events	0.43 ± 0.12	0.72 ± 0.18
Fitted ttV events	0.12 ± 0.04	0.14 ± 0.04
Fitted WW events	0.16 ± 0.02	0.53 ± 0.08
Fitted ZZ events	0.05 ± 0.02	0.07 ± 0.02
Fitted ChargeFlip events	0.47 ± 0.07	0.27 ± 0.03
Fitted C1N2_Wh_hall_175p0_0p0 events	$0.30^{+0.55}_{-0.30}$	$0.63^{+1.17}_{-0.63}$
MC exp. SM events	11.02 ± 2.32	13.93 ± 2.28
Fakes events	3.30 ± 2.10	1.76 ± 1.47
MC exp. WZ events	2.18 ± 0.38	1.85 ± 0.54
MC exp. Rare events	0.44 ± 0.12	0.73 ± 0.18
MC exp. ttV events	0.12 ± 0.04	0.14 ± 0.04
MC exp. WW events	0.17 ± 0.03	0.51 ± 0.08
MC exp. ZZ events	0.06 ± 0.02	0.07 ± 0.03
ChargeFlip events	0.47 ± 0.07	0.27 ± 0.03
MC exp. C1N2_Wh_hall_175p0_0p0 events	4.29 ± 0.73	8.60 ± 1.35

Table 9.2: Background yields in the signal regions before and after the exclusion fit, with one example signal mass point

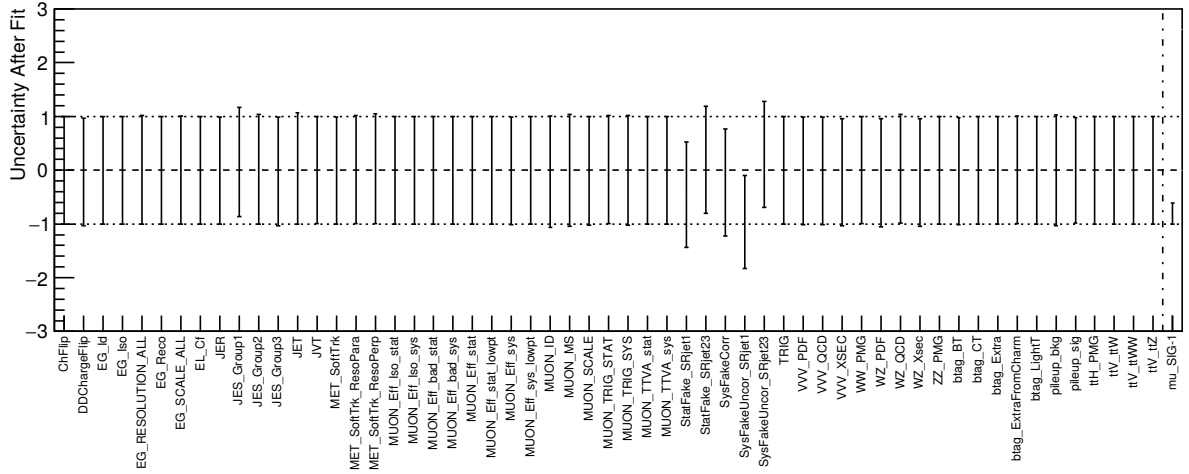


Figure 9.4: Pull of the nuisance parameters after the exclusion fit. Shown are all nuisance parameters and their variation in terms of gaussian standard deviations.

With no significant excess seen in the signal regions, exclusion limits can be set within the simplified model chargino neutralino production considered. In figure 9.5 the $(m_{\tilde{\chi}_1^0} - m_{\tilde{\chi}_1^\pm})$ mass plane is shown. Chargino masses below 150 GeV have already been excluded by previous analyses [22]. The dashed line shows the expected exclusion, if the observed data would be consistent with the Monte Carlo SM background expectation. The yellow band surrounding this line gives the $\pm 1\sigma$ uncertainties on the expected limit. All limits refer to a 95% confidence limit, which corresponds to a CLs value smaller than 5%. The red line is the observed limit, showing the actual results of the hypothesis test for data. Due to the underfluctuation in data in the one jet signal region, additional mass points at 225 and 237 GeV chargino at 25 and 37 GeV neutralino mass are excluded within this model. The grey numbers refer to the observed CLs value and clarify the discrete parameter points tested. Between the discrete signal mass points simulated in Monte Carlo, the significance value is interpolated.

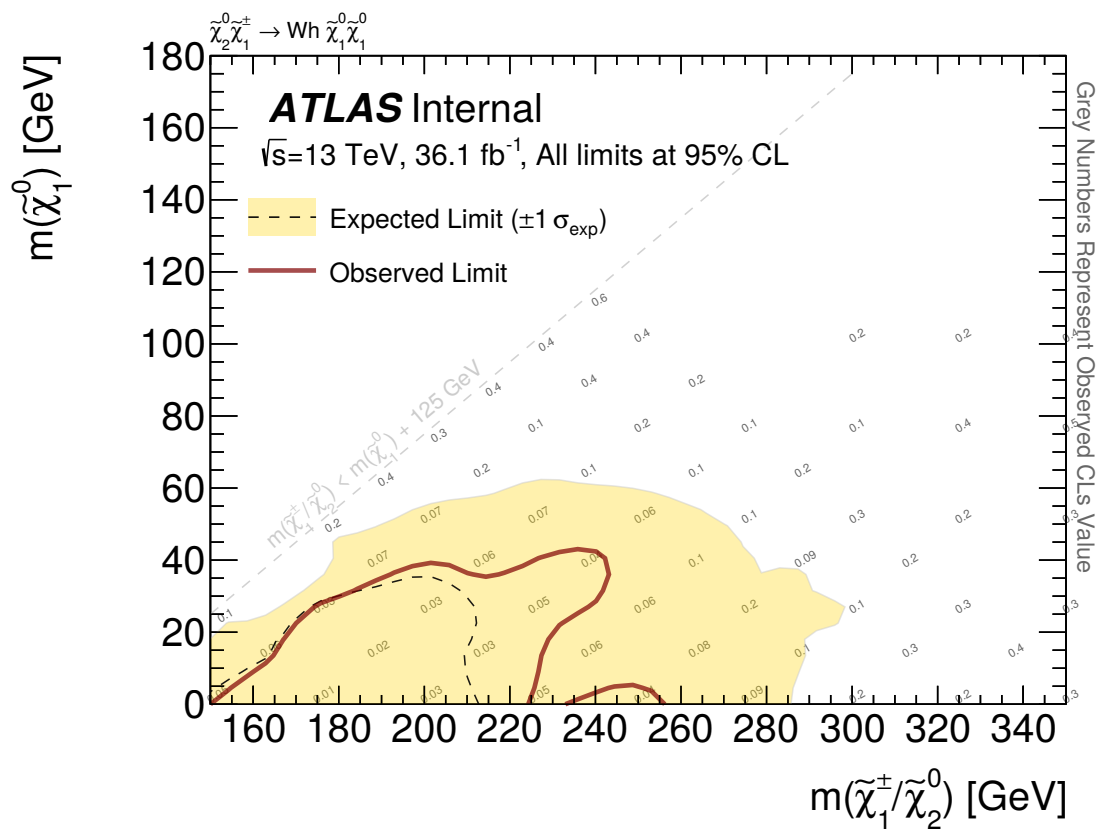


Figure 9.5: Excluded parameter space in the $m_{\tilde{\chi}_1^0} - m_{\tilde{\chi}_1^\pm}$ plane for the considered simplified model chargino neutralino production

10 Future prospects

Observing no significant excess in the 2015 and 2016 dataset of 36.1 fb^{-1} , it is also of interest to future analyses to see how sensitive the presented analysis would be with more available data. To check this, the analysis setup as presented previously was applied to higher data statistics. The Monte Carlo and data-driven processes as well as the signal prediction was scaled to several integrated luminosities. All uncertainties have been considered and the full statistical interpretation was performed. 2015-2017 a total integrated luminosity of 80 fb^{-1} was recorded with the ATLAS detector, fulfilling a good enough quality to be considered for physics analyses, as can be seen in figure 10.1.

Therefore, the discovery sensitivity for 80 fb^{-1} was studied in figure 10.2a. Comparing the discovery sensitivity at 80 fb^{-1} with the sensitivity at 36.1 fb^{-1} in figure 10.3a, an overall increase in significance can be observed. Additionally, a slight increase in the sensitivity towards higher $\tilde{\chi}_1^\pm$ masses can be observed. Increasing the luminosity further to 120 and 140 fb^{-1} , which will probably be reached at the end of 2018, the trend towards higher chargino masses does not continue, although the overall significance is rising. Before the long shutdown of the LHC planned in 2024, an integrated luminosity of 300 fb^{-1} can be reached. Comparing the sensitivity with this high integrated luminosity with the initial 36.1 fb^{-1} in figure 10.3, an overall sensitivity increase can be observed, with a highest significance difference of 0.85σ . A comparison of the considered int. luminosities for massless LSP signal points and a chargino mass between $m_{\tilde{\chi}_1^\pm} = 150 \text{ GeV}$ and $m_{\tilde{\chi}_1^\pm} = 300 \text{ GeV}$ can be seen in figure 10.4. Already with this

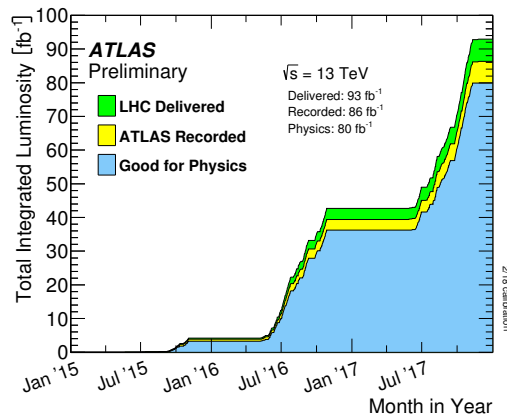


Figure 10.1: Total integrated luminosity over time [84]

extrapolation to higher int. luminosities, discovery sensitivities slightly below 3σ can be reached. Not considered in these extrapolations are re-optimisations of the signal regions for higher int. luminosities, where an higher available statistics would allow for stricter kinematic requirements. With the 2017 data taking, several reconstruction and identification algorithms have been improved, leading to lower uncertainties. This might also lead to an higher discovery sensitivity for the simplified chargino neutralino production, making it an interesting process also for future analyses.

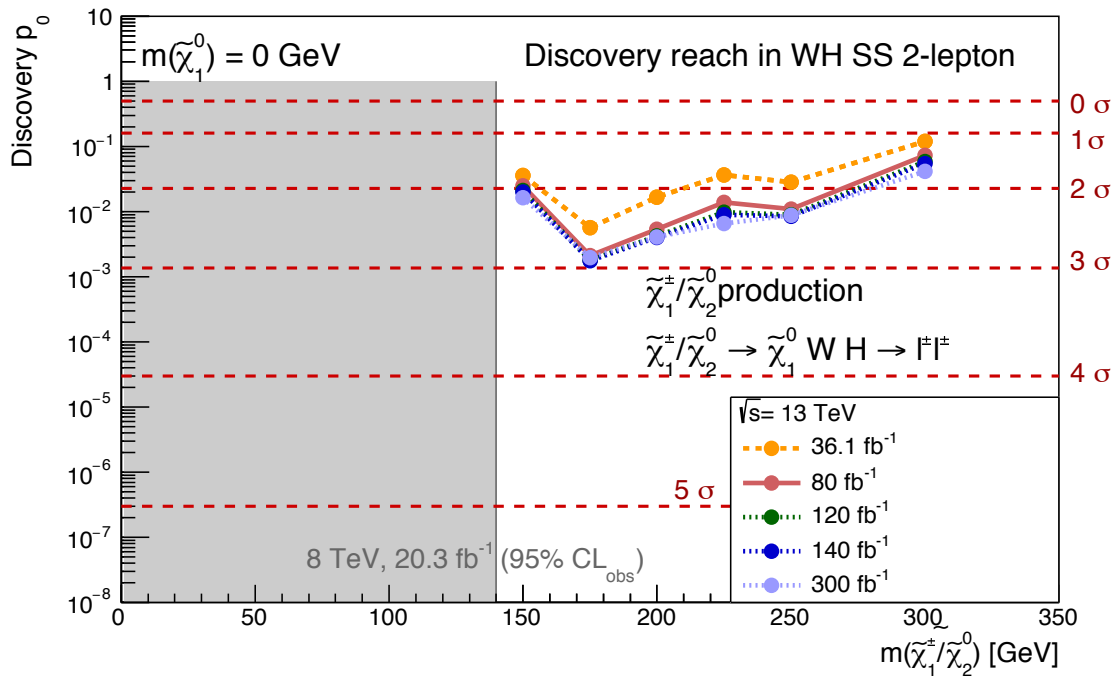
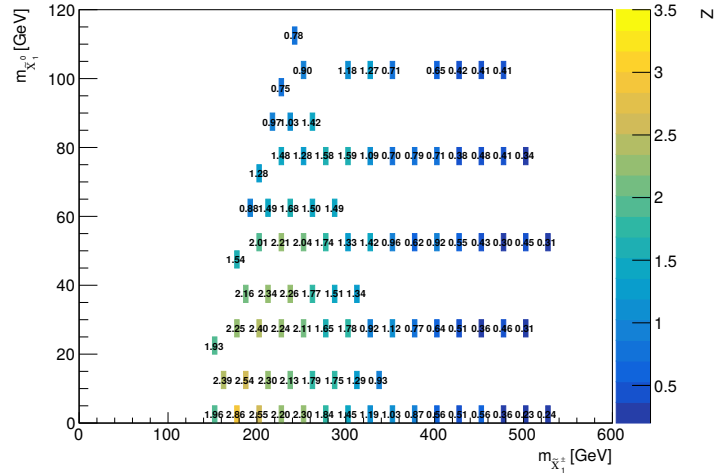
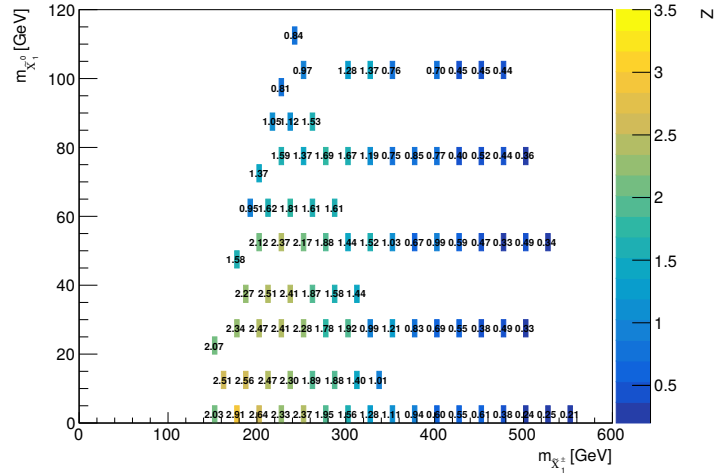


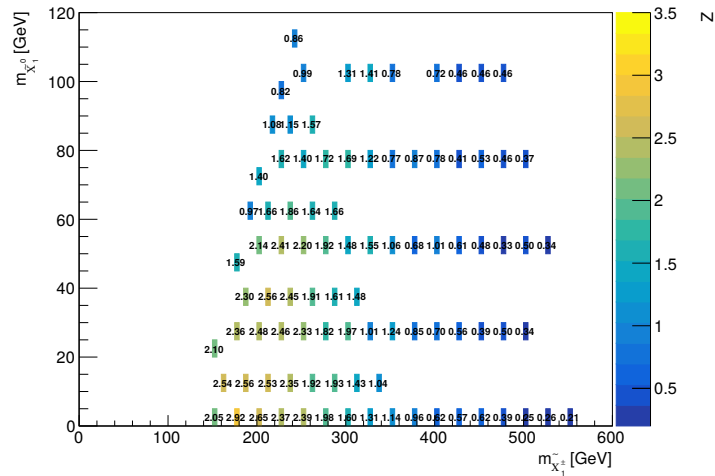
Figure 10.4: Discovery significance for massless LSP signal points



(a) $\int \mathcal{L} = 80 \text{ fb}^{-1}$

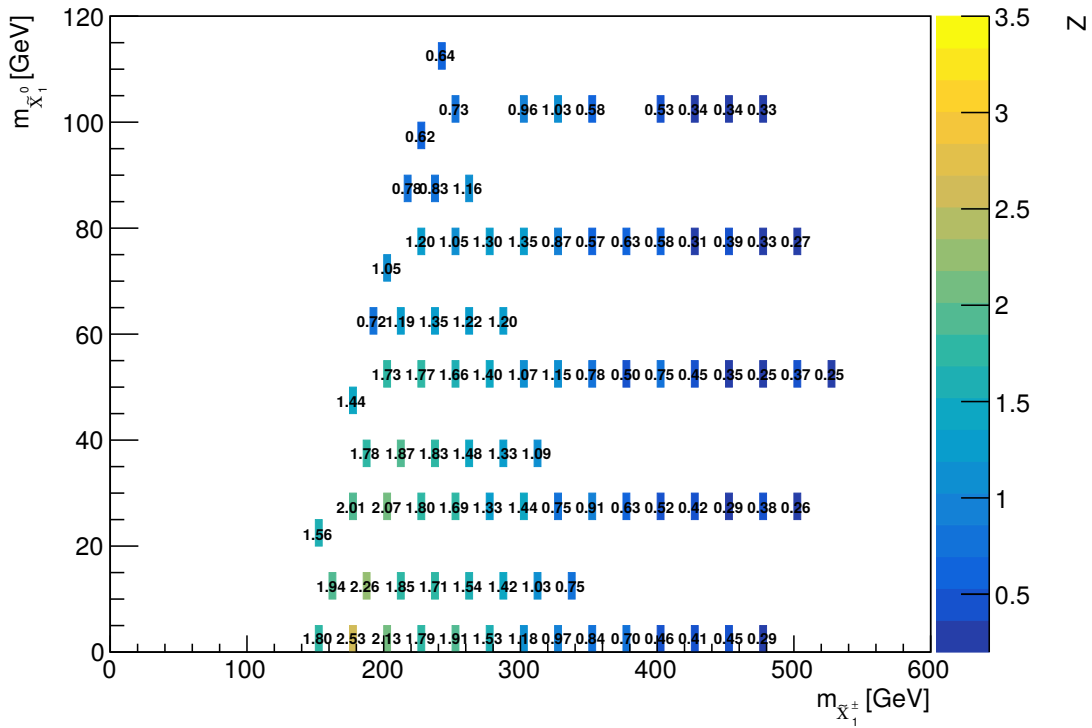


(b) $\int \mathcal{L} = 120 \text{ fb}^{-1}$

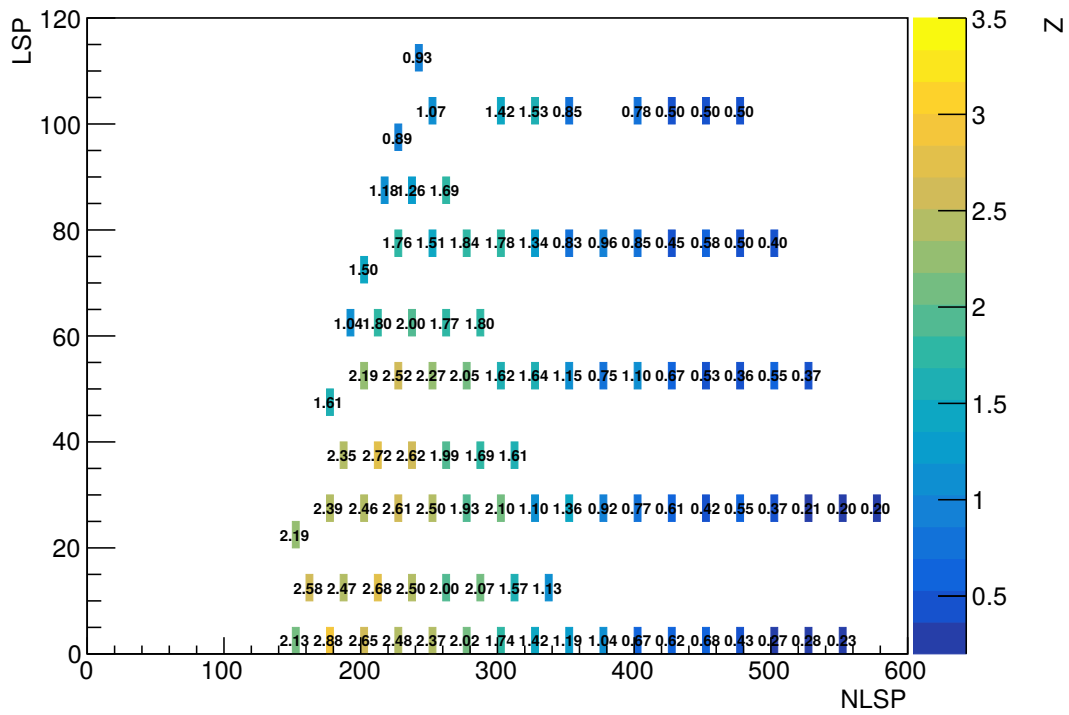


(c) $\int \mathcal{L} = 140 \text{ fb}^{-1}$

Figure 10.2: Discovery sensitivity in terms of Gaussian standard deviations for an integrated luminosity of 80, 120 and 140 fb^{-1}



(a) $\int \mathcal{L} = 36.1 \text{ fb}^{-1}$



(b) $\int \mathcal{L} = 300 \text{ fb}^{-1}$

Figure 10.3: Discovery sensitivity in terms of Gaussian standard deviations for an integrated luminosity of 36.1 fb^{-1} compared to 300 fb^{-1}

11 Conclusion

Being able to not only solve the Hierarchy problem but also providing a viable particle candidate for dark matter, supersymmetry offers a promising extension of the Standard Model of Particle Physics. Searching for the Minimal Supersymmetric Standard Model with its large number of free parameters is a challenging theory to search for. Therefore searches are usually considering simplified models.

In simplified models only a small set of particles is studied by decoupling all other particles. In the model considered in this thesis, the $\tilde{\chi}_1^\pm$ and $\tilde{\chi}_1^0$ masses are the free parameters, where the $\tilde{\chi}_1^\pm$ and $\tilde{\chi}_2^0$ are mass degenerated. This mass hierarchy is realised by considering the $\tilde{\chi}_1^\pm$ and $\tilde{\chi}_2^0$ to be wino-like and the $\tilde{\chi}_1^0$ to be bino-like. Compared to other simplified models considering chargino neutralino production, the simplified model considered here adds the feature of a direct $\tilde{\chi}_2^0 / \tilde{\chi}_1^\pm / \tilde{\chi}_1^0$ - Higgs coupling. Evidence of this would be a direct proof of SUSY particles coupling to the Higgs boson and therefore contributing to the Higgs mass radiative loop corrections and thus possibly fixing the Higgs mass to its observed value.

Within this work, the chargino neutralino production was searched for, where charginos and neutralinos decay via a W and Higgs boson and result in a final state with two same-sign leptons, missing transverse energy and jets. The E_T^{miss} is due to the stable neutralino LSP, but can also be caused by neutrinos in standard model processes. The main SM processes to be considered in this SUSY search is the production of W/Z diboson processes leading to dileptonic final states. The main reducible background is given through non-prompt fake leptons, originating from heavy flavor meson decays and light quark meson decays.

In order to define SUSY signal enhanced parameter spaces, an optimisation was carried out. A set of kinematic variables was used to design a signal region with exactly one jet and an additional region with two or three jets in the event. Both signal regions are orthogonal due to their requirement on the jet multiplicities and are thus statistically combined. A maximum discovery sensitivity of 2.52σ was reached for the combined regions, optimising for an integrated luminosity of $\int \mathcal{L} = 36.1 \text{ fb}^{-1}$.

For validating the WZ estimation through Monte Carlo, validation regions have been designed. A set of two validation regions, one for each jet-multiplicity signal region, was defined, showing a similar background contribution to the signal regions, and additionally validate the fake lepton estimation. A good agreement between data and MC estimation was observed in both validation regions.

After taking all experimental and theoretical uncertainties into account, no significant excess over the SM prediction was observed in 2015 and 2016 data collected by the ATLAS experiment. This was used to set exclusion limits at 95 % confidence level. For massless LSP's ($m_{\tilde{\chi}_1^0} = 0$ GeV), chargino masses up to $m_{\tilde{\chi}_1^\pm} = 225$ GeV have been excluded, with an additional excluded point at $m_{\tilde{\chi}_1^\pm} = 250$ GeV and $m_{\tilde{\chi}_1^0} = 0$ GeV. This presents an improvement in the excluded phase space in comparison to the previous run 1 WH same-sign analysis.

To estimate the sensitivity reach in future larger datasets, the discovery sensitivity for different luminosities has been computed, using the signal region definitions and uncertainty predictions as defined in the 2015 and 2016 data analysis, showing an enhanced discovery sensitivity after increasing the luminosity to 140 fb^{-1} , which is going to be realised with 2017 and 2018 data included. A re-optimisation of the signal regions would further enhance this sensitivity.

A Appendix

A.1 List of MC Samples

Diboson processes are simulated using **SHERPA**, fully leptonic triboson processes are simulated using **SHERPA v2.2.1** [85]. $W/Z + \text{jets}$ processes are generated with **SHERPA 2.2.1** [85], normalized to their next-to-next-to-leading order theoretical cross section [86]. Single top quark background samples are generated with **POWHEG** [87] using the CT10 PDF set [88]. **POWHEG** is interfaced to **PYTHIA 6.427** [89] with the CTEQ6L1 PDF set using the Perugia2012 [90] tune.

Multitop processes are simulated using **Madgraph** [91] interfaced to **Pythia**. $t\bar{t}H$ processes are simulated using **MC@NLO** [92] and **Herwig** [93]. All MC samples are produced with the p2949 tag.

The simplified chargino neutralino model was simulated using **Madgraph** [91] interfaced with **Pythia** [89]. The samples have been filtered at generation level with a 2L7 filter, requiring two leptons with $p_T > 7$ GeV. The considered dataset ID's are between 393820 and 393914.

In the following tables, the Monte Carlo samples for the SM backgrounds are listed with their respective cross-section, filter efficiency, k-factor, Generator efficiency and the integrated Luminosity. The backgrounds are summarized according to the categorization chosen in the shown distributions. All blue marked samples are Monte Carlo samples including two prompt, same-sign leptons. These samples are also considered after including the data-driven charge-flip and fake lepton estimation, whereas all not-highlighted samples are removed when including the data-driven estimations in order to remove overlaps in the estimation.

Dataset ID	Process	Tags	$\sigma \times \epsilon$ [pb]	k -factor	G. eff.	$\mathcal{L}_{int}[\text{fb}^{-1}]$
361069	Sherpa_CT10_llvjj_ss_EW4	e3836_s2726_r7772_r7676	0.0258	0.91	1.000	20984.256
361070	Sherpa_CT10_llvjj_ss_EW6	e3836_s2608_r7772_r7676	0.0434	0.91	1.000	12363.429
361071	Sherpa_CT10_llvjj_EW6	e3836_s2726_r7772_r7676	0.0423	0.91	1.000	25415.025
361072	Sherpa_CT10_llljj_EW6	e3836_s2608_s2183_r7772_r7676	0.0315	0.91	1.000	2093.411
361073	Sherpa_CT10_ggllll	e3836_s2608_s2183_r7772_r7676	0.0210	0.91	1.000	26331.662
361077	Sherpa_CT10_ggllvv	e3836_s2608_s2183_r7772_r7676	0.8549	0.91	1.000	256.820
363356	Sherpa_221_NNPDF30NNLO_ZqqZll	e5525_s2726_r7772_r7676	15.5630	1.00	0.140	2447.129
363359	Sherpa_221_NNPDF30NNLO_WpqqWmlv	e5583_s2726_r7772_r7676	24.7170	1.00	1.000	286.969
363358	Sherpa_221_NNPDF30NNLO_WqqZll	e5525_s2726_r7772_r7676	3.4370	1.00	1.000	1549.025
363360	Sherpa_221_NNPDF30NNLO_WplvWmq	e5983_s2726_r7772_r7676	112.7400	1.00	1.000	63.110
363489	Sherpa_221_NNPDF30NNLO_WlvZqq	e5525_s2726_r7772_r7676	11.4130	1.00	1.000	622.098
363490	Sherpa_221_NNPDF30NNLO_llll	e5332_s2726_r7772_r7676	1.2557	1.00	1.000	14195.509
363491	Sherpa_221_NNPDF30NNLO_lllv	e5332_s2726_r7772_r7676	4.5877	1.00	1.000	3437.907
363492	Sherpa_221_NNPDF30NNLO_llvv	e5332_s2726_r7772_r7676	12.4650	1.00	1.000	1187.565

Table A.1: List of simulated diboson processes

Dataset ID	Process	Tags	$\sigma \times \epsilon$ [pb]	k -factor	G. eff.	$\mathcal{L}_{int}[\text{fb}^{-1}]$
multitop						
304014	MadGraphPythia8EvtGen_A14NNPDF23_3top_SM	e4324_a766_a818_r7676	0.0016	1.00	1.000	121951.219
410080	MadGraphPythia8EvtGen_A14NNPDF23_4topSM	e4111_s2608_s2183_r7725_r7676	0.0092	1.00	1.000	21607.096
410000	PowhegPythiaEvtGen_ttbar_hdamp172p5_nonallhad	e3698_s2608_s2183_r7725_r7676	696.1100	1.19	0.543	109.345
triboson						
407311	Sherpa_221_NNPDF30NNLO_6l0v_EW6	e5473_s2726_r7772_r7676	0.0001	1.00	1.000	478749.375
407312	Sherpa_221_NNPDF30NNLO_5l1v_EW6	e5473_s2726_r7772_r7676	0.0006	1.00	1.000	88080.891
407313	Sherpa_221_NNPDF30NNLO_4l2v_EW6	e5473_s2726_r7772_r7676	0.0044	1.00	1.000	11216.921
407314	Sherpa_221_NNPDF30NNLO_3l3v_EW6	e5473_s2726_r7772_r7676	0.0158	1.00	1.000	3029.156
407315	Sherpa_221_NNPDF30NNLO_2l4v_EW6	e5655_s2726_r7772_r7676	0.0058	1.00	1.000	10108.625
Higgs related processes						
341079	PowhegPythia8EvtGen_CT10_ggH125_WWlvlv	e3871_s2608_s2183_r7772_r7676	0.9902	1.00	0.491	983.382
341122	PowhegPythia8EvtGen_CT10_ggH125_tautau	e3935_s2608_s2183_r7772_r7676	1.9081	1.45	0.123	4467.140
341195	PowhegPythia8EvtGen_CT10_ggH125_mumu	e3945_s2608_s2183_r7772_r7676	0.0066	1.45	1.000	99495.922
342178	PowhegPythia8EvtGen_CT10_ggH125_ee	e4158_s2608_r7772_r7676	0.0000	1.45	1.000	293359648.000
341080	PowhegPythia8EvtGen_CT10_VBFH125_WWlvlv	e3871_s2608_s2183_r7772_r7676	0.0848	1.00	0.510	5774.853
341155	PowhegPythia8EvtGen_CT10_VBFH125_tautau	e3888_s2608_s2183_r7772_r7676	0.2420	0.98	0.123	71518.055
341206	PowhegPythia8EvtGen_CT10_VBFH125_mumu	e3945_s2608_s2183_r7772_r7676	0.0009	0.96	1.000	998280.062
342189	PowhegPythia8EvtGen_CT10_VBFH125_ee	e4158_s2608_r7772_r7676	0.0000	0.98	1.000	5208568320.000
342284	Pythia8EvtGen_WH125_inc	e4246_s2608_s2183_r7772_r7676	1.1021	1.25	1.000	72.029
342285	Pythia8EvtGen_ZH125_inc	e4246_s2608_s2183_r7772_r7676	0.6007	1.45	1.000	114.075
341270	aMcAtNloHerwigppEvtGen_ttH125_semilep	e4277_s2608_s2183_r7772_r7676	0.5085	1.00	0.439	4269.874
341271	aMcAtNloHerwigppEvtGen_ttH125_allhad	e4277_s2608_s2183_r7772_r7676	0.5085	1.00	0.455	4112.265
341177	aMcAtNloHerwigppEvtGen_ttH125_dil	e4277_s2608_s2183_r7772_r7676	0.5085	1.00	0.106	35645.684

Table A.2: List of simulated Rare processes

Dataset ID	Process	Tags	$\sigma \times \epsilon$ [pb]	k -factor	G. eff.	$\mathcal{L}_{int}[\text{fb}^{-1}]$
410218	aMcAtNloPythia8EvtGen_A14N23LO_ttee	e5070_s2726_r7772_r7676	0.0369	1.12	1.000	34099.359
410219	aMcAtNloPythia8EvtGen_A14N23LO_ttmumu	e5070_s2726_r7772_r7676	0.0369	1.12	1.000	34112.250
410220	aMcAtNloPythia8EvtGen_A14N23LO_ttttau	e5070_s2726_r7772_r7676	0.0366	1.12	1.000	22792.877
410155	aMcAtNloPythia8EvtGen_A14N23LO_ttW	e5070_s2726_r7772_r7676	0.5483	1.10	1.000	12423.357
410081	MadGraphPythia8EvtGen_ttbarWW	e4111_s2608_s2183_r7725_r7676	0.0081	1.22	1.000	5048.439
407321	MadGraphPythia8EvtGen_ttbarWll	e5536_s2726_r7772_r7676	0.0003	1.34	1.000	84165.641

Table A.3: List of simulated $t\bar{t}$ plus vectorboson processes

DS ID	Process	Tags	$\sigma \times \epsilon$ [pb]	k -factor	G. ef.	$\mathcal{L}_{int}[\text{fb}^{-1}]$
410011	PowhegPythiaEvtGen_singletop_tchan_lept_top	e3824_s2608_s2183_r7725_r7676	43.7390	1.01	1.000	112.937
410012	PowhegPythiaEvtGen_singletop_tchan_lept_antitop	e3824_s2608_s2183_r7725_r7676	25.7780	1.02	1.000	189.903
410015	PowhegPythiaEvtGen_P2012_Wt_dilepton_top	e3753_s2608_s2183_r7725_r7676	3.5835	1.05	1.000	262.959
410016	PowhegPythiaEvtGen_Wt_dilepton_antitop	e3753_s2608_s2183_r7725_r7676	3.5814	1.05	1.000	262.690
410026	PowhegPythiaEvtGen_SingleTopSchan_noAllHad_antitop	e3998_s2608_s2183_r7725_r7676	1.2615	1.02	1.000	772.453
410025	PowhegPythiaEvtGen_SingleTopSchan_noAllHad_top	e3998_s2608_s2183_r7725_r7676	2.0517	1.00	1.000	484.101

Table A.4: List of simulated singletop processes

Dataset ID	Process	Tags	$\sigma \times \epsilon$ [pb]	k -factor	G. eff.	$\mathcal{L}_{int}[\text{fb}^{-1}]$
364198	Sherpa_221_Zmm_Mll10_40_MAXHTPTV0_70_BVeto	e5421_s2726_r7772_r7676	2413.7000	0.98	0.965	3.270
364199	Sherpa_221_Zmm_Mll10_40_MAXHTPTV0_70_BFilter	e5421_s2726_r7772_r7676	2414.7000	0.98	0.034	18.427
364200	Sherpa_221_Zmm_Mll10_40_MAXHTPTV70_280_BVeto	e5421_s2726_r7772_r7676	50.3180	0.98	0.892	54.088
364201	Sherpa_221_Zmm_Mll10_40_MAXHTPTV70_280_BFilter	e5421_s2726_r7772_r7676	50.2850	0.98	0.102	217.538
364202	Sherpa_221_Zmm_Mll10_40_MAXHTPTV280_E_CMS_BVeto	e5421_s2726_r7772_r7676	3.2355	0.98	0.853	220.507
364203	Sherpa_221_Zmm_Mll10_40_MAXHTPTV280_E_CMS_BFilter	e5421_s2726_r7772_r7676	3.2800	0.98	0.144	538.250
364204	Sherpa_221_Zee_Mll10_40_MAXHTPTV0_70_BVeto	e5421_s2726_r7772_r7676	2415.7000	0.98	0.965	3.253
364205	Sherpa_221_Zee_Mll10_40_MAXHTPTV0_70_BFilter	e5421_s2726_r7772_r7676	2416.8999	0.98	0.034	18.605
364206	Sherpa_221_Zee_Mll10_40_MAXHTPTV70_280_BVeto	e5421_s2726_r7772_r7676	50.4560	0.98	0.891	54.046
364207	Sherpa_221_Zee_Mll10_40_MAXHTPTV70_280_BFilter	e5421_s2726_r7772_r7676	50.4270	0.98	0.109	203.183
364208	Sherpa_221_Zee_Mll10_40_MAXHTPTV280_E_CMS_BVeto	e5421_s2726_r7772_r7676	3.2538	0.98	0.854	217.853
364209	Sherpa_221_Zee_Mll10_40_MAXHTPTV280_E_CMS_BFilter	e5421_s2726_r7772_r7676	3.2519	0.98	0.145	539.771
364210	Sherpa_221_Ztt_Mll10_40_MAXHTPTV0_70_BVeto	e5421_s2726_r7772_r7676	2417.8999	0.98	0.965	3.240
364211	Sherpa_221_Ztt_Mll10_40_MAXHTPTV0_70_BFilter	e5421_s2726_r7772_r7676	2414.2000	0.98	0.034	18.720
364212	Sherpa_221_Ztt_Mll10_40_MAXHTPTV70_280_BVeto	e5421_s2726_r7772_r7676	50.3700	0.98	0.890	54.057
364213	Sherpa_221_Ztt_Mll10_40_MAXHTPTV70_280_BFilter	e5421_s2726_r7772_r7676	50.4400	0.98	0.110	200.586
364214	Sherpa_221_Ztt_Mll10_40_MAXHTPTV280_E_CMS_BVeto	e5421_s2726_r7772_r7676	3.2834	0.98	0.851	217.328
364215	Sherpa_221_Ztt_Mll10_40_MAXHTPTV280_E_CMS_BFilter	e5421_s2726_r7772_r7676	3.2788	0.98	0.143	530.539

Table A.5: List of simulated DrellYan processes

Dataset ID	Process	Tags	$\sigma \times \epsilon$ [pb]	k -factor	G. eff.	$\mathcal{L}_{int}[\text{fb}^{-1}]$
301535	Sherpa_CT10_eegammaPt10_35	e3952_s2608_s2183_r7725_r7676	52.7060	1.00	1.000	94.596
301536	Sherpa_CT10_mumugammaPt10_35	e3952_s2608_s2183_r7773_r7676	52.7080	1.00	1.000	94.509
301890	Sherpa_CT10_enugammaPt35_70	e3952_s2608_s2183_r7725_r7676	15.3480	1.00	1.000	32.525
301891	Sherpa_CT10_enugammaPt70_140	e3952_s2608_s2183_r7725_r7676	1.5282	1.00	1.000	163.591
301892	Sherpa_CT10_enugammaPt140	e3952_s2608_s2183_r7725_r7676	0.2415	1.00	1.000	1034.154
301893	Sherpa_CT10_munugammaPt35_70	e3952_s2608_s2183_r7725_r7676	15.2720	1.00	1.000	32.674
301894	Sherpa_CT10_munugammaPt70_140	e3952_s2608_s2183_r7725_r7676	1.5235	1.00	1.000	163.702
301895	Sherpa_CT10_munugammaPt140	e3952_s2608_s2183_r7725_r7676	0.2418	1.00	1.000	1031.303
301896	Sherpa_CT10_taubugammaPt35_70	e3952_s2608_s2183_r7725_r7676	15.2970	1.00	1.000	32.568
301897	Sherpa_CT10_taubugammaPt70_140	e3952_s2608_s2183_r7725_r7676	1.5290	1.00	1.000	163.244
301898	Sherpa_CT10_taubugammaPt140	e3952_s2608_s2183_r7725_r7676	0.2426	1.00	1.000	1028.854
301899	Sherpa_CT10_eegammaPt35_70	e3952_s2608_s2183_r7725_r7676	5.2420	1.00	1.000	95.383
301900	Sherpa_CT10_eegammaPt70_140	e3952_s2608_s2183_r7725_r7676	0.3846	1.00	1.000	640.749
301901	Sherpa_CT10_eegammaPt140	e3952_s2608_s2183_r7725_r7676	0.0472	1.00	1.000	5295.601
301902	Sherpa_CT10_mumugammaPt35_70	e3952_s2608_s2183_r7725_r7676	5.2455	1.00	1.000	95.053
301903	Sherpa_CT10_mumugammaPt70_140	e3952_s2608_s2183_r7725_r7676	0.3855	1.00	1.000	648.023
301904	Sherpa_CT10_mumugammaPt140	e3952_s2608_s2183_r7725_r7676	0.0472	1.00	1.000	5275.190
301905	Sherpa_CT10_taubugammaPt35_70	e3952_s2608_s2183_r7725_r7676	5.2490	1.00	1.000	95.066
301906	Sherpa_CT10_taubugammaPt70_140	e3952_s2608_s2183_r7725_r7676	0.3848	1.00	1.000	649.135
301907	Sherpa_CT10_taubugammaPt140	e3952_s2608_s2183_r7725_r7676	0.0470	1.00	1.000	5295.056

Table A.6: List of simulated Vgamma processes

Dataset ID	Process	Tags	$\sigma \times \epsilon$ [pb]	k -factor	G. eff.	\mathcal{L}_{int} [fb ⁻¹]
364100	Sherpa_221_Zmumu_MAXHTPTV0.70_CVetoBVeto	e5271_s2726_r7772_r7676	1983.0000	0.98	0.822	4.964
364101	Sherpa_221_Zmumu_MAXHTPTV0.70_CFilterBVeto	e5271_s2726_r7772_r7676	1978.4000	0.98	0.113	22.540
364102	Sherpa_221_Zmumu_MAXHTPTV0.70_BFilter	e5271_s2726_r7772_r7676	1982.2000	0.98	0.064	63.719
364103	Sherpa_221_Zmumu_MAXHTPTV70.140_CVetoBVeto	e5271_s2726_r7772_r7676	108.9200	0.98	0.689	80.890
364104	Sherpa_221_Zmumu_MAXHTPTV70.140_CFilterBVeto	e5271_s2726_r7772_r7676	109.4200	0.98	0.186	99.279
364105	Sherpa_221_Zmumu_MAXHTPTV70.140_BFilter	e5271_s2726_r7772_r7676	108.9100	0.98	0.114	488.459
364106	Sherpa_221_Zmumu_MAXHTPTV140.280_CVetoBVeto	e5271_s2726_r7772_r7676	39.8780	0.98	0.609	208.736
364107	Sherpa_221_Zmumu_MAXHTPTV140.280_CFilterBVeto	e5271_s2726_r7772_r7676	39.7950	0.98	0.233	326.653
364108	Sherpa_221_Zmumu_MAXHTPTV140.280_BFilter	e5271_s2726_r7772_r7676	39.9080	0.98	0.146	2169.169
364109	Sherpa_221_Zmumu_MAXHTPTV280.500_CVetoBVeto	e5271_s2726_r7772_r7676	8.5375	0.98	0.559	423.925
364110	Sherpa_221_Zmumu_MAXHTPTV280.500_CFilterBVeto	e5271_s2726_r7772_r7676	8.5403	0.98	0.265	446.324
364111	Sherpa_221_Zmumu_MAXHTPTV280.500_BFilter	e5271_s2726_r7772_r7676	8.4932	0.98	0.176	1355.672
364112	Sherpa_221_Zmumu_MAXHTPTV500.1000	e5271_s2726_r7772_r7676	1.7881	0.98	1.000	1697.947
364113	Sherpa_221_Zmumu_MAXHTPTV1000_E.CMS	e5271_s2726_r7772_r7676	0.1477	0.98	1.000	6860.515
364114	Sherpa_221_Zee_MAXHTPTV0.70_CVetoBVeto	e5299_s2726_r7772_r7676	1981.8000	0.98	0.821	4.979
364115	Sherpa_221_Zee_MAXHTPTV0.70_CFilterBVeto	e5299_s2726_r7772_r7676	1980.8000	0.98	0.113	22.646
364116	Sherpa_221_Zee_MAXHTPTV0.70_BFilter	e5299_s2726_r7772_r7676	1981.7000	0.98	0.064	63.937
364117	Sherpa_221_Zee_MAXHTPTV70.140_CVetoBVeto	e5299_s2726_r7772_r7676	110.5000	0.98	0.690	79.645
364118	Sherpa_221_Zee_MAXHTPTV70.140_CFilterBVeto	e5299_s2726_r7772_r7676	110.6300	0.98	0.184	99.477
364119	Sherpa_221_Zee_MAXHTPTV70.140_BFilter	e5299_s2726_r7772_r7676	110.3100	0.98	0.114	475.689
364120	Sherpa_221_Zee_MAXHTPTV140.280_CVetoBVeto	e5299_s2726_r7772_r7676	40.7310	0.98	0.615	202.772
364121	Sherpa_221_Zee_MAXHTPTV140.280_CFilterBVeto	e5299_s2726_r7772_r7676	40.6700	0.98	0.230	324.184
364122	Sherpa_221_Zee_MAXHTPTV140.280_BFilter	e5299_s2726_r7772_r7676	40.6430	0.98	0.150	2078.998
364123	Sherpa_221_Zee_MAXHTPTV280.500_CVetoBVeto	e5299_s2726_r7772_r7676	8.6743	0.98	0.561	407.078
364124	Sherpa_221_Zee_MAXHTPTV280.500_CFilterBVeto	e5299_s2726_r7772_r7676	8.6711	0.98	0.263	444.808
364125	Sherpa_221_Zee_MAXHTPTV280.500_BFilter	e5299_s2726_r7772_r7676	8.6766	0.98	0.172	1356.645
364126	Sherpa_221_Zee_MAXHTPTV500.1000	e5299_s2726_r7772_r7676	1.8081	0.98	1.000	1686.255
364127	Sherpa_221_Zee_MAXHTPTV1000_E.CMS	e5299_s2726_r7772_r7676	0.1486	0.98	1.000	6819.879
364128	Sherpa_221_Ztautau_MAXHTPTV0.70_CVetoBVeto	e5307_s2726_r7772_r7676	1981.6000	0.98	0.821	4.982
364129	Sherpa_221_Ztautau_MAXHTPTV0.70_CFilterBVeto	e5307_s2726_r7772_r7676	1978.8000	0.98	0.113	22.633
364130	Sherpa_221_Ztautau_MAXHTPTV0.70_BFilter	e5307_s2726_r7772_r7676	1981.8000	0.98	0.064	63.352
364131	Sherpa_221_Ztautau_MAXHTPTV70.140_CVetoBVeto	e5307_s2726_r7772_r7676	110.3700	0.98	0.689	80.065
364132	Sherpa_221_Ztautau_MAXHTPTV70.140_CFilterBVeto	e5307_s2726_r7772_r7676	110.5100	0.98	0.183	99.508
364133	Sherpa_221_Ztautau_MAXHTPTV70.140_BFilter	e5307_s2726_r7772_r7676	110.8700	0.98	0.111	493.213
364134	Sherpa_221_Ztautau_MAXHTPTV140.280_CVetoBVeto	e5307_s2726_r7772_r7676	40.7810	0.98	0.608	204.914
364135	Sherpa_221_Ztautau_MAXHTPTV140.280_CFilterBVeto	e5307_s2726_r7772_r7676	40.7400	0.98	0.229	326.848
364136	Sherpa_221_Ztautau_MAXHTPTV140.280_BFilter	e5307_s2726_r7772_r7676	40.7610	0.98	0.134	923.313
364137	Sherpa_221_Ztautau_MAXHTPTV280.500_CVetoBVeto	e5307_s2726_r7772_r7676	8.5502	0.98	0.560	422.313
364138	Sherpa_221_Ztautau_MAXHTPTV280.500_CFilterBVeto	e5313_s2726_r7772_r7676	8.6707	0.98	0.262	444.352
364139	Sherpa_221_Ztautau_MAXHTPTV280.500_BFilter	e5313_s2726_r7772_r7676	8.6804	0.98	0.173	1347.705
364140	Sherpa_221_Ztautau_MAXHTPTV500.1000	e5307_s2726_r7772_r7676	1.8096	0.98	1.000	1668.876
364141	Sherpa_221_Ztautau_MAXHTPTV1000_E.CMS	e5307_s2726_r7772_r7676	0.1483	0.98	1.000	6775.146

Table A.7: List of simulated Z+jets processes

DS ID	Process	Tags	$\sigma \times \epsilon$ [pb]	k -factor	G. eff.	$\mathcal{L}_{int}[\text{fb}^{-1}]$
364156	Sherpa_221.Wmunu.MAXHTPTV0.70.CVetoBVeto	e5340.s2726.r7772.r7676	19143.0000	0.97	0.824	1.616
364157	Sherpa_221.Wmunu.MAXHTPTV0.70.CFilterBVeto	e5340.s2726.r7772.r7676	19121.0000	0.97	0.130	4.071
364158	Sherpa_221.Wmunu.MAXHTPTV0.70.BFilter	e5340.s2726.r7772.r7676	19135.0000	0.97	0.044	21.032
364159	Sherpa_221.Wmunu.MAXHTPTV70.140.CVetoBVeto	e5340.s2726.r7772.r7676	944.8500	0.97	0.675	23.912
364160	Sherpa_221.Wmunu.MAXHTPTV70.140.CFilterBVeto	e5340.s2726.r7772.r7676	937.7800	0.97	0.235	46.173
364161	Sherpa_221.Wmunu.MAXHTPTV70.140.BFilter	e5340.s2726.r7772.r7676	944.6300	0.97	0.076	283.269
364162	Sherpa_221.Wmunu.MAXHTPTV140.280.CVetoBVeto	e5340.s2726.r7772.r7676	339.5400	0.97	0.626	47.919
364163	Sherpa_221.Wmunu.MAXHTPTV140.280.CFilterBVeto	e5340.s2726.r7772.r7676	340.0600	0.97	0.289	77.568
364164	Sherpa_221.Wmunu.MAXHTPTV140.280.BFilter	e5340.s2726.r7772.r7676	339.5400	0.97	0.109	686.449
364165	Sherpa_221.Wmunu.MAXHTPTV280.500.CVetoBVeto	e5340.s2726.r7772.r7676	72.0670	0.97	0.546	129.289
364166	Sherpa_221.Wmunu.MAXHTPTV280.500.CFilterBVeto	e5340.s2726.r7772.r7676	72.1980	0.97	0.317	133.034
364167	Sherpa_221.Wmunu.MAXHTPTV280.500.BFilter	e5340.s2726.r7772.r7676	72.0450	0.97	0.133	317.464
364168	Sherpa_221.Wmunu.MAXHTPTV500.1000	e5340.s2726.r7772.r7676	15.0100	0.97	1.000	405.866
364169	Sherpa_221.Wmunu.MAXHTPTV1000.E.CMS	e5340.s2726.r7772.r7676	1.2344	0.97	1.000	3305.737
364170	Sherpa_221.Wenu.MAXHTPTV0.70.CVetoBVeto	e5340.s2726.r7772.r7676	19127.0000	0.97	0.824	1.617
364171	Sherpa_221.Wenu.MAXHTPTV0.70.CFilterBVeto	e5340.s2726.r7772.r7676	19130.0000	0.97	0.130	4.074
364172	Sherpa_221.Wenu.MAXHTPTV0.70.BFilter	e5340.s2726.r7772.r7676	19135.0000	0.97	0.044	20.272
364173	Sherpa_221.Wenu.MAXHTPTV70.140.CVetoBVeto	e5340.s2726.r7772.r7676	942.5800	0.97	0.669	23.973
364174	Sherpa_221.Wenu.MAXHTPTV70.140.CFilterBVeto	e5340.s2726.r7772.r7676	945.6700	0.97	0.228	46.963
364175	Sherpa_221.Wenu.MAXHTPTV70.140.BFilter	e5340.s2726.r7772.r7676	945.1500	0.97	0.103	103.368
364176	Sherpa_221.Wenu.MAXHTPTV140.280.CVetoBVeto	e5340.s2726.r7772.r7676	339.8100	0.97	0.597	50.200
364177	Sherpa_221.Wenu.MAXHTPTV140.280.CFilterBVeto	e5340.s2726.r7772.r7676	339.8700	0.97	0.290	77.584
364178	Sherpa_221.Wenu.MAXHTPTV140.280.BFilter	e5340.s2726.r7772.r7676	339.4800	0.97	0.109	687.518
364179	Sherpa_221.Wenu.MAXHTPTV280.500.CVetoBVeto	e5340.s2726.r7772.r7676	72.0840	0.97	0.544	129.323
364180	Sherpa_221.Wenu.MAXHTPTV280.500.CFilterBVeto	e5340.s2726.r7772.r7676	72.1280	0.97	0.317	133.693
364181	Sherpa_221.Wenu.MAXHTPTV280.500.BFilter	e5340.s2726.r7772.r7676	72.1130	0.97	0.134	315.726
364182	Sherpa_221.Wenu.MAXHTPTV500.1000	e5340.s2726.r7772.r7676	15.2240	0.97	1.000	400.587
364183	Sherpa_221.Wenu.MAXHTPTV1000.E.CMS	e5340.s2726.r7772.r7676	1.2334	0.97	1.000	3298.389
364184	Sherpa_221.Wtaunu.MAXHTPTV0.70.CVetoBVeto	e5340.s2726.r7772.r7676	19152.0000	0.97	0.825	1.617
364185	Sherpa_221.Wtaunu.MAXHTPTV0.70.CFilterBVeto	e5340.s2726.r7772.r7676	19153.0000	0.97	0.129	4.105
364186	Sherpa_221.Wtaunu.MAXHTPTV0.70.BFilter	e5340.s2726.r7772.r7676	19163.0000	0.97	0.045	20.834
364187	Sherpa_221.Wtaunu.MAXHTPTV70.140.CVetoBVeto	e5340.s2726.r7772.r7676	947.6500	0.97	0.674	23.903
364188	Sherpa_221.Wtaunu.MAXHTPTV70.140.CFilterBVeto	e5340.s2726.r7772.r7676	946.7300	0.97	0.222	48.307
364189	Sherpa_221.Wtaunu.MAXHTPTV70.140.BFilter	e5340.s2726.r7772.r7676	943.3000	0.97	0.104	103.602
364190	Sherpa_221.Wtaunu.MAXHTPTV140.280.CVetoBVeto	e5340.s2726.r7772.r7676	339.3600	0.97	0.596	50.427
364191	Sherpa_221.Wtaunu.MAXHTPTV140.280.CFilterBVeto	e5340.s2726.r7772.r7676	339.6300	0.97	0.290	76.903
364192	Sherpa_221.Wtaunu.MAXHTPTV140.280.BFilter	e5340.s2726.r7772.r7676	339.5400	0.97	0.118	632.798
364193	Sherpa_221.Wtaunu.MAXHTPTV280.500.CVetoBVeto	e5340.s2726.r7772.r7676	72.0650	0.92	0.546	136.270
364194	Sherpa_221.Wtaunu.MAXHTPTV280.500.CFilterBVeto	e5340.s2726.r7772.r7676	71.9760	0.97	0.316	133.773
364195	Sherpa_221.Wtaunu.MAXHTPTV280.500.BFilter	e5340.s2726.r7772.r7676	72.0260	0.97	0.134	314.868
364196	Sherpa_221.Wtaunu.MAXHTPTV500.1000	e5340.s2726.r7772.r7676	15.0460	0.97	1.000	407.258
364197	Sherpa_221.Wtaunu.MAXHTPTV1000.E.CMS	e5340.s2726.r7772.r7676	1.2339	0.97	1.000	3296.218

Table A.8: List of simulated W+jets processes

A.3 Data to MC comparisons for the proposed validation regions

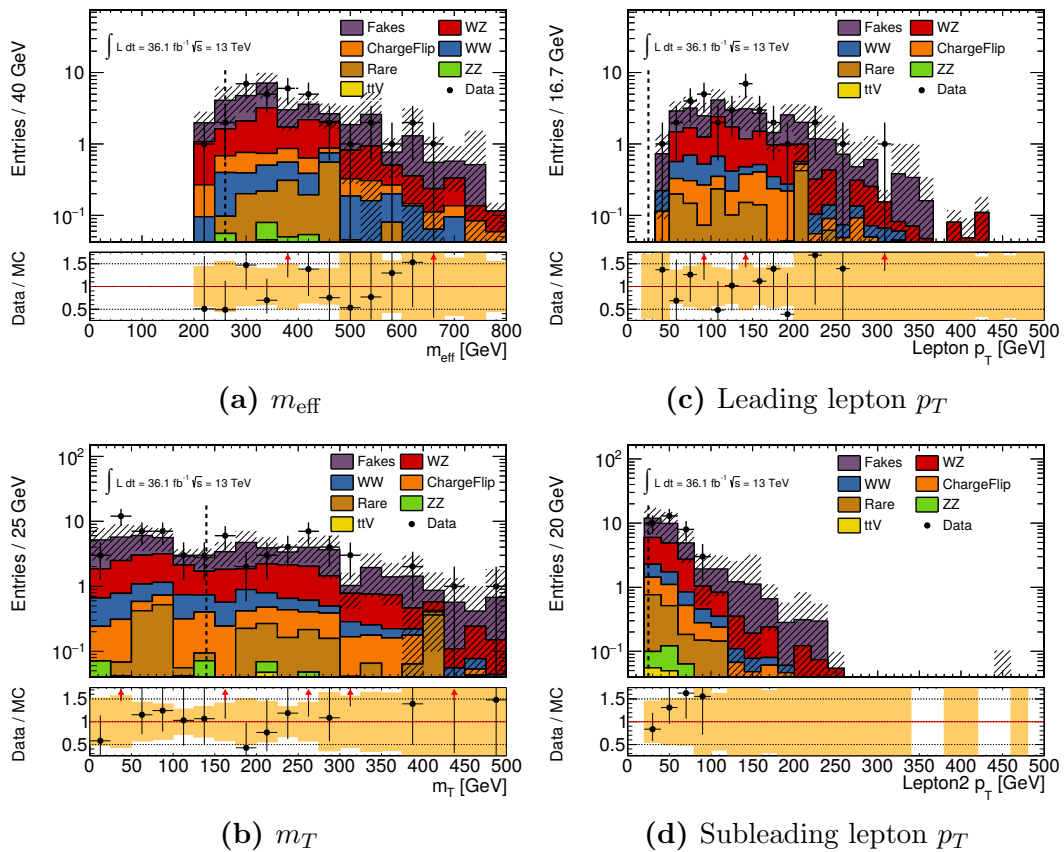


Figure A.2: Comparison of Data with Monte Carlo in VRjet1. The error bands include experimental and statistical uncertainties. All VR cuts but the respective variable shown are applied

A.3 Data to MC comparisons for the proposed validation regions

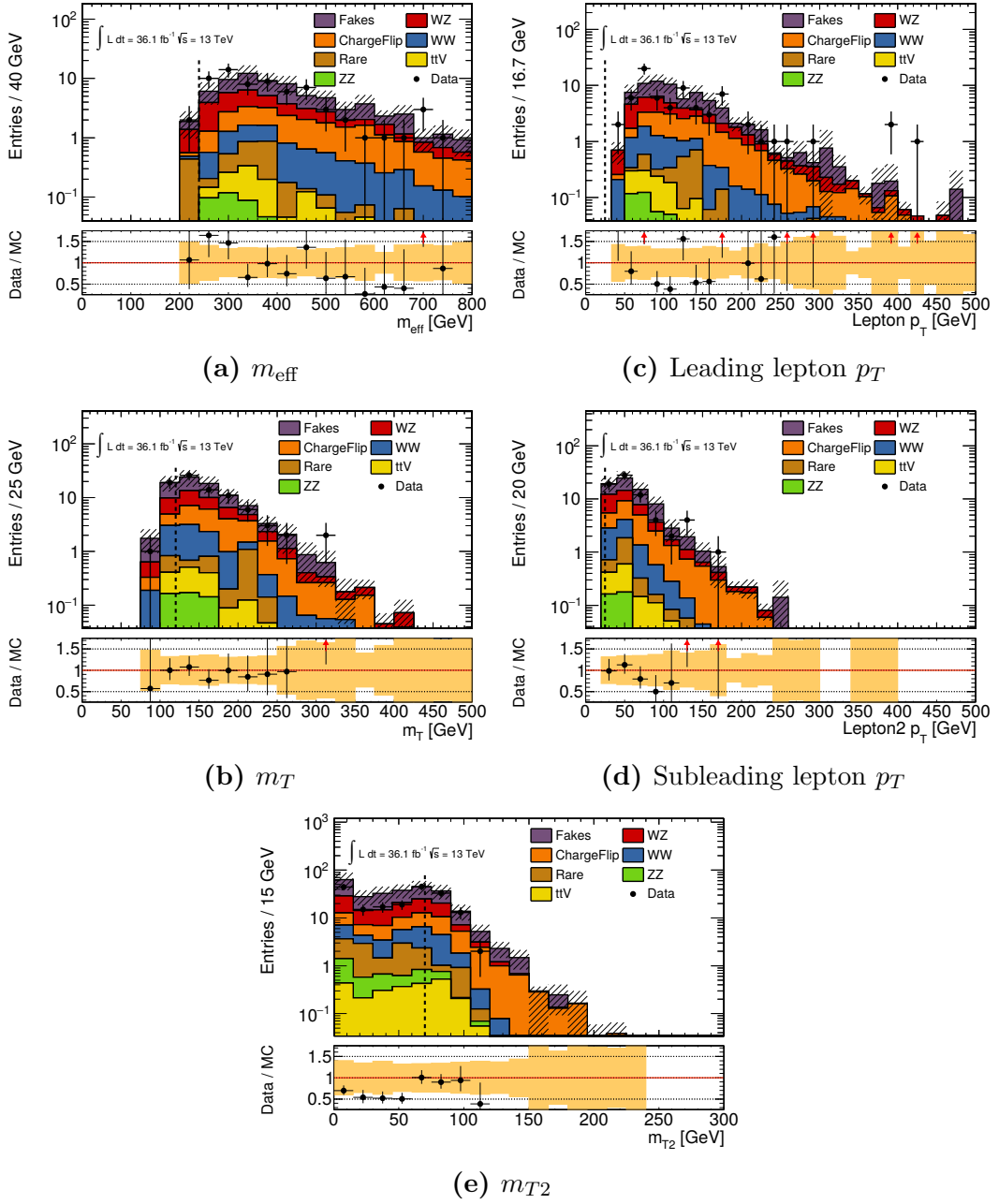


Figure A.3: Comparison of Data with Monte Carlo in VRjet23. The error bands include experimental and statistical uncertainties. All VR cuts but the respective variable shown are applied

Bibliography

- [1] **ATLAS** Collaboration, G. Aad *et al.*, “Observation of a new particle in the search for the Standard Model Higgs boson with the ATLAS detector at the LHC,” *Phys. Lett.* **B716** (2012) 1–29, [arXiv:1207.7214 \[hep-ex\]](#).
- [2] **CMS** Collaboration, S. Chatrchyan *et al.*, “Observation of a new boson at a mass of 125 GeV with the CMS experiment at the LHC,” *Phys. Lett.* **B716** (2012) 30–61, [arXiv:1207.7235 \[hep-ex\]](#).
- [3] S. P. Martin, “A Supersymmetry Primer,” *Adv.Ser.Direct.High Energy Phys.* **18** (Jul, 1997) 1–98, [arXiv/hep-ph:9709356 \[hep-ph\]](#).
- [4] D. Griffiths, *Introduction to elementary particles*. 2008.
- [5] M. E. Peskin and D. V. Schroeder, *An Introduction to quantum field theory*. Addison-Wesley, Reading, USA, 1995.
<http://www.slac.stanford.edu/~mpeskin/QFT.html>.
- [6] I. J. R. Aitchison and A. J. G. Hey, *Gauge theories in particle physics: A practical introduction. Vol. 1: From relativistic quantum mechanics to QED*. CRC Press, Bristol, UK, 2012. <http://www-spires.fnal.gov/spires/find/books/www?cl=QC793.3.F5A34::2012>.
- [7] I. J. R. Aitchison and A. J. G. Hey, *Gauge theories in particle physics: A practical introduction. Vol. 2: Non-Abelian gauge theories: QCD and the electroweak theory*. CRC Press, Bristol, UK, 2012.
<http://www-spires.fnal.gov/spires/find/books/www?cl=QC793.3.F5A34::2012:V2>.
- [8] “Advanced particle physics lecture notes,” 2016. Prof. Dr. D. Schaile.
- [9] L. Senatore, “[Lectures on Inflation](#),” in *Proceedings, Theoretical Advanced Study Institute in Elementary Particle Physics: New Frontiers in Fields and Strings (TASI 2015): Boulder, CO, USA, June 1-26, 2015*, pp. 447–543. 2017.
[arXiv:1609.00716 \[hep-th\]](#).
<http://inspirehep.net/record/1485069/files/arXiv:1609.00716.pdf>.
- [10] **Particle Data Group** Collaboration, C. Patrignani *et al.*, “Review of Particle Physics,” *Chin. Phys.* **C40** no. 10, (2016) 100001.

- [11] P. Mission, “Planck mission - cosmic microwave background,” March, 2013. <http://planck.cf.ac.uk/results/cosmic-microwave-background>. accessed 14.04.18.
- [12] F. Zwicky, “On the Masses of Nebulae and of Clusters of Nebulae,” *APJ* **86** (Oct., 1937) 217.
- [13] D. Clowe, M. Bradac, A. H. Gonzalez, M. Markevitch, S. W. Randall, C. Jones, and D. Zaritsky, “A direct empirical proof of the existence of dark matter,” [arXiv:0608407](https://arxiv.org/abs/astro-ph/0608407) [astro-ph]. <http://arxiv.org/abs/astro-ph/0608407>.
- [14] D. Harvey, R. Massey, T. Kitching, A. Taylor, and E. Tittley, “The non-gravitational interactions of dark matter in colliding galaxy clusters,” [arXiv \[astro-ph\]:1503.07675](https://arxiv.org/abs/astro-ph/1503.07675). <http://arxiv.org/abs/1503.07675>.
- [15] P. Binétruy, *Supersymmetry: theory, experiment and cosmology*. 2006. <http://inspirehep.net/record/736775/?ln=de>.
- [16] C. Csáki and P. Tanedo, “Beyond the Standard Model,” [arXiv:1602.04228](https://arxiv.org/abs/1602.04228).
- [17] R. Catena and L. Covi, “SUSY dark matter(s) Review,” in *Supersymmetry After Higgs Discov.*, pp. 121–136. Oct, 2014. [arXiv:1310.4776](https://arxiv.org/abs/1310.4776).
- [18] **LHC New Physics Working Group** Collaboration, D. Alves, “Simplified Models for LHC New Physics Searches,” *J. Phys.* **G39** (2012) 105005, [arXiv:1105.2838](https://arxiv.org/abs/1105.2838) [hep-ph].
- [19] A. Cervelli, G. Gallardo, J. Lorenz, D. M. Koeck, D. Paredes Hernandez, P. Tornambe, M. Javurkova, Y. Tu, D. Zhang, and C. Y. Lo, “Search for chargino and neutralino production in final states with two same-sign leptons, jets and missing transverse momentum at $\sqrt{s} = 13$ TeV with the ATLAS detector,” Dec, 2017. <https://cds.cern.ch/record/2298595>. ATLAS Internal documentation.
- [20] M. Ibe, S. Matsumoto, and R. Sato, “Mass Splitting between Charged and Neutral Winos at Two-Loop Level,” *Phys. Lett.* **B721** (2013) 252–260, [arXiv:1212.5989](https://arxiv.org/abs/1212.5989) [hep-ph].
- [21] **ATLAS** Collaboration, G. Aad *et al.*, “Summary of the ATLAS experiments sensitivity to supersymmetry after LHC Run 1 interpreted in the phenomenological MSSM,” *JHEP* **10** (2015) 134, [arXiv:1508.06608](https://arxiv.org/abs/1508.06608) [hep-ex].
- [22] **ATLAS** Collaboration, G. Aad *et al.*, “Search for direct pair production of a chargino and a neutralino decaying to the 125 GeV Higgs boson in $\sqrt{s} = 8$ TeV pp collisions with the ATLAS detector,” *Eur. Phys. J.* **C75** no. 5, (2015) 208, [arXiv:1501.07110](https://arxiv.org/abs/1501.07110) [hep-ex].

-
- [23] **ATLAS** Collaboration, “Summary plots from the atlas supersymmetry physics group,” 03, 2018. https://atlas.web.cern.ch/Atlas/GROUPS/PHYSICS/CombinedSummaryPlots/SUSY/ATLAS_SUSY_EWSummary/ATLAS_SUSY_EWSummary.png.
- [24] CERN, “About cern,” 2018. <https://home.cern/about>. accessed 09.04.18.
- [25] “LHC Guide.” Mar, 2017.
- [26] CERN, “The accelerator complex,” 2018. <https://home.cern/about/accelerators>.
- [27] E. A. Mobs, “The CERN accelerator complex. Complexe des accrateurs du CERN,”. <https://cds.cern.ch/record/2225847>.
- [28] **ATLAS** Collaboration, G. Aad *et al.*, “The ATLAS Experiment at the CERN Large Hadron Collider,” *JINST* **3** (2008) S08003.
- [29] J. Pequeno, “Computer generated image of the whole ATLAS detector.” Mar, 2008.
- [30] **ATLAS** Collaboration, M. Capeans, G. Darbo, K. Einsweiler, M. Elsing, T. Flick, M. Garcia-Sciveres, C. Gemme, H. Pernegger, O. Rohne, and R. Vuillermet, “ATLAS Insertable B-Layer Technical Design Report,” Sep, 2010. <http://cds.cern.ch/record/1291633>.
- [31] A. La Rosa, “The ATLAS Insertable B-Layer: from construction to operation,” *JINST* **11** no. 12, (2016) C12036, [arXiv:1610.01994](https://arxiv.org/abs/1610.01994).
- [32] W. Demtroeder, *Experimental physics. Vol. 4: Nuclear, particle and astrophysics*. 1998.
- [33] **ATLAS** Collaboration, A. Ruiz-Martinez and A. Collaboration, “The Run-2 ATLAS Trigger System,” Tech. Rep. ATL-DAQ-PROC-2016-003, CERN, Geneva, Feb, 2016. <https://cds.cern.ch/record/2133909>.
- [34] **ATLAS** Collaboration, J. Pequeno and P. Schaffner, “An computer generated image representing how ATLAS detects particles.” Jan, 2013.
- [35] W. Herr and B. Muratori, “Concept of luminosity,”. <https://cds.cern.ch/record/941318>.
- [36] **ATLAS** Collaboration, “Peak luminosity per fill in 2015,” 2015. https://twiki.cern.ch/twiki/bin/view/AtlasPublic/LuminosityPublicResultsRun2#Luminosity_summary_plots_for_AN1.
- [37] **ATLAS** Collaboration, “Peak luminosity per fill in 2016,” 2016. https://twiki.cern.ch/twiki/bin/view/AtlasPublic/LuminosityPublicResultsRun2#Luminosity_summary_plots_for_AN1.

- [38] M. H. Seymour and M. Marx, “Monte Carlo Event Generators,” in *Proceedings, 69th Scottish Universities Summer School in Physics : LHC Phenomenology (SUSSP69): St. Andrews, Scotland, August 19-September 1, 2012*, pp. 287–319. 2013. [arXiv:1304.6677 \[hep-ph\]](https://arxiv.org/abs/1304.6677).
<http://inspirehep.net/record/1229804/files/arXiv:1304.6677.pdf>.
- [39] **GEANT4** Collaboration, S. Agostinelli *et al.*, “GEANT4: A Simulation toolkit,” *Nucl. Instrum. Meth. A* **506** (2003) 250.
- [40] **ATLAS** Collaboration, , “The ATLAS Simulation Infrastructure,” *Eur. Phys. J.* **C70** (2010) 823–874, [arXiv:1005.4568](https://arxiv.org/abs/1005.4568).
- [41] A. Collaboration, “Selection of jets produced in 13 TeV proton-proton collisions with the ATLAS detector,” May, 2015. <https://cds.cern.ch/record/2016323>.
- [42] Hryn’ova, T and Nagano, K, “Trigger Menu Strategy for Run 2,” May, 2014. <https://cds.cern.ch/record/1703730>.
- [43] A. E. C. group, “2016 trigger recommendations for analysis groups,” 2018. <https://twiki.cern.ch/twiki/bin/viewauth/Atlas/TriggerRecommendationsForAnalysisGroups>. ATLAS Internal documentation.
- [44] A. M. C. group, “MCPAnalysisGuidelinesMC15,” 2018. https://twiki.cern.ch/twiki/bin/view/AtlasProtected/MCPAnalysisGuidelinesMC15#Muon_triggers. ATLAS Internal documentation.
- [45] J. Maurer, “TrigGlobalEfficiencyCorrectionTool,” 2017. <https://twiki.cern.ch/twiki/bin/view/Sandbox/JulienMaurerSandbox>. ATLAS Internal documentation.
- [46] “Electron identification measurements in ATLAS using $\sqrt{s} = 13$ TeV data with 50 ns bunch spacing,” Sep, 2015. <https://cds.cern.ch/record/2048202>.
- [47] **ATLAS** Collaboration, “Electron charge id selector tool,” 2017. <https://twiki.cern.ch/twiki/bin/viewauth/AtlasProtected/ElectronChargeFlipTaggerTool>. ATLAS Internal documentation.
- [48] De Vivie De Regie, Jean-Baptiste and Guo, Jun and Kondrashova, Nataliia and Laplace, Sandrine and Lee, Graham Richard and Lesage, Arthur and Liu, Jianbei and Mazza, Simone Michele and Morris, John and Nicolaidou, Rosy and Poveda, Joaquin and Proklova, Nadezda and Shen, Yu-Ting and Vasquez, Jared Gregory and Wang, Zirui and Yang, Haijun and Zgubic, Miha and Zhang, Dongliang and Zhang, Liqing, “ATLAS electron, photon and muon isolation in Run 2,” Mar, 2017. <https://cds.cern.ch/record/2256658>. ATLAS Internal documentation.
- [49] **ATLAS** Collaboration, G. Aad *et al.*, “Muon reconstruction performance of the ATLAS detector in protonproton collision data at $\sqrt{s} = 13$ TeV,” *Eur. Phys. J.* **C76** no. 5, (2016) 292, [arXiv:1603.05598 \[hep-ex\]](https://arxiv.org/abs/1603.05598).

-
- [50] M. Cacciari, G. P. Salam, and G. Soyez, “The Anti-k(t) jet clustering algorithm,” *JHEP* **04** (2008) 063, [arXiv:0802.1189 \[hep-ph\]](#).
- [51] “Tagging and suppression of pileup jets with the ATLAS detector,” May, 2014. <https://cds.cern.ch/record/1700870>.
- [52] “Jet Calibration and Systematic Uncertainties for Jets Reconstructed in the ATLAS Detector at $\sqrt{s} = 13$ TeV,” Jul, 2015. <https://cds.cern.ch/record/2037613>.
- [53] **ATLAS Collaboration** Collaboration, “Optimisation of the ATLAS b -tagging performance for the 2016 LHC Run,” Jun, 2016. <https://cds.cern.ch/record/2160731>.
- [54] **ATLAS Collaboration**, M. Aaboud *et al.*, “Performance of missing transverse momentum reconstruction with the ATLAS detector using proton-proton collisions at $\sqrt{s} = 13$ TeV,” [arXiv:1802.08168 \[hep-ex\]](#).
- [55] **ATLAS Collaboration**, “Number of interactions per crossing,” 2017. https://twiki.cern.ch/twiki/bin/view/AtlasPublic/LuminosityPublicResultsRun2#Pileup_Interactions_and_Data_AN1. accessed 06.04.18.
- [56] **ATLAS Collaboration**, “MCTruthClassifier,” 2016. <https://twiki.cern.ch/twiki/bin/view/AtlasProtected/MCTruthClassifier>. ATLAS Internal documentation.
- [57] D. Bogavac, A. Cervelli, J. Lorenz, M. D’Onofrio, Y. Gao, M. J. Sullivan, R. El Kosseifi, and S. Muanza, “Search for chargino and neutralino production in final state with one lepton, two b-jets consistent with a Higgs boson, and missing transverse momentum at $\sqrt{s} = 13$ TeV with the ATLAS detector,” Apr, 2017. <https://cds.cern.ch/record/2259593>. ATLAS Internal documentation.
- [58] F. Alonso, O. Jinnouchi, R. Reece, B. Schumm, K. Todome, Y. Yamaguchi, and M. Gignac, “Search for direct pair production of a chargino and a neutralino decaying via photons to the 125 GeV Higgs boson in $\sqrt{s} = 13$ TeV pp collisions with the ATLAS detector,” Aug, 2017. <https://cds.cern.ch/record/2281410>. ATLAS Internal documentation.
- [59] De Santo, Antonella and Abraham, Nicola and Trovato, Fabrizio and Javurkova, Martina and Tornambe, Peter, “Search for electroweak supersymmetry in final states with three leptons and missing transverse momentum, via Wh intermediate decays, in 36.1 fb^{-1} of p-p collisions at 13 TeV with the ATLAS detector,” Oct, 2017. <https://cds.cern.ch/record/2289838>. ATLAS Internal documentation.

- [60] R. Camacho Toro, J. Olsson, D. Miller, G. Stark, M. Swiatlowski, and C. Rizzi, “Search for direct production of charginos and neutralinos with fully hadronic final states in pp collisions at 13 TeV with the ATLAS detector,” Sep, 2017. <https://cds.cern.ch/record/2282762>. ATLAS Internal documentation.
- [61] **ATLAS** Collaboration, “Lhc higgs cross section wg picture gallery,” 2016, accessed 31.03.18. https://twiki.cern.ch/twiki/bin/view/LHCPhysics/LHCHXSWGCrossSectionsFigures#Higgs_decay_width_and_branching.
- [62] B. Abbott, J.-F. Arguin, S. Berlendis, F. Cardillo, G. D. Carrillo-Montoya, A. Di Simone, O. A. Ducu, Z. D. Greenwood, G. Herten, D. Jana, S. Jin, Y. Liu, A. Lleres, J. Maurer, A. S. Mete, A. Paramonov, J. Poveda, P. Pralavorio, H. Ren, O. Rifki, C. Sandoval, Y.-T. Shen, P. Skubic, A. M. Soffa, A. Taffard, P. Tornambe, C. Walker, and X. Zhuang, “Search for supersymmetry in final states with two same-sign or three leptons and jets using $\sqrt{s} = 13$ TeV pp collision data collected with the ATLAS detector,” Feb, 2017. <https://cds.cern.ch/record/2252643>. ATLAS Internal documentation.
- [63] N. Hartmann, “Search for supersymmetry in events with an isolated lepton, at least 2-9 jets and missing transverse momentum with the atlas detector,” 2018. PhD thesis, To be published.
- [64] A. Barr, C. Lester, and P. Stephens, “m_T2 : the truth behind the glamour,” [arXiv:0304226 \[hep-ph\]](https://arxiv.org/abs/hep-ph/0304226). <http://arxiv.org/abs/hep-ph/0304226http://dx.doi.org/10.1088/0954-3899/29/10/304>.
- [65] N. Hartmann, “Arrgh - a roc reduction generator hack,” 2015, accessed 11.03.18. <https://gitlab.cern.ch/nihartma/arrgh>.
- [66] T. P. S. Gillam, *Identifying fake leptons in ATLAS while hunting SUSY in 8 TeV proton-proton collisions*. PhD thesis, Cambridge U., 2015. <https://www.repository.cam.ac.uk/handle/1810/247906>.
- [67] **ATLAS Collaboration** Collaboration, “Electron efficiency measurements with the ATLAS detector using the 2015 LHC proton-proton collision data,” Jun, 2016. <https://cds.cern.ch/record/2157687>.
- [68] **ATLAS Collaboration** Collaboration, “Electron and photon energy calibration with the ATLAS detector using data collected in 2015 at $\sqrt{s} = 13$ TeV,” Aug, 2016. <https://cds.cern.ch/record/2203514>.
- [69] **ATLAS** Collaboration, G. Aad *et al.*, “Jet energy resolution in proton-proton collisions at $\sqrt{s} = 7$ TeV recorded in 2010 with the ATLAS detector,” *Eur. Phys. J. C* **73** no. 3, (2013) 2306, [arXiv:1210.6210 \[hep-ex\]](https://arxiv.org/abs/1210.6210).

-
- [70] **ATLAS** Collaboration, G. Aad *et al.*, “Jet energy measurement and its systematic uncertainty in proton-proton collisions at $\sqrt{s} = 7$ TeV with the ATLAS detector,” *Eur. Phys. J.* **C75** (2015) 17, [arXiv:1406.0076 \[hep-ex\]](#).
- [71] **ATLAS** Collaboration, T. C. P. Group, “Track to vertex association,” 2015. https://twiki.cern.ch/twiki/bin/view/AtlasProtected/TrackingCPE0YE2015#Track_to_Vertex_Association. ATLAS Internal documentation.
- [72] **ATLAS** Collaboration, G. Aad *et al.*, “Performance of pile-up mitigation techniques for jets in pp collisions at $\sqrt{s} = 8$ TeV using the ATLAS detector,” *Eur. Phys. J.* **C76** no. 11, (2016) 581, [arXiv:1510.03823 \[hep-ex\]](#).
- [73] **ATLAS** Collaboration, “Physics modelling group (pmg),” 2018. <https://twiki.cern.ch/twiki/bin/view/AtlasProtected/PhysicsModellingGroup>. ATLAS Internal documentation.
- [74] **ATLAS** Collaboration, “Multiboson focus group - systematic uncertainties,” 2018. https://twiki.cern.ch/twiki/bin/view/AtlasProtected/MultibosonFocusGroup#Systematic_uncertainties. ATLAS Internal documentation.
- [75] **ATLAS** Collaboration, “Ttbar boson focus group - review of systematic uncertainties,” 2018. https://twiki.cern.ch/twiki/bin/view/AtlasProtected/TtbarBosonFocusGroup#Review_of_systematic_uncertainti. ATLAS Internal documentation.
- [76] “Multi-Boson Simulation for 13 TeV ATLAS Analyses,” Jan, 2016. <https://cds.cern.ch/record/2119986>.
- [77] G. Cowan, K. Cranmer, E. Gross, and O. Vitells, “Asymptotic formulae for likelihood-based tests of new physics,” *Eur. Phys. J.* **C71** (2011) 1554, [arXiv:1007.1727 \[physics.data-an\]](#). [Erratum: *Eur. Phys. J.* **C73**,2501(2013)].
- [78] M. Baak, G. J. Besjes, D. Cte, A. Koutsman, J. Lorenz, and D. Short, “HistFitter software framework for statistical data analysis,” *Eur. Phys. J.* **C75** (2015) 153, [arXiv:1410.1280 \[hep-ex\]](#).
- [79] J. Lorenz, “Search for strongly interacting supersymmetric particles decaying to final states with an isolated lepton with the ATLAS detector at the LHC,” 2014. https://www.etp.physik.uni-muenchen.de/publications/theses/download/phd_jlorenz.pdf.
- [80] A. L. Read, “Modified frequentist analysis of search results (The CL(s) method),” in *Workshop on confidence limits, CERN, Geneva, Switzerland, 17-18*

- Jan 2000: Proceedings*, pp. 81–101. 2000.
<http://weplib.cern.ch/abstract?CERN-OPEN-2000-205>.
- [81] L. Moneta, K. Belasco, K. S. Cranmer, S. Kreiss, A. Lazzaro, D. Piparo, G. Schott, W. Verkerke, and M. Wolf, “The RooStats Project,” *PoS ACAT2010* (2010) 057, [arXiv:1009.1003](https://arxiv.org/abs/1009.1003) [[physics.data-an](#)].
- [82] W. Verkerke and D. P. Kirkby, “The RooFit toolkit for data modeling,” *eConf C0303241* (2003) MOLT007, [arXiv:physics/0306116](https://arxiv.org/abs/physics/0306116) [[physics](#)].
[,186(2003)].
- [83] **ROOT** Collaboration, K. Cranmer, G. Lewis, L. Moneta, A. Shibata, and W. Verkerke, “HistFactory: A tool for creating statistical models for use with RooFit and RooStats,”.
- [84] **ATLAS** Collaboration, “Total integrated luminosity and data quality in 2015-2017,” 2018.
<https://atlas.web.cern.ch/Atlas/GROUPS/DATAPREPARATION/PublicPlots/2017/DataSummary/figs/intlumivstimeRun2DQ.png>. accessed 09.04.18.
- [85] T. Gleisberg, S. Hoeche, F. Krauss, M. Schonherr, S. Schumann, F. Siegert, and J. Winter, “Event generation with SHERPA 1.1,” *JHEP* **02** (2009) 007, [arXiv:0811.4622](https://arxiv.org/abs/0811.4622) [[hep-ph](#)].
- [86] S. Catani, L. Cieri, G. Ferrera, D. de Florian, and M. Grazzini, “Vector boson production at hadron colliders: a fully exclusive QCD calculation at NNLO,” *Phys. Rev. Lett.* **103** (2009) 082001, [arXiv:0903.2120](https://arxiv.org/abs/0903.2120) [[hep-ph](#)].
- [87] S. Alioli, P. Nason, C. Oleari, and E. Re, “A general framework for implementing NLO calculations in shower Monte Carlo programs: the POWHEG BOX,” *JHEP* **06** (2010) 043, [arXiv:1002.2581](https://arxiv.org/abs/1002.2581) [[hep-ph](#)].
- [88] J. Pumplin, D. R. Stump, J. Huston, H. L. Lai, P. M. Nadolsky, and W. K. Tung, “New generation of parton distributions with uncertainties from global QCD analysis,” *JHEP* **07** (2002) 012, [arXiv:hep-ph/0201195](https://arxiv.org/abs/hep-ph/0201195) [[hep-ph](#)].
- [89] Sjöstrand, Torbjorn and Mrenna, Stephen and Skands, Peter Z., “A Brief Introduction to PYTHIA 8.1,” *Comput. Phys. Commun.* **178** (2008) 852, [arXiv:0710.3820](https://arxiv.org/abs/0710.3820) [[hep-ph](#)].
- [90] P. Z. Skands, “Tuning Monte Carlo Generators: The Perugia Tunes,” *Phys. Rev.* **D82** (2010) 074018, [arXiv:1005.3457](https://arxiv.org/abs/1005.3457) [[hep-ph](#)].
- [91] J. Alwall, P. Demin, S. de Visscher, R. Frederix, M. Herquet, F. Maltoni, T. Plehn, D. L. Rainwater, and T. Stelzer, “MadGraph/MadEvent v4: The New Web Generation,” *JHEP* **09** (2007) 028, [arXiv:0706.2334](https://arxiv.org/abs/0706.2334) [[hep-ph](#)].

- [92] S. Frixione and B. R. Webber, “Matching NLO QCD computations and parton shower simulations,” *JHEP* **06** (2002) 029, [arXiv:hep-ph/0204244](#).
- [93] G. Corcella *et al.*, “HERWIG 6: An Event generator for hadron emission reactions with interfering gluons (including supersymmetric processes),” *JHEP* **01** (2001) 010, [arXiv:hep-ph/0011363](#).

Acknowledgements

At this point I want to thank everyone supporting and helping me during this thesis:

- Prof. Dr. Dorothee Schaile for welcoming me in her group and supporting me in my professional development
- Dr. Jeanette Lorentz for her supervision of this thesis, her steady push and support to further improve my work, and her reassurances in difficult situations
- Andrea Matic, for being the best possible office colleague, for always cheering me up, helping me out and taking my loads of questions
- Peter Tornambé, for being the greatest colleague, being always open for discussions and pushing our analysis forward
- Dr. Nikolai Hartmann, for helping out with scripts and advice in every situation with enormous patience
- Danijela Bogavać, for all her helpful advices, especially towards the end of this thesis
- Fabrizio Trovato, for bringing in the sense of humour into our analysis while working long hours
- The complete Schaile-group for all its willingness to take questions, all social activities and the ping-pong matches to clear up my mind
- My family, for their steady support throughout my bachelor's and master's degree. Without you it would have been much harder.

Finally, I want to thank my boyfriend, Christian Geishauser, for being the best possible companion throughout the last years, for believing in me when I didn't and making me smile after long hours.

Selbständigkeitserklärung

Hiermit erkläre ich, die vorliegende Arbeit mit dem Titel

Search for charginos and neutralinos decaying via a W and a Higgs boson into final states with two same-sign leptons with the ATLAS detector

(Suche nach Charginos und Neutralinos im Zerfall über ein W und ein Higgs Boson in Endzustände mit zwei gleich-geladenen Leptonen mit dem ATLAS Detektor)

selbstständig verfasst zu haben und keine anderen als die angegebenen Quellen und Hilfsmittel benutzt zu haben.

München, 25.04.2018, Daniela Maria Köck